2015

SPECTROSCOPIC CHARACTERIZATION OF LANTHANUM-MEDIATED HYDROCARBON ACTIVATION

Dilrukshi C. Hewage
University of Kentucky, hewagedilrukshi@gmail.com

Recommended Citation

Hewage, Dilrukshi C., "SPECTROSCOPIC CHARACTERIZATION OF LANTHANUM-MEDIATED HYDROCARBON ACTIVATION" (2015). *Theses and Dissertations--Chemistry*. 54.
https://uknowledge.uky.edu/chemistry_etds/54

STUDENT AGREEMENT:

I represent that my thesis or dissertation and abstract are my original work. Proper attribution has been given to all outside sources. I understand that I am solely responsible for obtaining any needed copyright permissions. I have obtained needed written permission statement(s) from the owner(s) of each third-party copyrighted matter to be included in my work, allowing electronic distribution (if such use is not permitted by the fair use doctrine) which will be submitted to UKnowledge as Additional File.

I hereby grant to The University of Kentucky and its agents the irrevocable, non-exclusive, and royalty-free license to archive and make accessible my work in whole or in part in all forms of media, now or hereafter known. I agree that the document mentioned above may be made available immediately for worldwide access unless an embargo applies.

I retain all other ownership rights to the copyright of my work. I also retain the right to use in future works (such as articles or books) all or part of my work. I understand that I am free to register the copyright to my work.

REVIEW, APPROVAL AND ACCEPTANCE

The document mentioned above has been reviewed and accepted by the student's advisor, on behalf of the advisory committee, and by the Director of Graduate Studies (DGS), on behalf of the program; we verify that this is the final, approved version of the student's thesis including all changes required by the advisory committee. The undersigned agree to abide by the statements above.

Dilrukshi C. Hewage, Student

Dr. Dong-Sheng Yang, Major Professor

Dr. Dong-Sheng Yang, Director of Graduate Studies

SPECTROSCOPIC CHARACTERIZATION OF LANTHANUM-MEDIATED HYDROCARBON ACTIVATION

Dissertation

A dissertation submitted in partial fulfillment of the
requirements for the degree of Doctor of Philosophy in the
College of Arts and Science
At the University of Kentucky

By

Dilrukshi C. Hewage

Director: Dr. Dong-Sheng Yang, Professor of Chemistry

Lexington, Kentucky

2015

ABSTRACT OF DISSERTATION

SPECTROSCOPIC CHARACTERIZATION OF LANTHANUM-MEDIATED HYDROCARBON ACTIVATION

Lanthanum (La)-promoted hydrocarbon activation reactions were carried out in a laser vaporization metal cluster beam source. Reaction products were identified by time-of-flight mass spectrometry, and the approximate ionization thresholds of La-hydrocarbon complexes were located with photoionization efficiency spectroscopy. The accurate ionization energies and vibrational frequencies of the La complexes were measured using mass analyzed threshold ionization (MATI) spectroscopy. Their molecular structures and electronic states were investigated by combing the MATI spectroscopic measurements with quantum chemical and Franck-Condon factor calculations.

In this dissertation, La-mediated C-H and C-C bond activation reactions were investigated for several small alkynes (acetylene, propyne) and alkenes (propene, 1,3-butadiene, 1-butene). The C-H bond activation was observed for both alkynes and alkenes and the C-C bond activation for alkenes. The metal-hydrocarbon intermediates formed by the C-H or C-C bond cleavage reacted further with one or more parent hydrocarbon molecules to produce larger species by C-C bond coupling reactions. Structural isomers of the intermediates and products were identified within an energy range of several kilocalories per mole. Reaction pathways for the intermediate and product formations were studied by theoretical calculations.

The ground electron configuration of La atom is $4d^1 6s^2$. Upon the hydrocarbon coordination, La atom is excited to a $4d^2 6s^1$ configuration to facilitate the formation of two La-C bonds. After the metal-hydrocarbon complex formation, only one electron is left in the 6s orbital of the metal center. Therefore, the most stable electronic state of the La complexes studied in this work is in a doublet spin state. Ionization of the doublet state yields a preferred singlet ion state. Although La is in the formal oxidation state of +2, the ionization energies of the metal-complexes are significantly lower than that of the free atom. This observation suggests that the concept of the formal oxidation state widely used in chemistry textbooks is not useful in predicting the change of the ionization energy of a metal atom upon ligation. Moreover, ionization has a very small effect on the geometry of the hydrocarbon fragment in each complex but significantly reduces the La-C distances as a result of an additional charge interaction.

KEYWORDS:

MATI spectroscopy, C-H and C-C Bond activation, metal-hydrocarbon complexes, quantum chemical and Franck-Condon factor calculations.

Dilrukshi C. Hewage

07/25/2015

Date

SPECTROSCOPIC CHARACTERIZATION OF LANTHANUM-MEDIATED HYDOCARBON ACTIVATION

By

Dilrukshi C. Hewage

Dr. Dong-Sheng Yang

Director of Dissertation

Dr. Dong-Sheng Yang

Director of Graduate Studies

07/25/2015

Dedicated to my mentor and family....

ACKNOWLEDGEMENTS

I would like to express the deepest appreciation to my mentor Prof. Dong-Sheng Yang, for his supervision, enormous support and patience during my PhD career. He continually conveys a spirit of adventure in regard to research and an excitement in regard to teaching. I specially admire him for giving me the freedom to make independent decisions in the research. Without his guidance and persistent help, this dissertation would not have been possible.

I must express my thanks to Prof. Dennis Clouthier for his kind support as the director of graduate admissions at the beginning of my career at the University of Kentucky. He continuously supported me as a member of my advisory committee, and his insightful comments were always invaluable in my research. I would also like to thank him for nourishing me with quantum chemistry as a wonderful teacher. I offer my sincere appreciation to Prof. John P. Selegue for sharing his enormous knowledge with me whenever necessary. His careful suggestions were priceless in the progression of my research. I would like to acknowledge Prof. Chang-Guo Zhan for providing helpful suggestions in quantum chemical calculations during advisory committee meetings..

I express my great appreciation to all my current and former coworkers for their intellectual insight and friendship. I would like to especially acknowledge Dr. Lu Wu and Dr. Ruchira Silva for offering their expertise with no hesitation during their time in the lab and even after leaving the lab. Their talents and friendship will always be remembered and valued. I offer my sincere acknowledgements to Dr. Mourad Rodajane and Dr. Sudesh Kumari for their initial work in the metal + hydrocarbon research project which I have continued during my research career. They generously shared their experience and initial findings with me which was enormously helpful in the continuation of the project. I would like to thank Dr. Jung Sup Lee for his kind guidance and understanding during my first year in the lab and Mr. Wenjin Cao, Mr. Yuchen Zhang and Mr. Tao Jin for their assistance in the experimental work. I greatly admire the former lab member, Dr. Shengang Li for writing a powerful and fast FCF simulation program to process computational data. We would be vulnerable in data analysis without his simulation program.

I cannot forget the people who provided the invaluable help to maintain instruments running in appropriate conditions. They are Mr. Art Sebesta (electronics), Mr. J. Babbitt (glassware), Mr. Jim Morris, Mr. Charles Tipton, Steven Maynard (machinery) and Mr. Edward Duhr (computer hardware). Without their assistance, my lab work would not have been as smooth as it has been.

I am indebted to the Department of Chemistry and the Graduate School for the teaching assistantship and travel awards to the annual International Symposia on Molecular Spectroscopy. I am grateful for the financial support from the National Science Foundation Division of Chemistry and additional support from the Kentucky Science and Engineering Foundation for this research project.

Last, but not least I would like to express my greatest gratitude to my family for their moral support throughout my life and career. I owe my parents, Mr. Rupasena Hewage and Mrs. Mallika Haputhantree for their unconditional love and encouragements in my life, and I always admire the joyful brotherhood of my brother, Kasun Hewage. I offer my deepest gratitude to my husband, Thilanga Liyanage for his deep love and care.

The experience in science and the life I had at the University of Kentucky would never be forgotten. This work is dedicated to my mentor and family.

TABLE OF CONTENTS

CHAPTER 1. INTRODUCTION

CHAPTER 2. METHODOLOGY

CHAPTER 3. LANTHANUM-MEDIATED CYCLO-OLIGOMERIZATION OF ACETYLENE TO BENZYNE AND NAPHTHALENE

CHAPTER 4. LANTHANUM-MEDIATED C-H BOND ACTIVATION OF PROPYNE AND IDENTIFICATION OF LaC_3H_2 ISOMERS

CHAPTER 5. C-C BOND ACTIVATION AND, COUPLING OF PROPENE INDUCED BY LANTHANUM ATOM

CHAPTER 6. C-C AND C-H BOND ACTIVATION, AND COUPLING INDUCED BY LANTHANUM ATOM

CHAPTER 7. LANTHANUM ATOM MEDIATED BOND ACTIVATION OF 1-BUTENE

LIST OF TABLES

LIST OF FIGURES

CHAPTER 1. INTRODUCTION

1.1 Bond Activation of Hydrocarbons

Carbon-carbon and carbon-hydrogen (C-C and C-H) bonds of small hydrocarbons are relatively chemically inert due to their strength, nonpolar nature, and low polarizability.[1] There have been extensive efforts to activate less reactive hydrocarbons and convert them into more valuable products, such as acids, alcohols, and ketones. The available methods for such activation are thermal activation, super acid mediated activation, photoactivation, and metal-mediated activation.[2] Photoactivation is highly selective, but less economic.[2] Thermal activation is an energy intensive and less selective method.[2,3] Super acid mediated activation provides certain selectivity, but requires harsh conditions.[2] Metal-mediated activation is selective and economic and is widely used in organic synthesis and industrial applications.[1,2,4-20] Some of these application include selective functionalization such as metathesis[21] and polymerization[22-24] of the hydrocarbons. Reactions of the transition metals with the hydrocarbons may involve both C-H and C-C bond activation. [2,5,13,25-27] Typical, the C-H bonds (418 kJ mol^{-1}) in the hydrocarbons are stronger than the C-C bonds (348 $kJmol^{-1}$). In spite of the thermodynamic stability of the C-H bonds, the C-H bond activation is more common than the C-C bond activation by transition metal centers. [5,28,29] There are few factors which govern this preference. The C-H bonds are more abundant than the C-C bonds in most hydrocarbon compounds. The metal-hydrogen bonds are usually stronger than the metal-carbon bonds, making the C-H bond activation thermodynamically more favorable. Moreover, when a metal inserts into a C-H bond, the 1s spherical orbital of H favors the formation of a multi-centered transition state, which reduces the barrier of the C-H bond activation process.[28] On the other hand, the C-C bonds are highly directional and don't favor a multicenter transition state. Thus, there is a larger energy barrier for the C-C bond activation.[6]

In the activation of C-H bonds, there is clearly an inverse relationship between the bond strength and the activation barrier.[5] The alkenes and alkynes can form strong metal-association π (120-250 kJ/mol) complexes prior to the C-H insertion, while the alkanes can only form weak σ bonds (< 8 kJ/mol) with the metal.[5] Therefore, the metal directly inserts in to the C-H bond in alkanes. This direct insertion of a metal atom into a C-H bond generates a significant repulsion between metal electrons and σ C-H bond electrons.[5] Therefore, the formation of a π association complex prior to the metal C-H bond insertion greatly reduces the energy barrier of the C-H bond activation.[5] The bonding of the π association complex is explained by the Dewar-Chatt-Duncanson model.[30] Figure 1.1 displays the molecular orbital interaction diagram of this model. According to the model, the π symmetry bonding orbital of a hydrocarbon donates its electron density to an empty metal d-orbital, and a filled metal d-orbital donates its electron back to the empty π antibonding orbital of the hydrocarbon. Both donation and back-donation increase the metal-carbon bond strength, but reduce the bond order of the C-C bond.

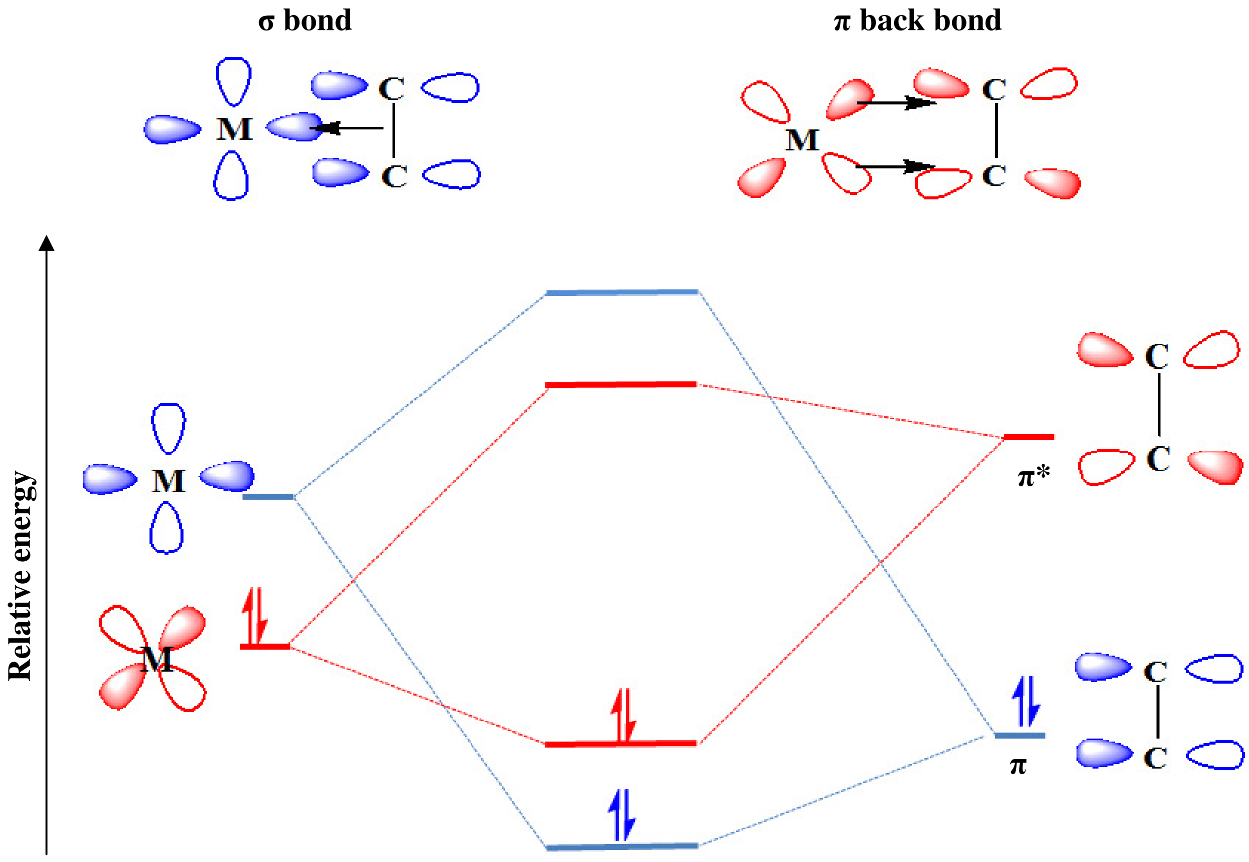

Figure 1.1 Molecular orbital interaction diagram of metal-π association complex.

1.2 Motivation

Hydrocarbons are not only the major constituents of petroleum and natural gas, but also the most abundant, low-cost stock for functionalized organic chemicals. The transformation of hydrocarbons to value-added products requires activation of thermodynamically stable C-H and C-C bonds as discussed in the introduction. Development of this area will help to discover new routes to convert hydrocarbons into more valuable products in an inexpensive way. The goal of designing selective and effective reagents for such reactions has stimulated extensive research activities on metal-medicated hydrocarbon activation in condensed[1,2,4,14,17,31,32] and gas[5,25,28,33-49] phases. Gas-phase studies provide an efficient means to investigate intrinsic reactivity patterns, reaction pathways, and structure-reactivity relationships of crucial intermediates and distinguish the intrinsic chemistry from solvation or counter ion effects. The most popular gas phase studies in the field are cross molecular beam[5,28,42,43] and fast-flow reactor methods.[25,41,44-46] The cross molecular beam method has been used to investigate the reaction channels and product branch ratios at different collision energies of the system.[5,28,42,43,50] The fast flow reactor method has been used to measure the reaction rate constants.[25,41,44-46] The data from the previous studies are essential but not sufficient for devising plausible reaction pathways. The other critical piece of information is the molecular structures and electronic states of reactants, intermediates, and products. The molecular structures and electronic states of the reactants are generally known, but few spectroscopic measurements have been reported for the intermediates and products.[11,51-53] Because of the lack of the spectroscopic measurements, the current knowledge about the structures and electronic states of the reaction intermediates and products is largely from theoretical predictions.[6,21,54-58] However, the reliable prediction of the electronic states and geometric structures is complicated by possibly many low-energy structural isomers of each complex and high-dense low-lying electronic states of each isomer. Therefore, a reliable identification of the molecular structures and electronic states generally requires the confirmation by spectroscopic measurements, especially by high resolution spectroscopic techniques. My work aims to determine the molecular structures and electronic states of the intermediates and products using the combination of the spectroscopic and computational methods. By investigating the structures and electronic states of the intermediates and products, we hope to gain new insight into the reaction mechanisms of the metal-mediated hydrocarbon activation reactions.

1.3 Scope of the Study

The scope of this dissertation is to investigate Lanthanum (La)-mediated bond activation of small hydrocarbons. The structural isomers of the intermediates and products are identified by using vibrationally resolved mass analyzed threshold ionization (MATI) spectroscopy and quantum chemical calculations. The possible reaction pathways of the product formation are proposed with the help of the theoretical calculations. La metal is considered due to the existence of a single isotope and the expected low ionization energy (IE) of the organometallic complexes. The IEs of the complexes formed are assumed to be in the energy range of 40000 to 48000 cm^{-1}, which can easily be achieved by frequency-doubled dye lasers in our research lab. Moreover La metal is much cheaper than many other popular metal catalysts in the industry.[59]

We have tried both saturated (alkane) and unsaturated hydrocarbons (alkene and alkyne) and found that the unsaturated hydrocarbons are much more reactive. Reactions between the La atom and alkanes are observed, but the amount of the products generated is not sufficient for mass analyzed threshold ionization (MATI) spectroscopic measurements. The details of the

MATI spectroscopic technique will be discussed in section 1.4. Since the MATI technique is based on the same idea as the zero electron kinetic energy (ZEKE) technique, and both are variants of photoelectron spectroscopy, I will first discuss about photoelectron spectroscopy and then the ZEKE and MATI techniques.

1.4 Photoelectron Spectroscopy

Photoelectron spectroscopy (PES) is based on Einstein's photoelectric effect.[60] The schematic of photoelectron effect is shown in Figure 1.2. A photon can remove an electron from a molecule if the photon energy is greater than the energy holding the electron in the molecule. Any photon energy in excess of the ionization energy (IE) is carried by the outgoing electrons in the form of kinetic energy.

PES is used to learn about the electronic structure of molecules (or atoms). According to Koopman's theorem, "the negative of the energy of an occupied orbital of a molecule from a theoretical calculation is equal to the vertical ionization energy of the molecule".[61] Therefore, the photoelectron technique reveals information about the occupied molecular orbitals. There are two general ways to carry out PES measurements. In the conventional PES, the molecules are irradiated with light of fixed wavelength and the kinetic energy of the emitted electrons is measured. In this method, a tunable energy source is not required, making the experimental setup relatively simple.[62] The disadvantage of this method is its limited spectral resolution arising from the technique difficulty of distinguishing the electrons with small kinetic energy differences. The first PES measurement using this method was performed by Turner *et al*. in the 1960s.[63] This method has rarely resolved the vibrational bands of polyatomic molecules since the resolution is around 10 meV at best. To improve the PES

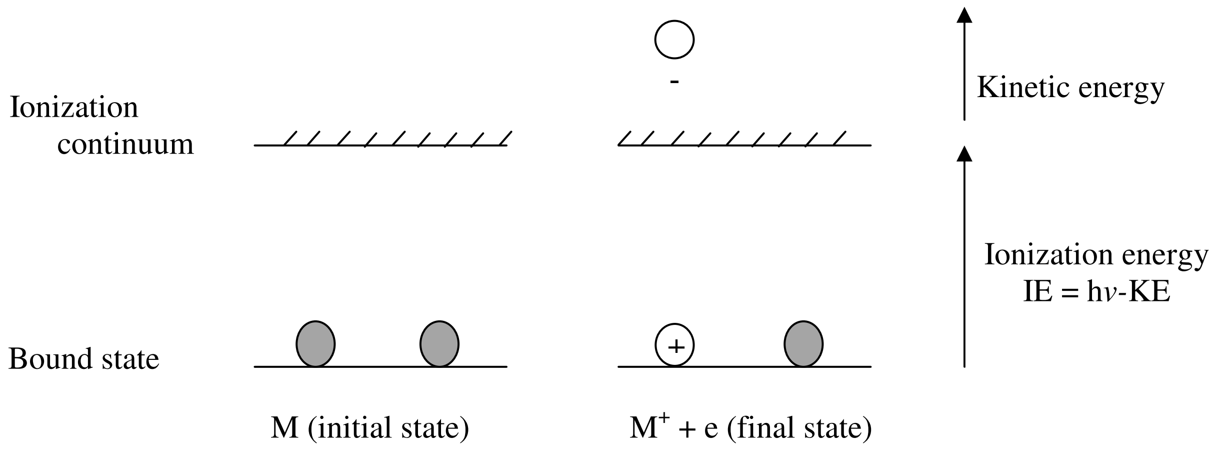

Figure 1.2 Schematic of photoelectric effect.

spectral resolution, the wavelength is scanned through ionization thresholds and the electrons with a given kinetic energy are detected. If the photon energy is equal to the ionization energy, electrons with zero kinetic energy are emitted. If these zero kinetic energy electrons are detected, the technique is known as ZEKE PES.[62] Details of ZEKE PES are described below.

1.4.1 ZEKE Spectroscopy

ZEKE spectroscopy stands for Zero Electron Kinetic Energy spectroscopy and was developed by Muller-Dethlefs and coworkers in 1984.[64] Much higher spectral resolution of ZEKE spectroscopy (~ 0.1 meV) than that of conventional PES has led to many exciting applications in chemical physics and chemistry in the last three decades. [65-67] There are two ways to generate ZEKE electrons. One is through direct photoionization. In this method, a tunable light source is scanned over the ionization thresholds under a field free condition.[68] ZEKE electrons are formed if hν = IE and kinetic electrons are produced if hν > IE. Kinetic electrons fly out of the ionization region after a certain time, whereas the ZEKE electrons remain at the point where they are produced. Once an electric field is applied to accelerate electrons towards the detector, the kinetic and ZEKE electrons arrive at the detector at different times. Beside the direct photoionization, ZEKE electrons can also be produced by delayed pulse-field-ionization (PFI) of long-lived (up to tens of μs), high-lying (principal quantum number > 150) Rydberg states[69] as shown in Figure 1.3. In this way, electrons are first photoexcited to the high-lying Rydberg states, which are just few cm^{-1} below the ionization threshold, followed by the field ionization. [62,69-71] In both approaches, kinetic electrons may also be produced if the photon energy is greater than the energy difference between the final and initial states. To remove these kinetic electrons, a small DC field (0.06 V.cm^{-1}) is applied. This small field sufficiently removes the kinetic electrons within a few micro seconds (1-5 μs) after firing the photoexcitation laser.

After this short time period, the long-lived, high-lying Rydberg states are still survived. In these Rydberg states, the electron is considered to orbit around the ionic core that closely resembles the ionized molecule. Due to the high principal and angular momentum quantum numbers (n and l), the electron has a spherically shaped orbit in these states, and the electron-core interaction can essentially be described by a simple Coulomb force. In other words, the electron-core distance is so large that the ionic core resembles a point charge with respect to the orbiting electron. The strong l- and m_l-mixing (m_l = the magnetic component of l) resulting from the presence of the stray fields and nearby ions is known to increase the life time of these Rydberg state to the microsecond scale. These long-lived, high-lying Rydberg states can then be ionized by a small, delayed pulsed electric field (1.2 V.cm^{-1}) . Because of the involvement of the pulsed field ionization, this technique is commonly known as PFI-ZEKE and the schematic of the technique is shown in Figure 1.3. The spectral resolution of the technique depends on the linewidth of the excitation laser and the strength of the field used for ionization.[62] The field-induced IE shift (δ) can be determined by recording the ZEKE spectra as a function of the field strength (E_P) and calculated by the following empirical formula:

$$\delta = c.\sqrt{E_p} \qquad (1.1)$$

where c is a constant.

However, the measured field-induced shift is smaller than the linewidth of the ZEKE spectra of the metal complexes.[72] As a result, this field-induced measurement is not carried out for every molecular systems, but the estimated small shift from Equation (1.1) is included in our measurement uncertainty. Since the ionization cross-sections are continuous through the ionization threshold, ZEKE spectra provide the same information as the

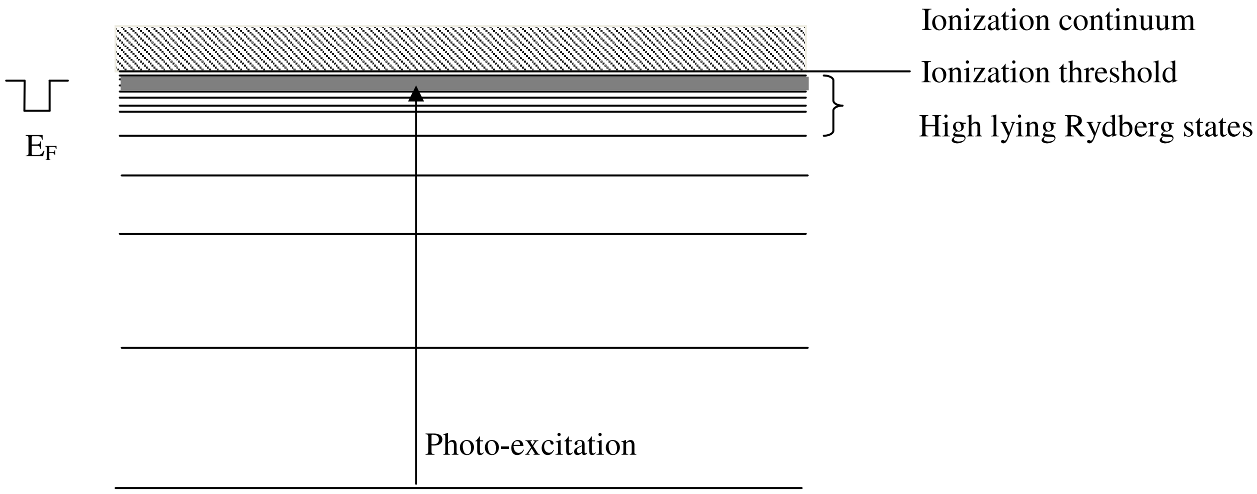

Figure 1.3 Schematic of PFI-ZEKE experiment.

conventional PES obtained by direct photoionization, but with a much higher resolution. The experimental setup of the ZEKE experiment will be discussed in Chapter 2.

The precise IE measured from the ZEKE spectrum can be used in a thermodynamic cycle to derive the bond dissociation energy of the neutral complex. Figure 1.4 illustrates the relationship between ionization energies of the metal atom and complex and bond dissociation energies of the neutral and ionized complexes. The potential energy curves of the neutral and ionic complexes in Figure 1.4 are assumed to be the function of the metal-ligand distances and displayed by the red and blue curved lines, respectively. The nuclear coordinate at the lowest energy of each curve corresponds to the equilibrium metal-ligand distance of the complex. The metal-hydrocarbon bond strength of the cation complex is usually stronger than that of the corresponding neutral complex because of the additional ion-multipole interactions in the cation. Therefore the shape of the potential energy curves of the neutral and cation complexes are often different. In addition, the potential energy wells of the neutral and cation complexes may have different zero point energies, as indicated by the black horizontal line at the near bottom of each well. The zero point energies are the vibrational energies of the molecules at the zero vibrational quantum number (v). The quantum mechanic harmonic oscillator energy levels (E_v) are related to the vibrational quantum number by

$$E_\mathrm{v} = \hbar \nu_i(\mathrm{v} + ½) \qquad \mathrm{v} = 0, 1, 2, ... \tag{1.2}$$

where $\hbar = h/2\pi$ and ν_i is the vibrational frequency of mode *i*. Thus, even at v = 0, the vibrational energy is a nonzero positive value ($½\hbar\ \nu_i$). The total zero point energy is the sum of the $E_{\mathrm{v}\,=\,0}$ terms over all 3N-6 (nonlinear molecules) or 3N-5 (linear molecules) vibrational modes of the

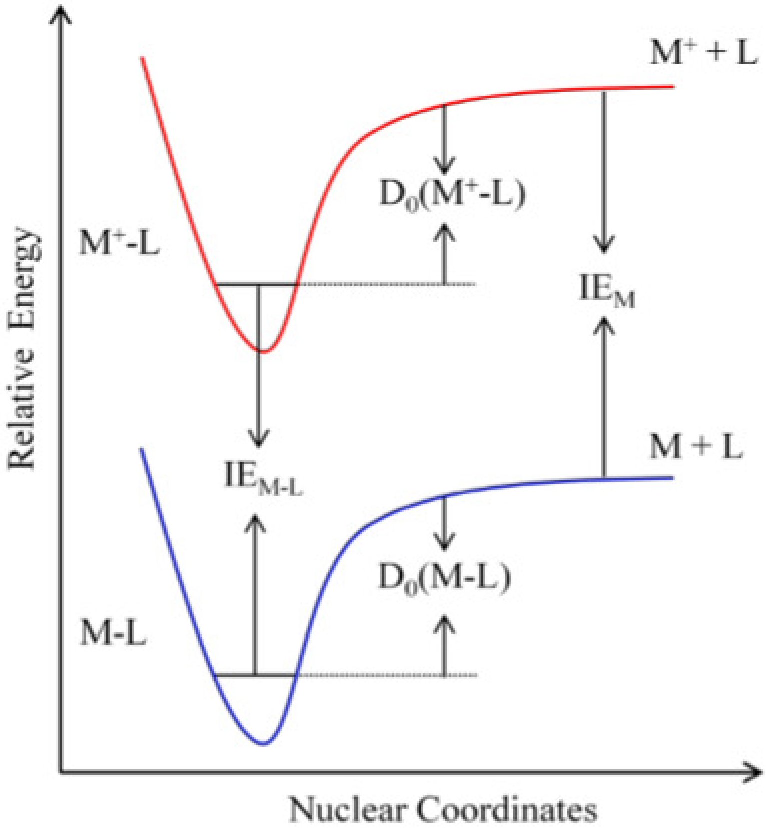

Figure 1.4 Thermodynamic relationship between bond dissociation energies (D_o/D_0^+) and ionization energies (IEs) of metal complexes as a function of the potential energy surfaces. IE_{M-L} = IE of the ML complex; IE_M = IE of the M atom; D_o(M-L) = D_0 of the neutral ML complex; $D_o(M^+$-L) = D_0 of ionic $(ML)^+$ complex.

complex. Because the stronger metal-ligand bonding in the cation complex, the metal-ligand vibrational frequencies and thus the zero point energy in the cation complex are often larger than those in the neutral complex. This zero point energy comes from the Heisenberg uncertainty principle: certain pairs of complementary physical properties of a particle (properties such as position *x* and momentum *p*) cannot be measured simultaneously to an infinite precision. In 1927, Werner Heisenberg stated that the more precisely *x* of a particle is determined, the less precisely its *p* can be known, and vice versa. Mathematically, the Heisenberg uncertainty principle is expressed as

$$\Delta x \Delta p_x > \hbar \qquad (1.3)$$

where Δx is the uncertainty in position, Δp_x is the uncertainty in momentum, and h is the Planck constant $(\hbar = \boldsymbol{h/2\pi})$**.** According to the uncertainty principal, all particles should have nonzero momenta; otherwise, the uncertainty in momentum would be zero (infinite precision), and the position of such a stationary particle would be precisely known (because the particle is not moving). Therefore, all atoms in a molecule must have non zero momenta and thus kinetic energies. However, chemical bonds within a molecule prevent the atoms from drifting far away from one another. As a result, the molecule vibrates even at v = 0. This means that molecules are constantly vibrating, and the molecular structure at one point in time may vary slightly from the molecular structure at a different point in time. However, the uncertainty principle only has a practical impact at the molecular scale due to the magnitude of $\hbar$. Because of the uncertainty principle, experimental measurements of molecules will always include the vibrational zero point energies. On the other hand, the IE of a bare metal atom does not include a vibrational zero point energy correction because free atoms cannot vibrate.

The relationship between dissociation and ionization energies is expressed as

$D_o(M\text{-}L) + IE_{M\text{-}L} = IE_M + D_o(M^+\text{-}L)$ (1.4)

Where, **$D_o(M^+\text{-}L)$:** dissociation energy of the cation complex

$D_o(M\text{-}L)$: dissociation energy of the neutral complex

$IE_{M\text{-}L}$: ionization energy of the neutral complex

IE_M: ionization energy of the metal atom

The ionization energies of the metal atoms have already been determined very accurately by various experimental methods,[52] and the dissociation energies of many metal ion complexes have been determined by collision induced dissociation or photodissociation.[48,73] Therefore, the dissociation energy of the neutral complex can be derived by measuring the ionization energy of the metal complex from the ZEKE spectra. In addition to the ionization energies, the metal-ligand and other vibrational frequencies from the ZEKE measurements are valuable in determining the structures of the metal complexes. The vibrational frequencies of the metal-ligand modes are typically in the range of 300-600 cm^{-1}. Although IR spectroscopy is often used to measure the vibrational frequencies of molecules, it is difficult for the metal-ligand vibarational modes of the metal complexes in the gas phase. This is because the vibrational transitions are generally weaker than the electronic transitions and the generation of a tunable laser with wavenumber < 400 cm^{-1} is difficult in the laboratory (though this is not an issue for expensive free electron lasers).

Since the ZEKE technique detects electrons, it is sometime difficult to identify the carrier of the electrons once the molecular beam contains multiple complexes with similar ionization energies. This drawback is overcome by mass-analyzed threshold ionization spectroscopy (MATI), a sister technique of PFI-ZEKE. The details of the MATI technique is discussed in the following section.

1.4.2 MATI Spectroscopy

The MATI technique was developed in 1991 by Zhu and Johnson.[74] In this technique, cations are detected instead of electrons. Because ions are much heavier than electrons, a longer delay time is required to separate the Rydberg molecules from prompt ions generated by laser ionization. Moreover, a much stronger electric field (320 V.cm^{-1}) is required to accelerate ions towards the detector. Because of the requirement of the strong electric field, the resolution of MATI is somewhat reduced compared to that of ZEKE. However, MATI is a powerful technique because of its ability of mass selection.[74-78] The experimental setup of the MATI experiment will be discussed in Chapter 2. In order to better analyze the ZEKE or MATI spectra, theoretical calculations are carried out, which are discussed below.

1.5 Theoretical Calculations

Computational chemistry includes the molecular mechanics and electronic structure theory. The molecular mechanic calculations are based on the laws of the classical physics, whereas the electronic structure methods are based on the laws of the quantum mechanics. In the present study, we have performed quantum chemical calculations. In the quantum mechanics, the energy and other properties of a molecule can be obtained by solving the time-independent Schrodinger equation:

$$\hat{H}\psi = E\psi \tag{1.5}$$

where $\hat{H}$ is a mathematical operator called Hamiltonian, E is the eigenvalue of the state, and ψ is the wave function. The wave function describes the quantum states of the system and contains all the information about the system. If the accurate wave function is known, the corresponding energy levels can be obtained by solving the time-independent Schrodinger equation as described in equation (1.5). Even though the wave function of a system is time dependent, the probability density of a molecule in a given eigenstate is time-independent. [79] However, obtaining the exact solution to the Schrodinger equation is practically impossible for many electron systems other than for the simplest systems. Therefore, the electronic structure methods use various approximations to obtain approximate solutions to the Schrodinger equation.

1.5.1 Ab Initio Calculations

Ab initio means "from the beginning" in Latin. The task of the ab initio calculations is to solve the electronic Schrodinger equation to obtain the electronic wave function and electronic energy. Ab initio calculations are from first principles of quantum mechanics. They uses the values of a small number of physical constants (speed of light, Planck's constant, and the masses and charges of electrons and nuclei) and include no other experimental data. In the classical physics, the total energy of a system is the summation of the kinetic energy and potential energy. The kinetic energy of a particle, *KE* is given by

$$KE = \frac{p^2}{2m} \tag{1.6}$$

where , p is the momentum and m is the mass. The corresponding quantum chemical operator for the kinetic energy, $\hat{KE}$, is

$$\hat{KE} = -\frac{\hbar^2}{2m}\nabla^2 \tag{1.7}$$

where,

$$\nabla^2 = \left(\frac{\partial^2}{\partial x^2} + \frac{\partial^2}{\partial y^2} + \frac{\partial^2}{\partial z^2}\right) \tag{1.8}$$

These partial derivatives are taken over all space of x, y, and z coordinates. Since the molecules are composed of charged particles, protons and electrons, the potential energy term of the

Hamiltonian consists of the Coulomb interactions among these charged particles. For example, the Hamiltonian of a helium atom with the fixed nucleus is

$$\hat{H}_{He} = -\frac{\hbar^2}{2m}\nabla_1^2 - \frac{\hbar^2}{2m}\nabla_2^2 - \frac{Ze^2}{4\pi\varepsilon_0 r_1} - \frac{Ze^2}{4\pi\varepsilon_0 r_2} + \frac{e^2}{4\pi\varepsilon_0 r_{12}} \tag{1.9}$$

where the subscripts 1 and 2 are electron labels, m is the mass of the electron, Z is the atomic number, e is the charge of an electron, r_1 and r_2 are the respective electron-nucleus distances for electron 1 and 2, r_{12} is the electron-electron distance, and ε_0 is the permittivity of free space. Hamiltonian simplifications are often made using atomic units, where all physical constants are set to unity. Thus, the electronic Hamiltonian operator for a helium atom in atomic units reduces to

$$\hat{H}_{He} = -\frac{1}{2}\nabla_1^2 - \frac{1}{2}\nabla_2^2 - \frac{Z}{r_1} - \frac{Z}{r_2} + \frac{1}{r_{12}} \tag{1.10}$$

and the units are called hartrees, or atomic units (a.u.). However, the nuclear kinetic energy term is often removed from the Hamiltonian since electrons generally move at a much higher speed than the nuclei. This reasonable approximation, proposed by Born and Oppenheimer in 1927, greatly simplifies the quantum mechanical calculations.[80] Because of the electron-electron repulsion term, the Hamiltonian couldn't be solved exactly. In a molecule or atom, the orbital paths of electrons are correlated to one another due to the repulsion between the electrons. Therefore this potential energy term of the Hamiltonian is called the electron correlation energy. Since this equation cannot be solved exactly, a variety of methods has been developed to approximate solutions to the Schrödinger equation for non-hydrogen-like systems (i.e. multielectron systems). Two common ab initio methods, Hartree-Fock and Møller-Plesset perturbation, are described in Sections 1.5.1.1 and 1.5.1.2.

1.5.1.1 Hartree-Fock Method

The Hartree-Fock (HF) method is the most basic, quickest, and cheapest type of the ab initio calculations. To account for the electron-electron repulsion, this method assumes that each electron moves in a smeared-out average electro static field of all other electrons . However, this approximation overestimates the electron repulsion energies. Because it requires the final field as computed from the charge distribution to be "self-consistent" with the assumed initial field, the Hartree–Fock method is often called the self-consistent field method (SCF) in literature. Thus, self-consistency is a requirement of the solution. Figure 5 displays the full HF procedure schematically by a flow chart.

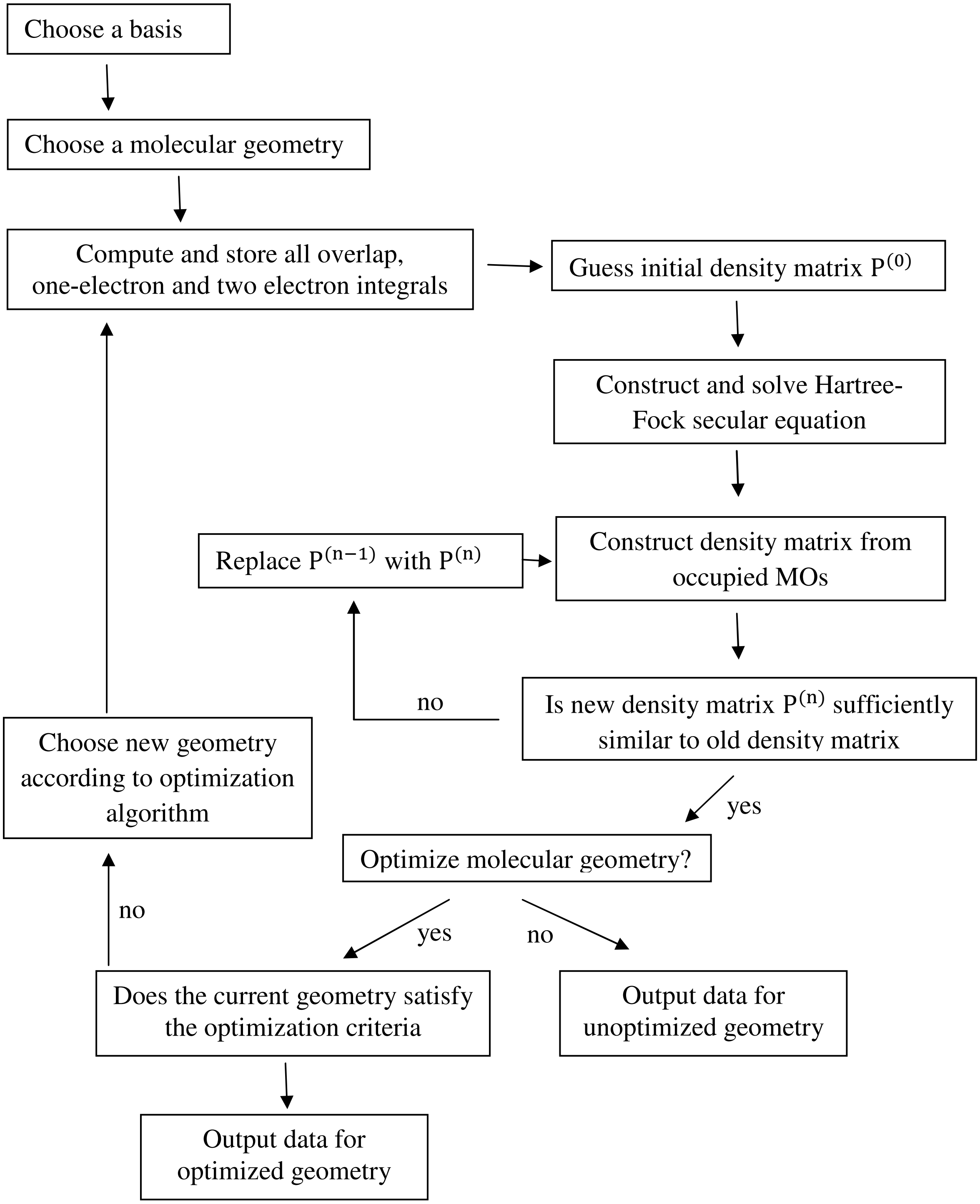

Figure 1.5 Flow chart of the HF procedure.[81]

Even with an infinite basis set, the HF method is unable to calculate the exact energy (E) of a system. The best possible solution obtained by HF method is known as the HF limit (E_{HF}). Once the E_{HF} is achieved, the error associated with the HF approximation is known as the correlation energy (E_{corr}).

$$E_{corr} = E - E_{HF} \tag{1.11}$$

In spite of the correlation energy errors, the HF energy is chemically useful for comparing two or more systems for which the errors could be made to cancel out. However, neglecting the electron correlation can have significant chemical consequences where accurate wave functions and properties are required. Nevertheless, HF provides a well-defined stepping stone on the way to more sophisticated theories of more accurate solutions to the Schrodinger equation.

1.5.1.2 Moller-Plesset Perturbation Theory

The Moller-Plesset perturbation theory is one of the post HF methods. The term of the post HF is used for the methods with electron correlation treatments. In the SCF calculations, it is assumed that the energy eigenfunctions are the product of one-electron wave functions and the effects of electron correlation, beyond that of exchange energy resulting from the anti-symmetrization of the wave function, are completely neglected. Perturbation theories introduce the electron correlation to the electronic HF Hamiltonian as a small perturbation to address instantaneous electron-electron interactions. In other words, these methods use the molecular orbitals and energies from the HF calculations as the unperturbed term and treat the perturbed term successively to higher orders. The total Hamiltonian operator, $\hat{H}$, is expressed as

$$\hat{H} = \hat{H}_0 + \lambda \hat{H}_1 \tag{1.12}$$

where $\hat{H}_0$ is the HF Hamiltonian operator, $\hat{H}_1$ is the difference between the exact electronic Hamiltonian and HF Hamiltonian operator, and λ is the perturbation parameter. The wave function and energy of a system are expressed as a power series as shown below.

$$\psi = \psi_0 + \lambda_1\psi_1 + \lambda_2\psi_2 + \ldots. \qquad (1.13)$$

$$E = E_0 + \lambda_1 E_1 + \lambda_2 E_2 + \ldots. \qquad (1.14)$$

where ψ_n and E_n are the *n*th order corrections to the HF wave function and energy, respectively. The Moller-Plesset perturbation calculations that include the *n*th order corrections to the energy and wave function are denoted as MP*n*. Among the various MPn methods, MP2 is the most widely used method and typically accounts for 80- 90% of the electron correlation energy. MP3 and MP4 methods provide 90 - 95% and 95 - 98% correlation energies, respectively. However, the MPn ($n > 2$) calculations are much more expensive and difficult to converge than MP2 and may not improve the energy with increasing order. This energy divergence arises from the fact that the MP*n* methods are nonvariational.

1.5.2 Density Functional Theory

The density functional theory (DFT) approach is based upon a strategy of modeling electron correlation via a general functional of the electron density. Instead of optimizing a wave function, an electron density is optimized in DFT. The total energy of a molecular system is expressed as:

$$E = E^T + E^V + E^J + E^{XC} \qquad (1.12)$$

Where, E^T **:** kinetic energy term (arising from the motion of the electron)

E^V**:** potential energies of the nuclear-electron attraction and nuclear-nuclear repulsion

E^J**:** electron-electron repulsion term

E^{XC}: exchange-correlation term

All terms, except for the nuclear-nuclear repulsion, are functions of the electron density. In the Kohn-Sham approach to DFT, most of the electron kinetic energy is calculated, and the remaining unknown components are approximated.[81] These unknown components of the electron energy are combined into a single term called the exchange-correlation energy. The DFT methods require the knowledge about the dependence of the molecular properties on the electron density, while the traditional wave-functional-based ab initio methods require a correct quantum chemical operator to derive the molecular properties.

There are advantages and disadvantages of the DFT methods compared to the wave-function-based ab initio methods. A DFT calculation requires about the same amount of computer resources as HF, but provides better results because of the inclusion of the electron correlation effect. The DFT accuracy is between those of HF and MP2, with the advantage of a lower cost. DFT is the most cost effective method to achieve a given level of accuracy. The wave function of a n-electron molecule requires 4n variables (3 spatial and 1 spin) for each electron, whereas the electron density function requires only three position variables ρ(x, y, z) to define the system. However, the functional cannot be systematically improved as the exact mathematical form of the functional is unknown. On the other hand, wave functions can be improved systematically by including bigger basis sets and higher level correlation models to reach the exact solution of Schrödinger equation.

The DFT methods used in this dissertation are based on generalized gradient approximation.[81] The gradient-corrected correlation functionals are derived by Lee, Yang, and Parr (LYP) and Perdew.[82,83] The exchange functional is the Becke's three parameter hybrid functional (B3), which includes a balanced contribution of the exact exchange functional and the gradient-corrected exchange functional.[84]

In addition to the quantum chemical calculations, spectral simulations are carried out using a home-made software called "FCF program" developed by Shenggang Li.[85] Using this program, we calculate multi-dimensional Franck-Condon (FC) factors and molecular Boltzmann populations.

1.6 The Franck-Condon Principle

For an allowed vibronic transition, the band intensities are governed by the Franck-Condon principle.[86-88] The band intensities are proportional to the transition moment integral, M_{ev}

$$M_{ev} = \int \psi^{*}_{e'v'} \hat{\mu} \psi_{e''v''} d\tau \tag{1.13}$$

where $\psi^{*}_{e'v'}$ and $\psi_{e''v''}$ are vibronic wave functions of the final and initial states, respectively, and $\hat{\mu}$ is the dipole moment operator. The dipole moment operator can be expressed as a linear combination of the electronic $\hat{\mu}_e$ and nuclear $\hat{\mu}_N$ dipole operators

$$\hat{\mu} = \hat{\mu}_e + \hat{\mu}_N \tag{1.14}$$

According to the Born-Oppenheimer approximation,[80] the nuclei are considered to be frozen during a vibronic transition as the electrons move much faster than the nuclei. Therefore, the electronic and nuclear components of the wave function and dipole operator can be separated, and the transition moment integral becomes

$$M_{ev} = \left(\int \psi^{*}_{e'} \hat{\mu}_e \psi_{e''} d\tau_e\right)\left(\int \psi^{*}_{v'} \psi_{v''} d\tau_N\right) \tag{1.15}$$

where the first integral is the electronic transition moment integral and the second integral is the vibrational overlap integral, called the FC overlap integral. For an allowed electronic transition, where the electronic transition moment integral is nonzero, the intensities of vibronic bands are proportional to the Franck-Condon Factor (FCF), which is the square of the FC overlap integral,

$$I_{e'v' \leftarrow e''v''} \propto \left|\int \psi^{*}_{v'} \psi_{v''} d\tau_N\right|^2 \tag{1.16}$$

The largest overlap of the wave functions is achieved if there is a minimal change in the nuclear coordinates. Therefore, the relative intensities of the vibronic transitions can be used as a guide to determine the structural difference between the two electronic states (i.e., the initial neutral state and the final cationic state). For example, if the spectrum contains a strong 0-0 transition and a short vibrational progression, the structural change between the neutral and cationic states is small. Conversely, if the spectrum displays a long vibrational progression with a weak 0-0 band, the structural change upon ionization is large. The structures of the complexes can be identified by comparing the experimental and simulated spectra.

The FCF is nonzero if the direct product of each wave function gives the totally symmetric representation. In our experiments, most neutral molecules are at the ground vibrational level, and as a result, the totally symmetric modes of the cation complex are often observed. However, the frequencies of asymmetric modes can also be measured through overtone transitions (e.g. $v' = 2 \leftarrow v'' = 0$) because the direct product of any two identical representations contains the totally symmetric representation (e.g. $b_1 \otimes b_1 = a_1$ in C_{2v}). Similarly, combination transitions involving asymmetric vibrational modes may also be observed if their direct product contains the totally symmetric representation.

1.6.1 Multidimensional Franck-Condon Factors

The FCF simulation program uses the theoretical equilibrium geometries, harmonic vibrational frequencies, and normal coordinates of the neutral complex and cation as input parameters. Upon ioninzation, the normal coordinates of a molecule may be displaced and rotated, and this is known as the Duschinsky effect.[29] A linear and orthogonal transformation between the normal coordinates of the neutral and cationic states are assumed in the Duschinsky transformation, and this transformation is typically non-linear and non-orthogonal according to the axis-switching effect.[30-32] The FCF program treats the axis-switching effect by applying a zeroth order Eckart matrix, where off-diagonal elements are diminished with each rotation. More mathematical and computational details can be found in Shenggang Li's Ph.D. dissertation and elsewhere.[85,89]

1.7 FCF Simulation Program

The version 4.6 of the FCF program is used in the present study. This program calculates multidimensional FCFs using the recursion relations formulated by Doktorov et al.[90] Because the intensities of the vibronic transitions are proportional to the square of the FCFs, spectral simulations are generated as a function of the energy, E, by

$$I(E) \propto \sum_{v} \sum_{v'} \left(\langle v|v'\rangle^2\right)\left(e^{\frac{-Ev}{kT}}\right)\left\{\frac{\gamma}{2\pi}\left[(E_o + E_{v'} - E_v - E)^2 + \left(\frac{\gamma}{2}\right)^2\right]^{-1}\right\} \tag{1.17}$$

where $I(E)$ is the relative intensity at an energy E, the first, second, and third terms in the product of the summations are the FCFs, the Boltzmann factor, and the line shape function, respectively. E_v and $E_{v'}$ are the vibrational energies of the initial and final states, respectively; E_0 is the adiabatic ionization energy. This summation runs over all initial and final vibrational states, v and v', respectively. The Lorentzian line shape is adjusted according to the experimental linewidth that is measured as the full width at half maximum (FHWM), γ.

CHAPTER 2. METHODOLOGY

2. 1 Experimental Setup

The schematic of the experimental set up is shown in Figure 2.1. The first part of the experiment is the synthesis of metal complexes in the gas phase. This process is carried out in the reaction chamber, which is evacuated by a 2200 $L.s^{-1}$ oil diffusion pump (Edwards Diffstak 250/2000M) backed by a two-stage rotary pump (Edwards E2M40) to a base pressure of about 10^{-7} Torr. The working pressure of the source chamber is in the range of 10^{-4} - 10^{-5} Torr and varies depending on the state of the reactant hydrocarbon and the method of hydrocarbon introduction. The pressure in the reaction chamber is measured by an active inverted magnetron gauge (Edwards, AIM-S-NW25). The backing pressure of the foreline is in the range of 10^{-2} - 10^{-3} Torr and is measured by a linear active Pirani gauge (Edwards, APG-L0NW16). The reaction chamber houses a piezoelectric valve, a faceplate, a micro motor, a cluster tube, a skimmer, and two deflection plates as shown in Figure 2.2. Details of the individual components are shown in Figure 2.3. The metal atoms or clusters are generated by laser vaporization. A desired metal rod is translated and rotated with the help of a micro-motor (Micro Motor Electronics, 1516E012S) so that each laser pulse hits on a fresh surface. The rotation and translation of the rod greatly helps to improve the stability of the cation or electron signals. A frequency-doubled Nd:YAG laser (Lumonics YM-800, 532 nm) is focused to a ~ 0.5 mm diameter spot on the surface of the metal rod by a focal lens (f = 30 mm) to generate the metal vapor. The metal vapor reacts with a hydrocarbon compound to produce metal-hydrocarbon complexes. The method of hydrocarbon introduction is varied according to its state. If the hydrocarbon is a gas, it is seeded in a carrier gas (He, Ar or He/Ar mixture) in a stainless steel mixing cylinder and introduced in to the reaction region via the piezoelectric pulsed valve from the back of the reaction chamber. The optimal concentration of the hydrocarbon compound in the carrier is about 10^{-5}. To change the hydrocarbon concentration, a new carrier/hydrocarbon gas mixture is required. If the hydrocarbon is a liquid, its vapor is continuously introduced at or downstream of the laser ablating point, and perpendicularly to the carrier gas beam. The flow of the vapor is controlled by a SS Integral Bonnet Angle-Pattern Needle Valve (SS-1RS4-A) and a SS Low-Flow Metering Valve (SS-SS4-VH). By adjusting the valves, the hydrocarbon concentration can be gradually changed and optimized, but the accurate concentration of the hydrocarbon is unknown in this method as we don't have a flow meter installed in the line. Depending on the vapor pressure at a given temperature, the hydrocarbon is heated up or cooled down by immersing its container in a hot or cool water bath. If the hydrocarbon is a solid, it is placed in a copper oven inside the reaction chamber. The oven is heated to an appropriate temperature using a heating cartridge and the temperature is controlled by a thermo-controller (Omega CN2110).

The resultant metal complexes are supersonically expanded into the source chamber via a cluster tube (2 mm inner diameter, 1.5 cm length). Multiple collisions occur between the complexes and carrier gas inside the cluster tube before exiting from the tube. These collisions tend to remove vibrational and rotational energies from the complexes and transform these internal energies into the translational energies so that complexes are vibrationaly and rotationaly cooled down. By changing the carrier gas and its pressure, the cooling efficiency can be altered. The heavier carrier gases have larger collision cross sections compared to the lighter ones. Therefore, the heavier carrier gases are more efficient in the cooling process. Once the carrier gas pressure is increased, more collisions will occur and the complexes would be more efficiently cooled down. The collisions with a large velocity component alone the axis of cluster tube will drive the molecules out of the cluster tube and into the vacuum. These collisions monochomatize the velocities, instead of having molecules with a large distribution of velocities in all directions. Therefore, we obtain a molecular beam with the most molecules traveling in the same direction and with about the same velocity (i.e., a molecular beam with a narrow velocity distribution of molecules). According to the Boltzmann distribution theory, narrower the velocity distribution is the lower temperature of the molecules. Therefore, the translational temperature would be significantly decreased in the supersonic expansion. This supersonically cooled molecular beam is collimated by a skimmer (2 mm diameter). A pair of deflection plates is installed right after the skimmer and the electric field of nearly 100 V.cm^{-1} is applied across the plates to remove the residual ionic species in the molecular beam. After passing through the deflection plates, the neutral molecular beam enters into the spectroscopy chamber. The reaction and spectroscopy chambers are separated by an electropneumatic gate valve (MDC GV- 2000V-P), which requires both electricity and pressurized gas (nitrogen) to operate. The gate value provides an protection to the MCP detector in the spectroscopic chamber as the valve closes automatically once the pressure of the reaction chamber exceeds a certain point.

In the spectroscopy chamber, TOF-MS spectrometry and MATI or ZEKE spectroscopy are carried out. This chamber is evacuated to a standby pressure of ~10^{-9} Torr and a working pressure of 10^{-7}-10^{-8} Torr by two 450 L.s^{-1} turbo-molecular pumps (Seiko Seiki STP451). Each Turbo-molecular pump is backed by a two stage rotary pump (Edwards RV12). To protect the turbo pumps from possible pressure failures, another electropneumatic gate valve (Edwards, GVI 060P) is used to separate the spectroscopy chamber from the turbo pumps. The pressure inside the spectroscopy chamber is measured by an active ion gauge (AIGX-S) and the backing pressure of the foreline is measured by a linear active Pirani gauge (Edwards, APG-

L0NW16). The backing pressure of the foreline is on the order of 10^{-3} Torr. The spectroscopy chamber houses a two field, space focused, Wiley-McLaren time-of-flight (TOF) mass spectrometer.[91] The TOF tube is a 13" long and 1.5" diameter cylinder and is magnetically shielded by a double-layer of µ-metal, with a two-stage extraction assembly at the bottom and a dual micro-channel plate detector (MCP) at the top. The µ-metal consists of 77% nickel, 16% iron, and 5% copper doped by about 2% chromium or molybdenum. Due to its high permeability, µ-metal is useful for shielding against static or low-frequency magnetic fields such as the earth magnetic field. The extraction assembly contains two extraction cans, named outer and inner extraction cans in Figure 2.4 (a). There are four holes (1" diameter) perpendicular to each other on the outer extraction can. Two holes are on the axis of the molecular beam, and the other two are perpendicular to the molecular beam axis. These holes allow the laser and molecular beams to enter the spectroscopy chamber. To generate a homogenous electric field between the two cans, the aperture at the bottom of the inner can is covered with a gold mesh of 95% transmittance. The surfaces of the cans are coated with a layer of graphite (Sprayon, Dry graphite lube, S00204) to remove the residual charges more efficiently. The MCP detector consists of arrays of micro channels as indicated by its name, and these micro channels are slightly tilted from the normal of the surface. Two MCPs are aligned in a chevron or V-like shape to achieve a signal amplification of 10^{6}-10^{7}. Using an external voltage divider, different voltages are applied on the two MCP plates.

The pictures of the TOF tube and MCP detector are shown in Figure 2.4. To photo-excite the complexes, a tunable laser in the UV energy region is shined onto the molecular beam. A frequency-doubled dye laser (Lumonics HD-500) pumped by a frequency-doubled or tripled Nd:YAG laser (Continuum Surelite II) is used to produce the tunable UV laser. The frequency doubling unit of the dye laser utilizes a BBO (beta-Ba2B2O4) crystal. The angle of the crystal is optimized by a motor driven system (Lumonics HyperTRAK-1000) with respect to the wavelength of the laser. The UV laser excites the neutral molecules to high lying Rydberg states, which are then ionized by a delayed electric pulsed field to generate MATI ions or ZEKE electrons. While the UV laser excitation produces the high-lying Rydberg molecules, it may also generate cations if the laser energy is higher than the ionization threshold of a particular state. The cations or electrons are extracted towards the MCP detector by the same pulsed field. The analog signal detected by the MCP is amplified by a preamplifier (Stanford Research Systems SR 445), averaged by a boxcar (Stanford Research Systems SR 250), converted to the digital signal by an analog-to-digital convertor. The signal is also monitored using an oscilloscope (Tektronix, TDS 3012).

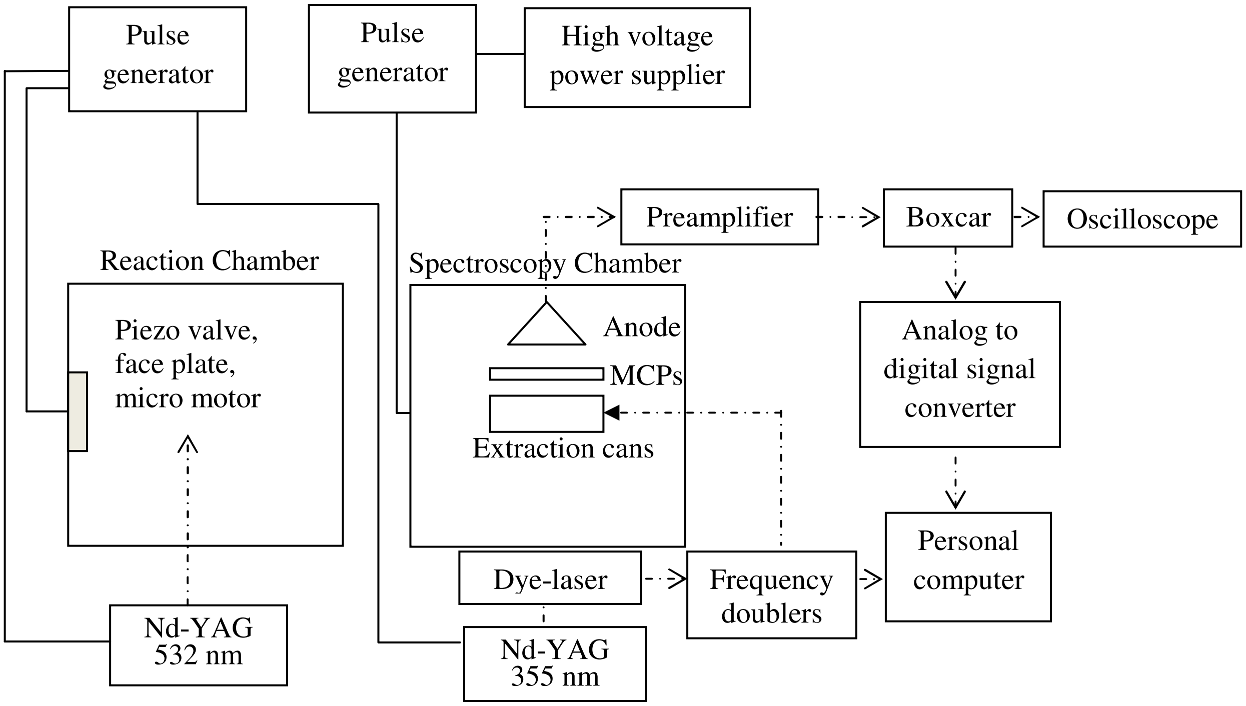

Figure 2.1 Schematic of the experimental setup.

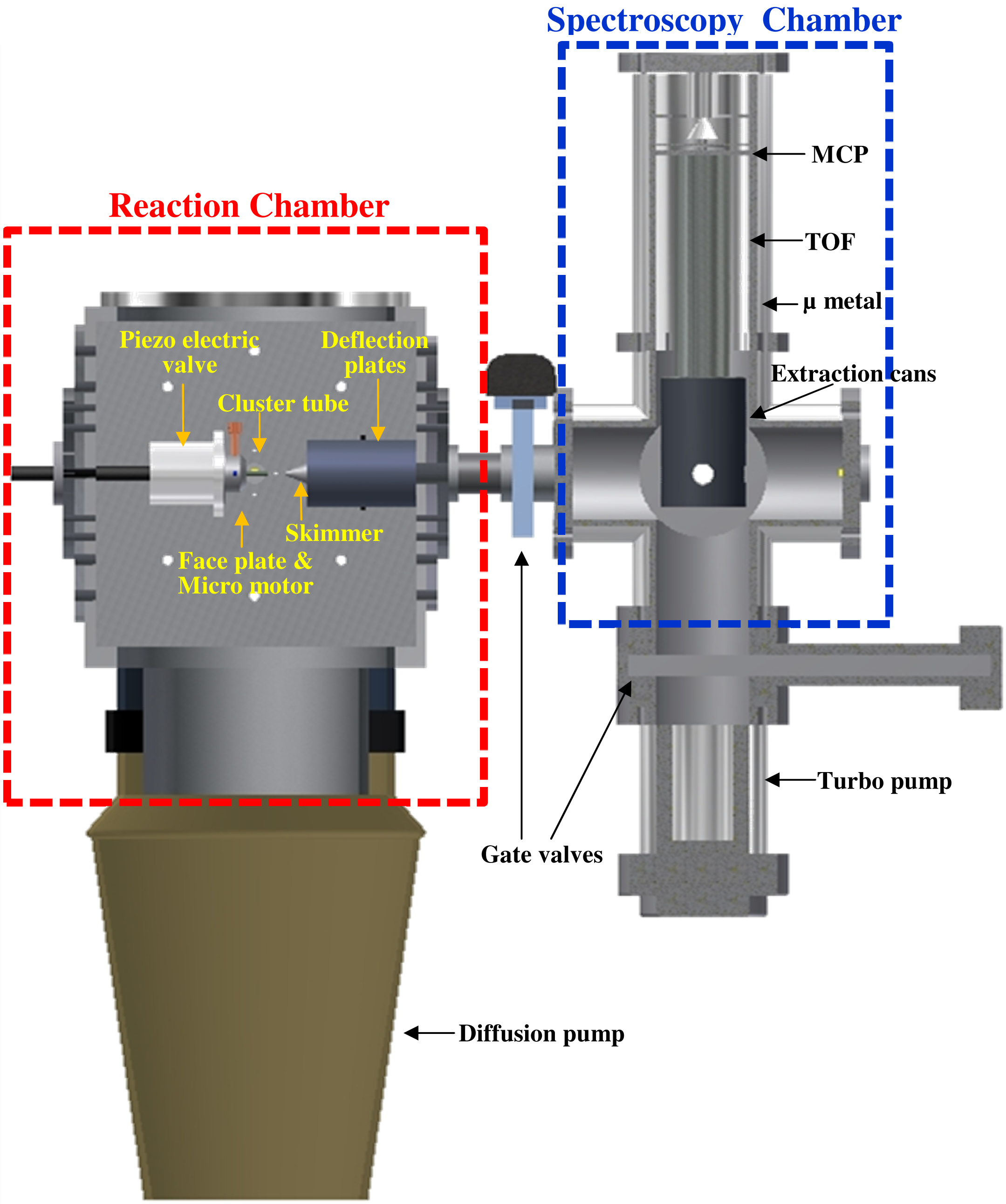

Figure 2.2 The reaction and spectroscopy chambers.

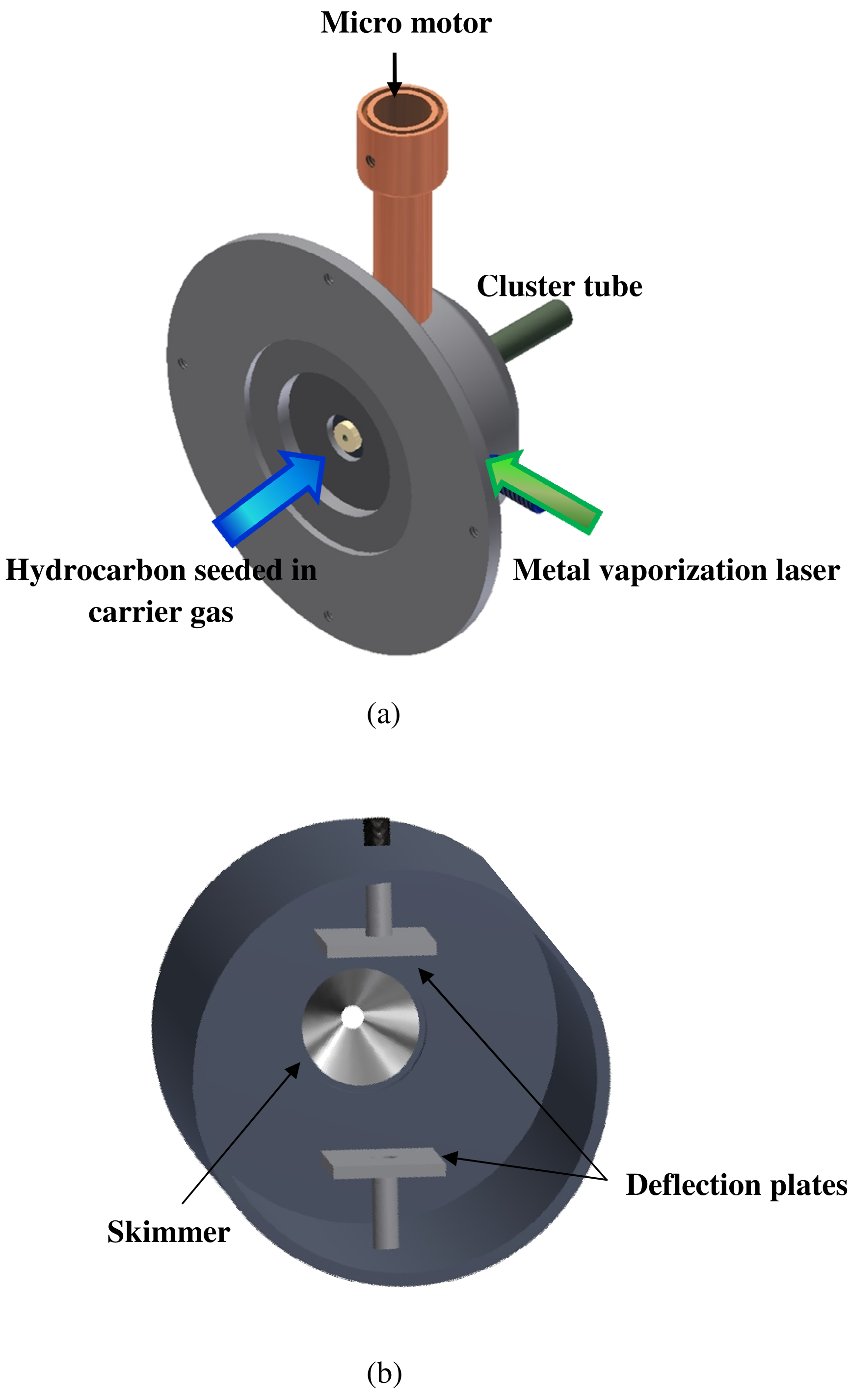

Figure 2.3 The faceplate (a) and skimmer and deflection plates (b) installed in the reaction chamber.

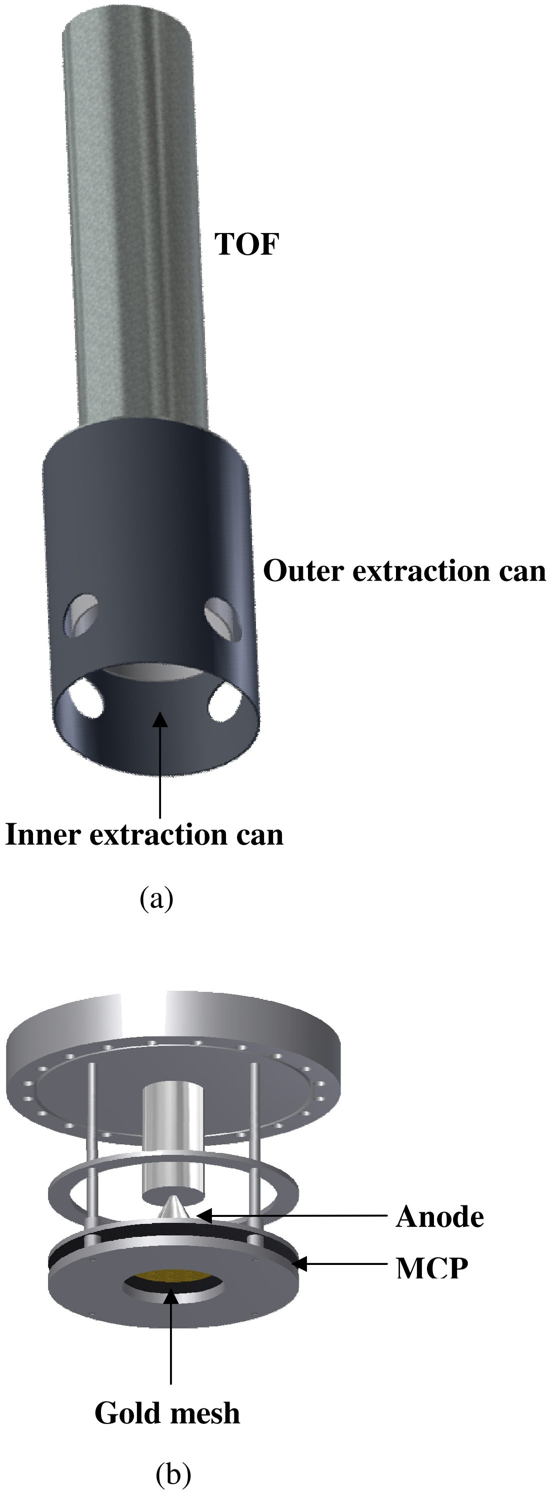

Figure 2.4 The TOF tube and extraction cans (a) and MCP detector (b) in the spectroscopy chamber.

2.1.1 TOF-MS

To detect the cation signals, the TOF tube is grounded, and the outer and inner extraction cans are applied with +2500 V and +1700 V respectively. The high voltages are supplied by the two DC power suppliers (Stanford Research Systems PS350/5000V-25W). Because the two extraction cans are separated by 2.5 cm, a field of 320 V.cm^{-1} is generated across the two cans. This field is used to ionize the Rydberg molecules and extract them towards the MCP detector.

It is assumed that the cations are singly charged. This is a reasonable assumption since the second ionization energies of the complexes are so high that the UV light will not be able to remove the second electrons from the complexes in a single-photon process. To minimize the two or multiple photon processes the UV laser beam is well defocused. The singly charged cations have the same kinetic energies regardless of their masses if they are generated at the same position. Therefore, the mass to charge ratios (m/Z) of the complexes can be easily and accurately calculated using their flight times. Kinetic energy, E_k, of a particle with the charge of q in an electric field of V can be expressed as

$$E_k = Vq$$

Because the ions have the same charge (i.e. singly charged), their kinetic energies must be the same. If two ions have masses of m_1 and m_2 with the velocities of v_1 and v_2 respectively, the following relationship is held.

$$E_k = \frac{1}{2}m_1{v_1}^2 = \frac{1}{2}m_2{v_2}^2$$

since $= {}^{d}/_{t}$, where d=distance, t=time

$$\frac{1}{2}m_1\left(\frac{d}{t_1}\right)^2 = \frac{1}{2}m_2\left(\frac{d}{t_2}\right)^2$$

$$\left(\frac{m_1}{m_2}\right) = \left(\frac{t_1}{t_2}\right)^2$$

Therefore, if we know the mass and the flight time of a reference ion, we then can figure out the mass of the other ion using the its flight time measured with the oscilloscope.

2.1.2 PFI-PIE

A pulsed field ionization-photoionization efficiency (PFI-PIE) curve is used to estimate the ionization energy of a metal complex. In PFI-PIE, a metal complex is first excited to high lying Rydberg states and then ionized by a delayed pulsed field. The delay between the excitation laser and pulsed field for ionization / extraction is about 1 μs. The ion signal of the desired complex is integrated and recorded with respect to the laser wavenumber. If the photon energy is below the ionization threshold of a complex, the ion signal intensity should be zero or near zero. On the other hand, if the photon energy is above the ionization threshold of the complex, the ion signal exhibits a significant increase in the intensity. The intersecting point of the "zero" signal baseline and the line through the signal onset provides an estimate for the ionization energy (IE) of the complex.

2.1.3 MATI Experimental Setup

The timing of the MATI experiment is controlled by two digital delay generators (Stanford Research Systems, DG535 and DG645), and the time sequence is presented in Figure 2.7. The MATI experiment begins at T_0 by triggering the piezoelectric valve to generate gas pulses. Then, the flash lamp of the Nd:YAG laser for vaporization (Lumonics YM-800, 532 nm) is triggered at T_1 and the Q-switch of the vaporization laser is triggered internally at T_2. For this laser, the time difference between the flash lamp and Q-switch (T_2-T_1) is about 140 μs. To synchronize the laser pulses with the gas pulses, the time difference between T_1 and T_0 must be optimized. The flash lamp and Q-switch of the Nd:YAG laser for excitation (Continuum Surelite II) are triggered externally at T_3 and T_5, respectively. Because both flash lamp and Q-switch are triggered externally, the time difference between these two triggers (T_5-T_3) can easily be changed to optimize the power of the laser output. The optimal time delay of the Q-switch trigger from the flash lamp trigger of this laser is about 174 μs. About 300-400 ns prior to the Q switch trigger (T_5) of the Nd:YAG laser pump for excitation, a pulsed field is turned on and applied between the two extraction cans. This pulsed field is generated by the same high voltage pulsed power supplies for the generation and extraction of the MATI ions (i.e., 320 $V.cm^{-1}$ with +2500 V on the outer can and + 1700 V on the inner can) but triggered at different time (T_4). The residue AC field following the falling edge of this electric pulse is used to stabilize the Rydberg states of the neutral molecules. This residue field is sometime called a scrambling field. Several to tens of microseconds (~ 5-20 μs) after the Q-switch triggering of the excitation pump laser, a field of 320 $V.cm^{-1}$ is applied to ionize the Rydberg state molecules and extract the resultant MATI cations towards the MCP detector. The pulsed power supplies for the 320 $V.cm^{-1}$ field is triggered at T_6. Moreover, a DC voltage of 5-20 V is applied on the inner extraction can to differentiate MATI ions produced by the delayed field ionization from the prompt ions generated by the direct photo-excitation. The prompt ions generated prior to the MATI ions are repelled by the DC voltage on the inner can and arrive later to the MCP detector than the MATI ions of the same mass. Because of their different flight times, the MATI ions are separated from the prompt ions and can be easily recorded without the interference of the latter. The electronic circuit of a voltage divider used to supply the voltages for the MCP detector for the cation detection is shown in Figure 2.5.

2.1.4 ZEKE Experimental Setup

The time sequence of the ZEKE experiment is similar to that of the MATI experiment as shown in Figure 2.5. However, the electric polarities applied on the extraction cans and the MCP detector are different from those in the MATI experiment, and a much smaller field is applied on the extraction cans as well. In the ZEKE experiment, a negative pulse of -3.0 V and 100 ns is applied on the outer can, while the inner can is grounded. This generates a pulsed field of 1.2 $V.cm^{-1}$ between the two cans, and this field is used to ionize the high-lying Rydberg states and extract the ZEKE electrons to the MCP detector. The time delay between the excitation laser and the electric pulse is 5-10 μs. In addition to the electric pulse, a DC field of +0.06 $V.cm^{-1}$ is applied across the two extraction cans to discriminate the kinetic electrons generated by direct photoionization from the ZEKE electrons produced by the delayed field ionization. A DC voltage of 5-10 V is applied on the TOF tube to maximize the electron collection efficiency. The electronic circuit that provides the voltage for the MCP detector for the ZEKE detection is shown in Figure 2.5.

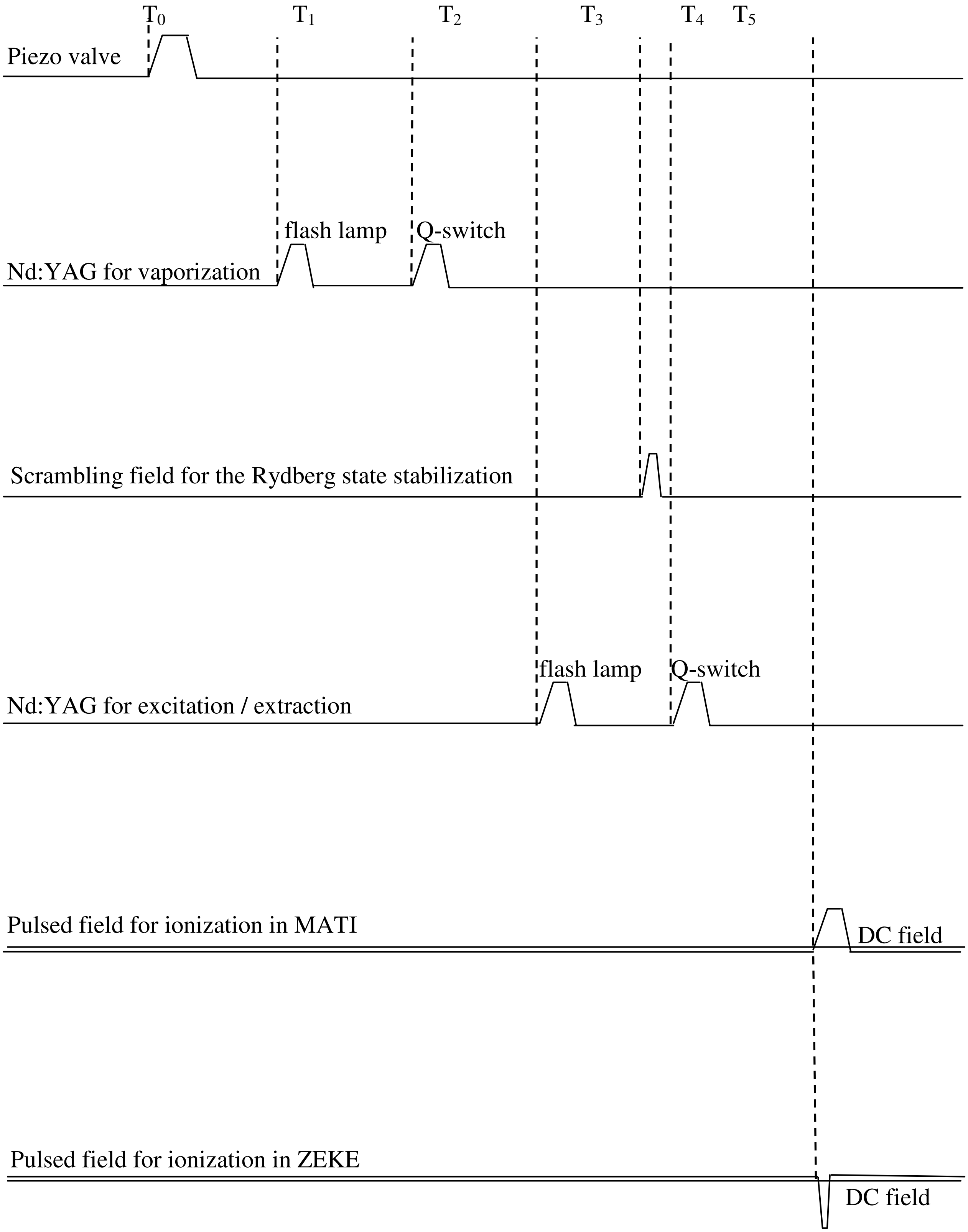

Figure 2.5 Time sequence of the MATI and ZEKE experiment.

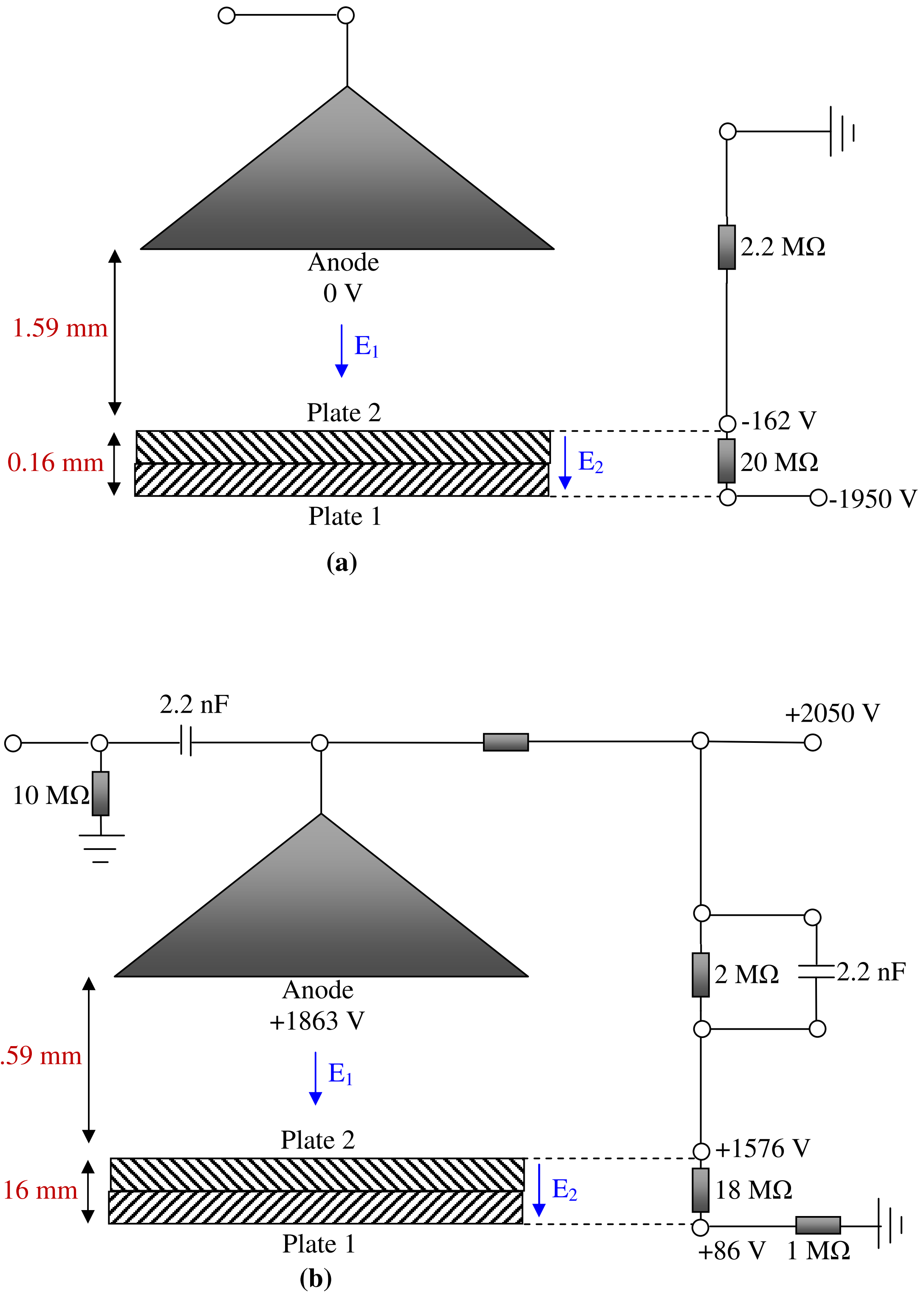

Figure 2.6 The schematic of the electronic circuits for providing the voltages for MCP in cation (a) and electron (b) detections.

2.2 Theoretical Calculations

Geometry optimization and vibrational frequency calculations are carried out using Gaussian 03/09 package[92] installed on the University of Kentucky Hewlett-Packard Superdome Cluster. In these calculations we use Becke's three-parameter hybrid functional[84] with the correlation functional of Lee, Yang, and Parr (B3LYP)[82,83], the triple-split-valence; all electron basis set 6-311+G(d,p)[93,94] for C and H; and effective-core-potential SDD basis set [95] for La. No symmetry restrictions are imposed during the geometry optimizations. For each optimized stationary point vibrational analysis is performed to identify the nature of the stationary point (minimum or saddle point). In the calculations of reaction pathways, the minima connected by a given transition state are confirmed by intrinsic reaction coordinate (IRC) calculations. Single-point energy calculation is carried out on each optimized geometry at CCSD(T) [96] level with aug-cc-pvtz basis[97,98] for C and H, and SDD basis for La to have better estimates for the relative energies. However, the zero point energies are from the B3LYP method.

To simulate the MATI spectrum, multi-dimensional Frank Condon (FC) factors are calculated from the equilibrium geometries, harmonic vibrational frequencies, and normal coordinates of the neutral and ionized complexes. The Duschinsky effect[99] is considered to account for the possible axes rotation from the neutral complex to the cation. Boltzmann distribution is considered to account for the internal energy distribution at different temperatures. Spectral line width broadening is simulated by giving each band a Lorentzian line shape with the experimental linewidth.

CHAPTER 3. LANTHANUM-MEDIATED CYCLO-OLIGOMERIZATION OF ACETYLENE TO BENZYNE AND NAPHTHALENE

3.1 Introduction

Transition metal-mediated catalytic transformation of acetylene is a significant area in organic synthesis. Three major transformation reactions of acetylene are hydrogenation[100], dehydrogenation[101], and polymerization.[100,102-121] These transformation reactions are extensively studied in the surface chemistry of acetylene on the first, second and third row transition metals in the past few decades.[100-112,122,123] Surface reactions are found to be sensitive to the surface crystallography and electronic structure.[122] They also exhibit similar characteristics to the catalytic behavior of transition metal cluster compounds.[122] Among polymerization reactions, cyclization of acetylene has attracted a considerable attention. Moreover, cyclotrimerization of acetylene to form benzene is the most popular topic in the field, and this process has been studied in details in the surface chemistry of Pd.[102,104-112,120,122-124] The reactive intermediates of this process has been characterized by different spectroscopic techniques, such as X-ray photoelectron spectroscopy (XPS), angle-resolved ultraviolet photoelectron spectroscopy (ARUPS), near edge X-ray absorption fine structure (NEXAFS) spectroscopy and high-resolution electron energy-loss spectroscopy (HREELS).[100,102,112,122,124] Reaction kinetics and mechanisms have been studied by the techniques including isotopic labeling or laser-induced thermal desorption combined with Fourier transform mass spectrometry.[106,123] Apart from surface chemistry, matrix isolation infrared spectroscopy (IR) studies[125-127] and gas phase cross molecular beam studies[42,128] have been conducted using bare transition metals. Metal insertion or association complexes of acetylene have been characterized in IR studies. Dehydrogenation of acetylene as a result of the C-H bond activation is the major observation in cross molecular beam studies. Due to single collisions in the cross molecular beam experiments, cyclization of acetylene is not observed. Davis and coworkers have investigated the competitive product formation channels and energetics of the reaction between Y and C_2H_2.[42] Eric D. Glendening has studied the potential energy surfaces of the Y-mediated H and H_2 eliminations of acetylene.[128] However, the studies on the neutral bare transition metal-mediated bond activation of acetylene in the gas phase are still very limited. My work is to characterize the reactive intermediates and products formed by the reaction between bare La metal and C_2H_2 with the aim of better understanding the reaction pathways. The understanding of the detailed reaction pathways helps to design reactions for producing chemo- and regio-selective cyclic products in organic synthesis. We have used MATI spectroscopy in combination with DFT calculations to characterize the reaction intermediates and products in this study and observed both dehydrogenation and cyclization of C_2H_2 promoted by the neutral La atom. Cyclization followed by dehydrogenation has produced La-benzyne and La-napthalene complexes.

3.2 Experimetal and Computational Details

The metal-cluster beam instrument used in this work consists of reaction and spectroscopy vacuum chambers and is described in Chapter 2. The metal-hydrocarbon reaction was carried out in a laser vaporization metal cluster beam source. Acetylene (atomic absorption grade, Western International Gas and Cylinders) was seeded in a He carrier gas with a concentration of 10^{-4} - 10^{-5} in a stainless steel mixing cylinder. La metal atoms were generated by pulsed-laser (Nd:YAG, Continuum Minilite II, 532 nm, 1.0-1.5 mJ/pulse) vaporization of a La rod (99.9%, Alfa Aesar) in the presence of the acetylene/He mixture (40 psi) delivered by a home-made piezoelectric pulsed valve. The metal atoms and gas mixture entered into a clustering tube (2 mm diameter and 2 cm length) where the chemical reactions occurred. The reaction mixture were then expanded into the reaction chamber, collimated by a cone-shaped skimmer (2 mm inner diameter), and passed through a pair of deflection plates. Ionic species in the molecular beam that were formed during laser vaporization were removed by the electric field (100 Vcm^{-1}) applied on the deflection plates. The neutral products were identified by photoionization time-of-flight mass spectrometry. A separate experiment was carried out to confirm that acetylene was activated by La atom rather than the vaporization laser, In this experiment, acetylene was introduced by a second pulsed valve (Parker, Series 9) 3 cm downstream of the laser vaporization point.

Prior to the MATI measurements, photoionization efficiency spectra were recorded to locate the approximate ionization thresholds of the La complexes to simplify the MATI experiment. In the MATI experiment, the metal complexes were excited to high-lying Rydberg states in a single-photon process and ionized by a delayed pulsed electric field. The excitation laser was the same as that for photoionization in the mass spectrometry and photoionization efficiency experiments and was the frequency doubled output of a tunable dye laser (Lumonics HD-500), pumped by the third harmonic output (355 nm) of a Nd:YAG laser (Continuum Surelite II). The laser beam was collinear and counter propagating with the molecular beam. The ionization pulsed field (320 V cm^{-1}) was generated by two high voltage pulse generators (DEI, PVX-4140) and delayed by 10-20 μs from the laser pulse by a delayed pulsed generator (SRS, DG641). A small DC field (6.0 V cm^{-1}) was applied to separate the prompt ions produced by direct photoionization from the MATI ions generated by delayed field ionization. The MATI ion signal was obtained by scanning the wavelength of the tunable dye laser, detected by a dual microchannel plate detector, amplified by a preamplifier (SRS, SR445), averaged by a gated integrator (SRS, SR280), visualized by a digital oscilloscope (Tektronix TDS 3012), and stored in a laboratory computer. Laser wavelengths were calibrated against vanadium atomic transitions in the spectral region.[129] The Stark shift induced by the DC separation field was calculated using the relation of $\Delta IE = 6.1E_f^{1/2}$, where E_f is in V cm^{-1} and ΔE is in cm^{-1}.[130]

Geometry optimization and vibrational frequency calculations were carried out using Gaussian 03 software package.[92] In these calculations we used the Becke's three-parameter hybrid functional with the correlation functional of Lee, Yang, and Parr (B3LYP)[82,83] and 6-311+G(d,p)[93,94] basis set for C and H and effective-core-potential SDD[95] basis set for La. We have extensively used DFT/B3LYP and found this method generally produced adequate results for helping the spectral and structural assignments of organometallic radicals.[131] No symmetry restrictions were imposed in the initial geometry optimization, but symmetry was imposed in the subsequent optimization. For each optimized stationary point, vibrational analysis was performed to identify the nature of the stationary point (minimum or saddle point). In predicting reaction pathways, minima connected by a transition state were confirmed by intrinsic reaction coordinate calculations.

To compare with the experimental MATI spectra, multi-dimensional FC factors were calculated from the equilibrium geometries, harmonic vibrational frequencies, and normal coordinates of the neutral and ionized complexes.[132] In these calculations, the recursion relations from Doktorov et al.[133] were employed, and the Duschinsky effect[99] was considered to account for a possible axis rotation from the neutral complex to the cation. Spectral simulations were obtained considering the experimental linewidth and a Lorentzian line shape. Transitions from excited vibrational levels of the neutral complex were considered by assuming thermal excitation at specific temperatures.

3.3 Results and Discussion

Figure 3.1 displays the TOF-MS spectrum of the products formed from the reaction between laser vaporized La metal and C_2H_2 at 240 nm. The major organometallic complexes generated are LaC_2, LaC_2H_2, LaC_4H_2, LaC_4H_4, LaC_6H_4, LaC_8H_6, $LaC_{10}H_8$ and $LaC_{12}H_{10}$. The reaction products formed in the original and control experiments are identical, though a higher propyne concentration in the control experiment is required to produce comparable ion intensity in the mass spectra. Because propyne bypass the vaporization region in the control experiment, the vaporization laser plays no role for the hydrocarbon activation. The products observed in the TOF-MS spectrum are formed by association, dehydrogenation oligomerization, or oligomerization followed by dehydrogenation. LaC_2 is the smallest complex formed by dehydrogenation . LaC_2H_2 is the π association complex, which is well known in the metal mediated unsaturated hydrocarbon activation. The structure of LaC_2H_2 is characterized by the MATI measurement and is the same as that formed by the La + 1,3-butadiene and La + butene reactions (i.e. La-η^2-HCCH). The spectral and structural assignments of La-η^2-HCCH have been discussed in Chapter 6. The rest of the products are formed by either oligomerization or oligomerization followed by dehydrogenation. The structures and electronic states of LaC_6H_4 and $LaC_{10}H_8$ will be discussed in this Chapter.

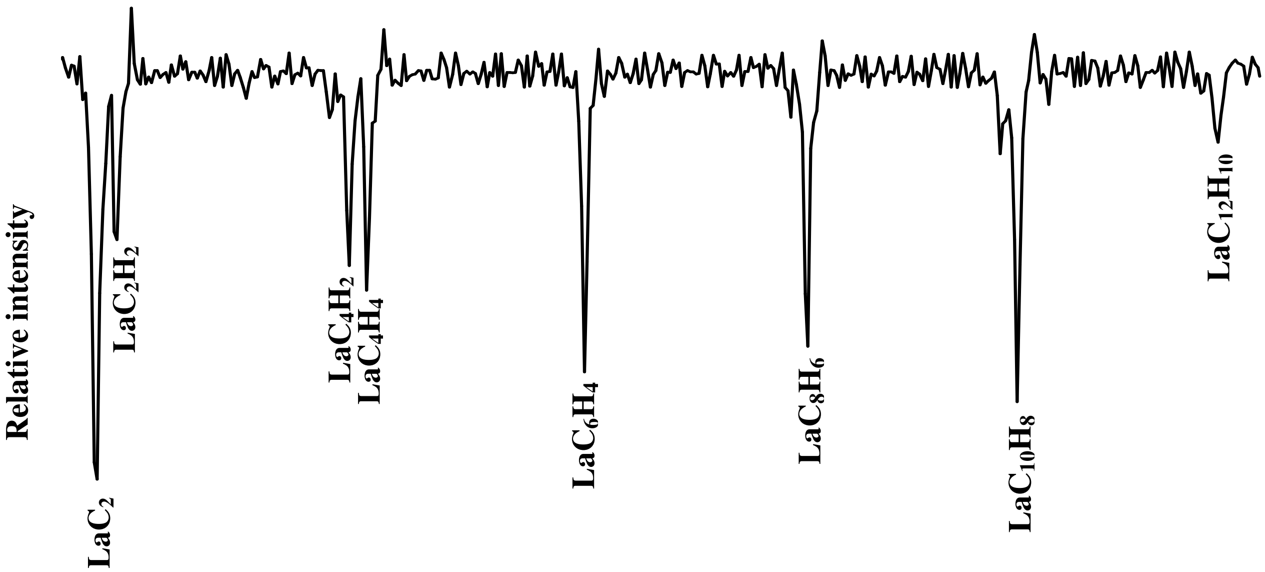

Figure 3.1 TOF-MS spectrum of the La + acetylene reaction recorded at the laser ionization wavelength of 240 nm. The seeding concentration of C_2H_2 in He is 10^{-5}.

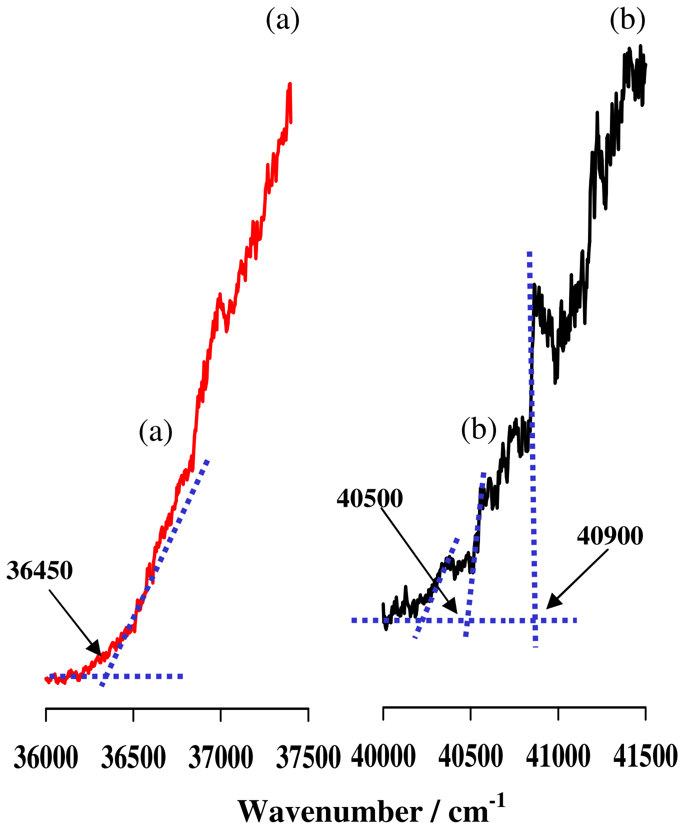

Figure 3.2 PIE spectra of LaC$_{10}$H$_8$ (a) and LaC$_6$H$_4$ (b).

3.3.1 LaC_6H_4

The PIE spectrum of LaC_6H_4 (Figure 3.2(b)) displays a slowly rising signal onset followed by a few sharp onsets separated by about 400 cm^{-1} : the first sharp one is at 40500 (50) cm^{-1} , the second at 40900 (50) cm^{-1} and so on. The positions of the sharp onsets were used to search for and correlate with the MATI signal. Figure 3.4(a) displays the MATI spectrum of LaC_6H_4. The strongest peak located at 40857 (5) cm^{-1}, which matches with the second sharp signal onset of the PIE spectrum, is the origin band of an electronic transition. The major progression of 326 cm^{-1} is originated from this band. The band located at 302 cm^{-1} left to the origin band arises from the transition of a thermally excited vibrational level of the neutral complex. In order to analyze and assign the spectrum in details, we have searched for possible structural isomers of LaC_6H_4. Because of the high degree of unsaturation, the C_6H_4 fragment in the complex tends to have cyclic structures rather than acyclic ones, and the most likely cyclic structure is a six-membered ring. Therefore, benzyne and its two other radical isomers are considered for C_6H_4 in the geometry optimization. Figure 3.3 displays four low-energy isomers of LaC_6H_4 and Table 3.1 summarizes the point groups, relative energies and geometries of them in their ground neutral and cationic electronic states. For the lowest energy isomer, the excited spin states are also considered. La atom has a doublet spin ground state with the electron configuration of $5d^16s^2$. A 5d←6s electron promotion yields an excited electron configuration of $5d^26s^1$. Depending on the electron orientation, both doublet and quartet spin states can be formed from this configuration. This electron configuration has been shown to be preferred in metal-hydrocarbon interactions because of the reduced electron repulsion between the metal 6s and hydrocarbon valence electrons. In the formation of two La-C bonds with C_6H_4, the two 5d electrons would be involved and the 6s electron would remain on the La atom. In this case, the resulted neutral La complex should prefer a doublet spin state. Ionization of the neutral doublet state is expected to yield a singlet ion state by removing the 6s electron. On the other hand, if the La $5d^2 6s^1$ electron configuration remain unchanged upon the formation of LaC_6H_4, the metal complex is expected to be weakly bound, and both doublet and quartet states are possible for the neutral complex. In this case, ionization of the doublet state may yield singlet or triplet ion states and ionization of the quartet state produces a triplet ion state.

As shown in Figure 3.3, La is coplanar and bound with C_1 and C_6 of benzyne in isomers A and is above the six-membered ring in isomers B, C and D. The $^2A_1$ ground state is predicted for isomer A (C_{2v}), ^2A for isomers B and C (C_1), and $^2A'$ for isomer D (C_s). The most stable isomer is predicted to be isomer A followed by isomer B at 2.09 eV, isomer C at 2.28 eV and isomer D at 3.23 eV. The quartet state (^4A) of isomer A is calculated to be 2.35 eV above the doublet ground state ($^2A_1$). The quartet states of the other isomers are not calculated since their ground doublet states already have very high relative energies. Ionization of the doublet state of each isomer yields a preferred singlet ion state by the removal of the La 6s-based electron. Ionization has a very small effect on the geometries of the hydrocarbon fragment in each isomer but significantly reduces the La-C distances (Table 3.1) as a result of an additional charge interaction. It is noted that isomer B is converted to the same cation state as isomer A upon ionization.

By comparison of the spectroscopic measurements with the theoretical calculations, isomer A is found to be responsible for the observed MATI spectrum. Figure 3.3 compares the measured spectrum (Figure 3.3a) and simulated spectrum of the $^1A_1 \leftarrow {}^2A_1$ transition of isomer A (Figure 3.3b). The simulation matches nicely with the experimental spectrum in both band positions and intensities. The IE of the complex is predicted to be 41131

cm^{-1} and measured to be 40857 (5) cm^{-1}. The frequencies of the symmetric La-benzyne stretching mode are calculated as 302 and 325 cm^{-1} and measured as 302 and 326 cm^{-1} in the ionic and neutral states, respectively. The IE and vibrational frequencies from the experiment and calculations are summarized in Table 3.4. Upon ionization, the La-C_1 and La-C_6 bond lengths are significantly reduced, which is consistent with the strong Franck-Condon activity of the La-benzyne stretching mode.

The structure of isomer A is consistent with the solid phase mononuclear transition-metal-benzyne complexes observed crystallographically.[135] The crystal structures reveal that the metal center is coplanar with benzyne ring and is inserted symmetrically into the C-C triple bond to form the two resonance structures, M-benzyne and benzometalla-cyclopropene.[135] Moreover, La-benzyne is the dehydrogenated product of La-benzene. Benzyne is more structurally strained and more reactive and forms much stronger bonds with transition metals than benzene. Our group has previously reported the ZEKE spectrum of La-benzene complex along with the theoretical calculations.[136] La-benzene has a structure with La above the center of slightly bend benzene ring, whereas La-benzyne has a planar structure. Both complexes have C_{2v} symmetry with neutral ground electronic states of $^2A_1$. The IE of La-benzene is 36820 (5) cm^{-1} , 4037 cm^{-1} lower than the IE of La-benzyne. On the other hand, the MATI/ZEKE spectra of both La-benzyne and La-benzene exhibit metal-ligand stretching vibration because of the significant difference of the La-C distances between the neutral and ionic states. Moreover, La-benzene experiences structural changes in the benzene ring upon the ionization and few other active vibrational modes can be observed as a result.

Transition metal-benzyne complexes have been found to be synthetically very useful because of their high reactivities toward other organic and inorganic species.[135,137-143]

Freiser and coworkers have studied Fe^+-benzyne reactions with saturated and unsaturated hydrocarbons and buckminsterfullerene using FTMS and CID techniques.[138,140,141] They have observed alkylation or hydrogenation of Fe^+-benzyne with saturated hydrocarbons and coupling reaction with unsaturated hydrocarbons.[141] For the reactions with acetylene, they observed Fe^+ and C_8H_6 as a result of addition-demetalation.[138] In contrast, we have observed LaC_8H_6, but not C_8H_6, in our TOF-MS spectrum. It is possible that C_8H_6 is also formed in our experiment, but is not ionized because the IE of C_8H_6 is beyond the laser energies available to us. In our work, LaC_8H_6 is found to couple with another acetylene molecule to produce $LaC_{10}H_8$.

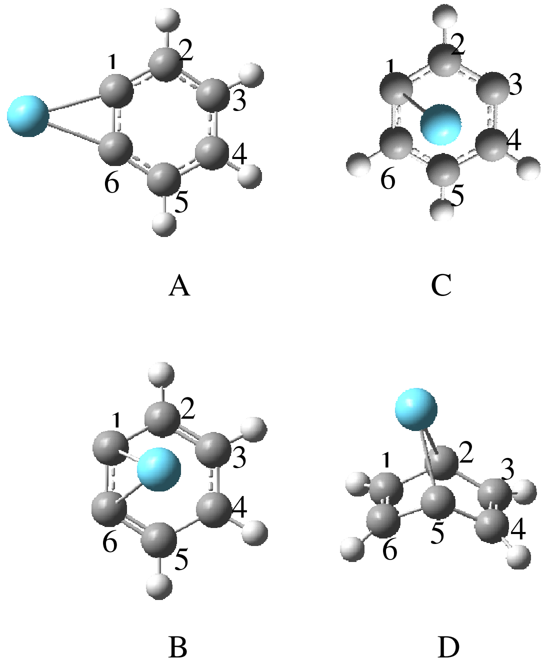

Figure 3.3 Possible cyclic structural isomers of LaC_6H_4.

Table 3.1 Point groups (PG), electronic states (ES), relative energies (E_0, cm^{-1}), bond lengths (Å) and bond angles (degrees) of the LaC_6H_4 isomers calculated at DFT / B3LYP level. The atomic labels are the same as those in Figure 3.3

	Isomer A				**Isomer B**		**Isomer C**		**Isomer D**	
PG	C_{2v}	C_1	C_{2v}	C_1	C_1	C_{2v}	C_1	C_1	C_s	C_s
ES	$^2A_1$	^4A	$^1A_1$	^3A	^2A	$^1A_1$	^2A	^1A	$^2A'$	$^1A'$
E_0	0	16310	41331	56642	16876	41331	18407	59616	26071	65610
La-C_1	2.31	2.52	2.24	2.37	2.20	2.24	2.38	2.35	2.96	2.90
La-C_2					2.68		2.72	2.74	2.33	2.25
La-C_3					2.80		2.71	2.53	3.47	3.33
La-C_4					2.61		2.75	2.60	3.47	3.33
La-C_5					2.73		2.99	2.90	2.33	2.25
La-C_6	2.31	2.69	2.24	2.64	2.52	2.24	2.69	2.62	2.96	2.90
C_1-C_2	1.41	1.41	1.41	1.42	1.48	1.41	1.43	1.42	1.50	1.50
C_2-C_3	1.39	1.39	1.39	1.39	1.39	1.39	1.40	1.38	1.51	1.51
C_3-C_4	1.41	1.41	1.41	1.41	1.44	1.41	1.41	1.42	1.34	1.34
C_4-C_5	1.39	1.40	1.39	1.40	1.46	1.39	1.42	1.43	1.51	1.51
C_5-C_6	1.41	1.39	1.41	1.38	1.38	1.41	1.40	1.40	1.50	1.50
C_1-C_6	1.41	1.32	1.42	1.34	1.43	1.42	1.44	1.45	1.35	1.36
< C_1-La-C_6	35.5	29.2	37.1	30.5	34.5	37.1	32.2	33.4		
< C_2-La-C_5									42.9	45.7

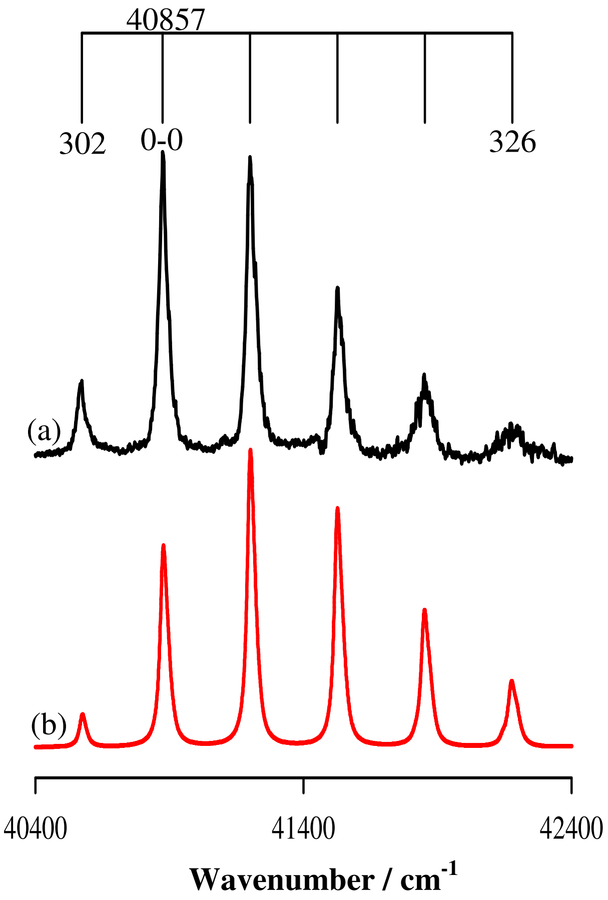

Figure 3.4 MATI spectrum of LaC_6H_4 (a) and the simulated spectrum of the $^1\mathbf{A_1} \leftarrow {}^2\mathbf{A_1}$ transition of La-benzyne (b) at 200K with FWHM of 35 cm^{-1}.

3.3.2 $LaC_{10}H_8$

A slowly rising signal onset, followed by a very sharp signal onset, is shown in the PIE spectrum of $LaC_{10}H_8$ (Figure 3.2(a)). The slowly rising signal originates from the ionization of thermally excited vibrational levels of the neutral $LaC_{10}H_8$ complex. The sharp signal onset around 36450 cm^{-1} corresponds to the first ionization threshold of the complex. Figure 3.6(a) displays the MATI spectrum of $LaC_{10}H_8$. The band located at 36566 cm^{-1} is the origin band of an electronic transition. The energy of this band is comparable with that of the sharp onset in the PIE spectrum. On the right side of the origin band there are 288 cm^{-1} major progression, 78 cm^{-1} short progression, and their combination bands. On the left side of the origin band there are 270 cm^{-1} and 78 cm^{-1} transitions along with their combination bands.

As for LaC_6H_4, we have considered the cyclic structures for $C_{10}H_8$ in the $LaC_{10}H_8$ complex. Figure 3.5 presents six possible isomers predicted by the DFT calculations. Among them, isomer A (La-pentfulvalene) is the most stable one. The next most stable isomer is predicted to be isomer B at 0.15 eV followed by isomer C (La-naphthalene) at 0.55 eV, isomer D (La-azulene) at 0.79 eV, isomer E at 1.84 eV, and isomer F at 3.03 eV. The point groups, electronic states, and relative energies are summarized in Table 3.2. Among the possible electronic transitions of all isomers, the $^1A' \leftarrow {}^2A'$ electronic transition of isomer C (La-naphthalene) provides the best matching simulation to the experimental spectrum as shown in Figure 3.6. The calculated vibrational frequencies match nicely with the measured values. The predicted intensity profile for the 288 cm^{-1} progression is also reasonable. However, the intensity of the 78 cm^{-1} progression is considerably overestimated. To further confirm that La-naphthalene is indeed the isomer responsible for the observed spectrum, we have carried out MATI measurement of $LaC_{10}H_8$ formed by the reaction between La and naphthalene. The

MATI spectrum of La-naphthalene is presented in Figure 3.6(c). Because the MATI spectra in Figure 3.6(a) and 3.6(c) are identical, we are confident that $LaC_{10}H_8$ formed in La + acetylene and La + naphthalene reactions has the same structure (i.e. La-naphthalene). The bond lengths and bond angles of La-naphthalene are summarized in Table 3.3. Upon ionization, La-C bond lengths are reduced, and C_1-La-C_4 bond angle is contracted. The IEs and vibrational frequencies from the MATI measurements and theoretical calculations are listed in Table 3.4. The predicted IE (36998 cm^{-1}) of the complex has a reasonable agreement with the experimental IE (36566 cm^{-1}). Ring bending frequencies of the neutral and cation are measured as 64 and 78 cm^{-1}. La-naphthalene symmetric stretching frequencies are measured as 270 and 288 cm^{-1} for the neutral and cation respectively. The theoretical frequencies are comparable with the experimental frequencies (within ± 10 cm^{-1}).

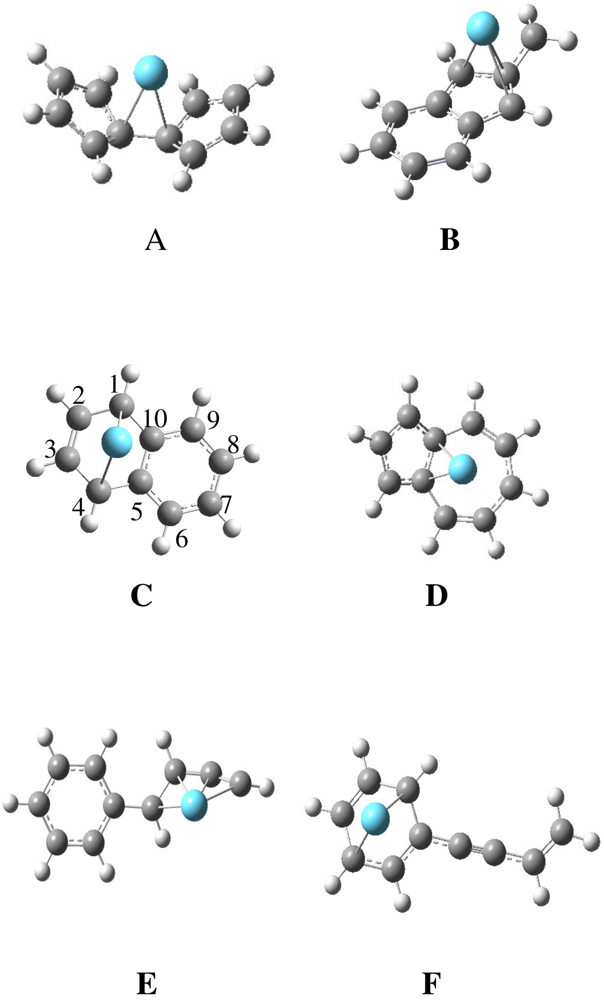

Figure 3.5 Possible cyclic structural isomers of $LaC_{10}H_8$.

Table 3.2 Point groups (**PG**), electronic states (**ES**), and relative energies including vibrational zero point energy correction($\mathbf{E_0}$, cm^{-1}) of the $LaC_{10}H_8$ isomers calculated at the DFT/B3LYP level

Isomers	**PG, ES**	$\mathbf{E_0}$
A	C_{2v}, $^2A_1$	0
A$^+$	C_{2v}, $^1A_1$	39180
B	C_s, $^2A'$	1236
B$^+$	C_s, $^1A'$	41014
C	C_s, $^2A'$	4404
C$^+$	C_s, $^1A'$	41402
D	C_s, $^2A''$	6375
D$^+$	C_s, $^1A'$	41762
E	C_1, ^2A	14814
E$^+$	C_1, ^1A	55280
F	C_1, ^2A	24477
F$^+$	C_1, ^1A	61645

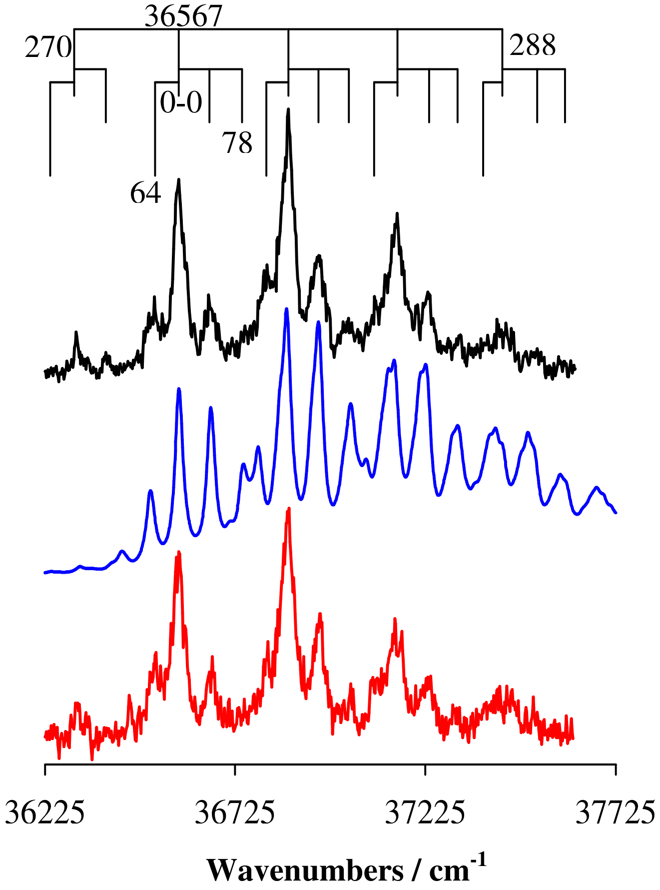

Figure 3.6 MATI spectrum of $LaC_{10}H_8$ (a), the simulated spectrum of the $^1A' \leftarrow {}^2A'$ transition of La-naphthalene (b) and MATI spectrum of La-naphthalene (c). The spectrum in (c) is generated from the reaction between La and naphthalene. The simulation is done at 100K with FWHM of 25 cm^{-1}.

Table 3.3 Bond lengths (Å) and bond angles (degrees) of the neutral and cation states of La-naphthalene calculated at the DFT / B3LYP level. The atomic labels are the same as those in Figure 3.5(c)

	Neutral C_s, $^2A'$	Cation C_s, $^1A'$
La-C_1	2.54	2.47
La-C_2	2.74	2.68
La-C_{10}	2.82	2.69
C_1-C_2	1.45	1.45
C_1-C_{10}	1.47	1.47
C_2-C_3	1.38	1.38
C_5-C_6	1.41	1.41
C_6-C_7	1.39	1.39
C_7-C_8	1.40	1.40
<C_1-La-C_4	68	70

Table 3.4 Adiabatic ionization energies (AIE, cm^{-1}) and vibrational frequencies (cm^{-1}) of La-benzyne and La-naphthalene from the MATI measurements and DFT / B3LYP calculations. The uncertainty of the experimental IE values is 5 cm^{-1}

	MATI	B3LYP
La-benzyne, C_{2v}		
AIE : $^1A_1 \leftarrow {}^2A_1$	40857	41131
La-benzyne symmetric stretching, υ_{10}	302	302
La^+- benzyne symmetric stretching, υ_{10}^+	326	325
La-naphthalene, C_s		
AIE : $^1A' \leftarrow {}^2A'$	36566	36998
Ring bending of neutral, υ_{26}	64	74
Ring bending of cation, υ_{26}^+	78	83
La-naphthalene symmetric stretching, υ_{24}	270	262
La^+-naphthalene symmetric stretching, υ_{24}^+	288	285

Table 3.5 MATI band positions (cm^{-1}) and assignments of La-benzyne and La-napthalene. The uncertainty associated with the band positions is 5 cm^{-1}

La-benzyne		La-naphthalene	
Band position of MATI	Assignment	Band position of MATI	Assignment
40555	10^0_1	36233	$24^0_1 26^0_1$
40857	0^0_0	36297	24^0_1
41183	10^1_0	36375	$24^0_1 26^1_0$
41509	10^2_0	36503	26^0_1
41835	10^3_0	36567	0^0_0
42161	10^4_0	36645	26^1_0
		36791	$24^1_0 26^0_1$
		36855	24^1_0
		36933	$24^1_0 26^1_0$
		37079	$24^2_0 26^0_1$
		37143	24^2_0
		37221	$24^2_0 26^1_0$
		37431	24^2_0

3.3.3 Reaction Pathways for the Formation of LaC_6H_4 and $LaC_{10}H_8$

We were able to confirm that the bond activation of acetylene is La metal mediated, rather than the vaporization laser assisted. The reaction products formed in the original and control experiments were identical, though a higher acetylene concentration in the latter experiment was required to produce a comparable ion intensity in the mass spectra. Since acetylene bypassed the vaporization region in the control experiment, vaporization laser played no role for the hydrocarbon activation. This observation should not be surprising since the laser flux used in metal vaporization is rather low and acetylene (like other small unsaturated hydrocarbon compounds) has low absorption cross sections for visible light.

$La + 3\ C_2H_2 \rightarrow LaC_6H_4 + H_2$

$LaC_6H_4 + 2\ C_2H_2 \rightarrow LaC_{10}H_8$

The metal mediated oligomerization of acetylene generates LaC_6H_4 and $LaC_{10}H_8$ as shown above. A possible reaction pathway for the La-benzyne formation is shown in Figure 3.7, and the structures of the stationary points along the reaction pathway are shown in Figure 3.8. The overall process is exothermic, that is, all the intermediates and transition states are located below the reactants in energy. The process is initiated with the formation of a well known π-association complex, LaC_2H_2. The reaction of LaC_2H_2 with a second C_2H_2 molecule form IM3, a five-membered metallacycle, via IM2 and TS1. TS1 has an imaginary frequency associated with a vibrational mode that brings the internal C atoms closer to each other. A PdC_4H_4 metallacycle similar to IM3 has also been identified previously in the formation of benzene on a Pd surface.[122] This five-membered metallacycle (IM3) reacts with a third C_2H_2 molecule to form a seven-membered metallacycle (IM5) via TS2. The vibration related to the imaginary frequency of TS2 is the one that brings the third C_2H_2 molecule towards the five-membered metallacycle.

La-benzyne is then formed by the consecutive elimination of two H atoms through the steps of TS3→IM6→IM7→TS4.

La-naphthalene is formed by C-C bond coupling reaction between La-benzyne and two C_2H_2 molecules as shown in Figures 3.9 and 3.10. The first C_2H_2 insertion into a La-C bond of La-benzyne forms La-C_8H_6 (IM10) via the initial information of (C_2H_2)La(benzyne) (i.e., IM9 and TS5). La-C_8H_6 is observed in the TOF-MS spectrum, even though its MATI signal is very weak. The failure of the MATI measurements for this species is likely due to large structural differences between the neutral an ion states as shown by a slow ion signal onset in its PIE spectrum (not shown in this report). The second C_2H_2 insertion yields IM12. As in the first insertion step, this step also involves C_2H_2 addition to the La center (i.e., IM11 and TS6) initially. In the final step, coupling reaction occurs to form La-naphthalene via IM12 and TS7.

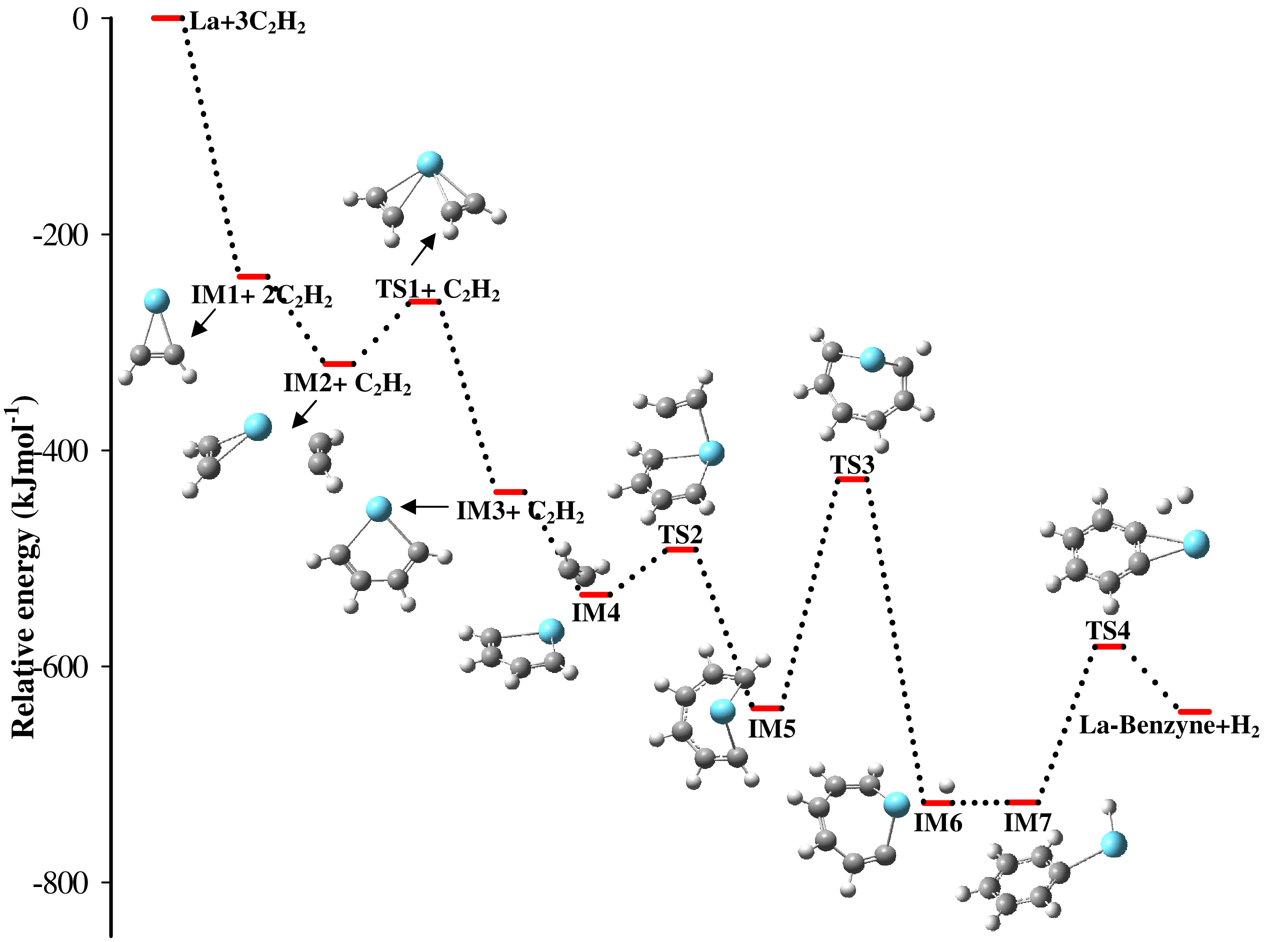

Figure 3.7 Reaction pathway for the formation of La-benzyne from the reaction between La and C_2H_2 at the DFT/B3LYP level. TS: Transition States, IM: Intermediates.

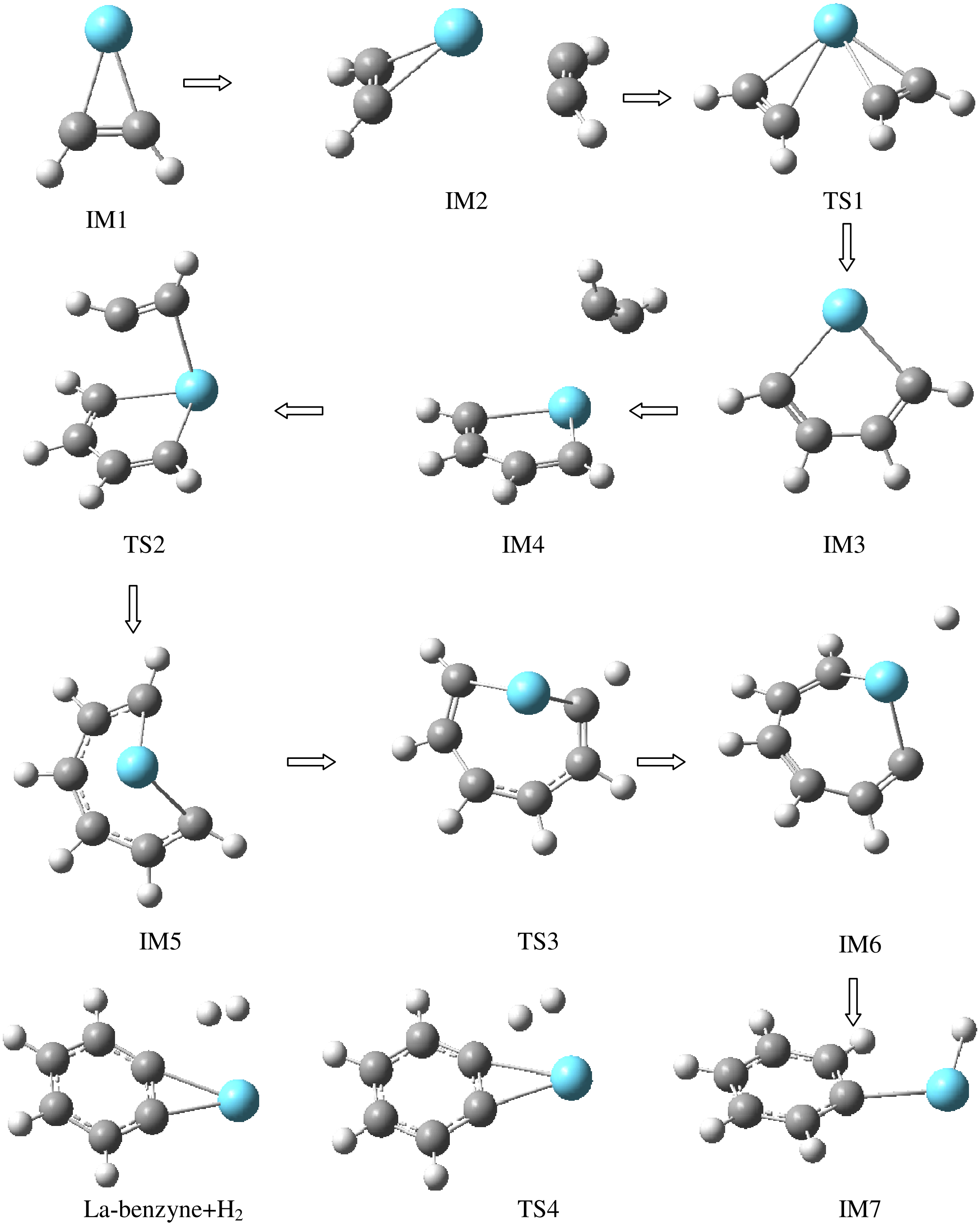

Figure 3.8 Stationary points of the reaction pathway for the formation of La-benzyne from the reaction between La and C_2H_2. TS: Transition States, IM : Intermediates.

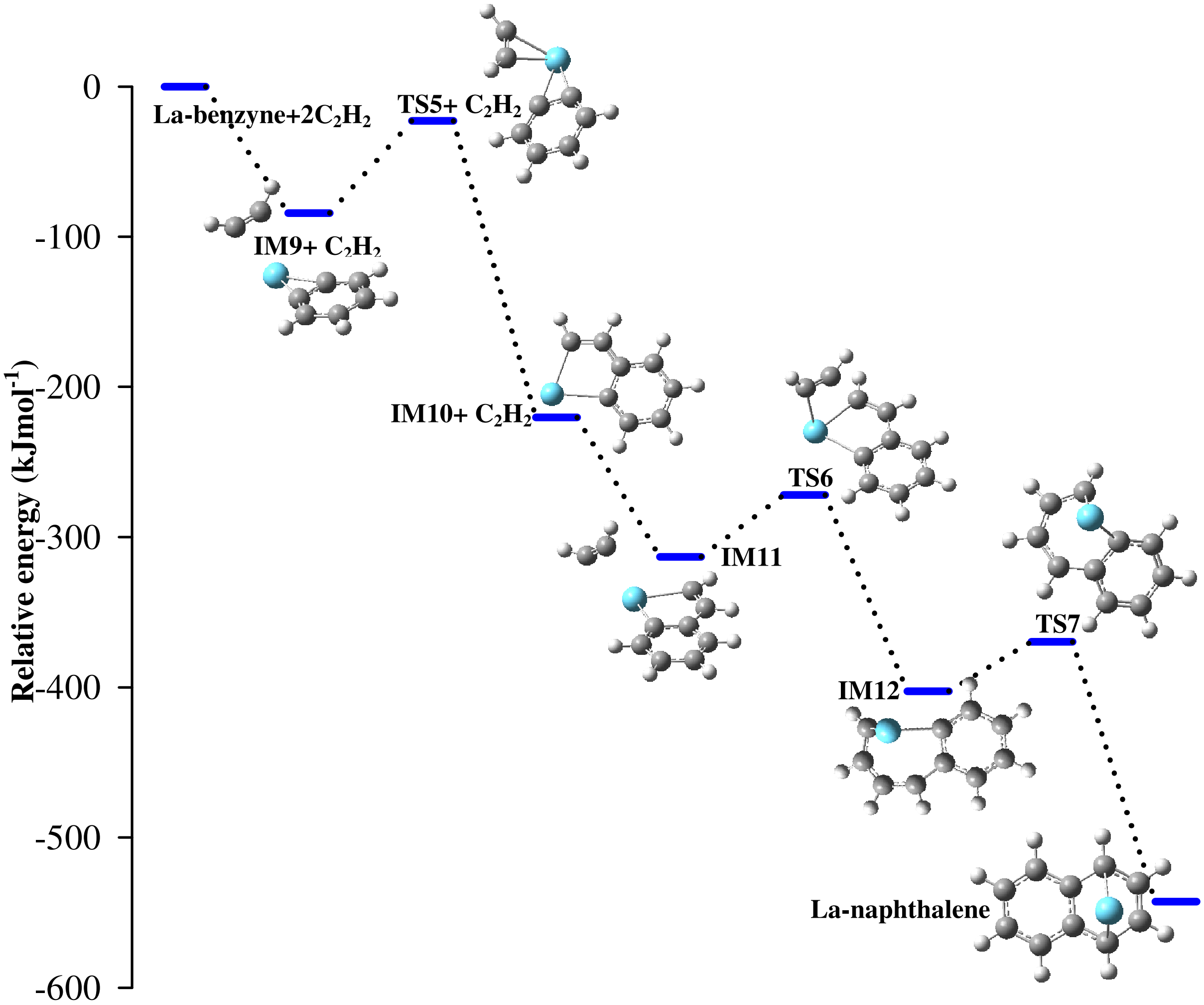

Figure 3.9 Reaction pathway for the formation of La-naphthalene from the reaction between La-benzyne and C$_2$H$_2$. TS: Transition States, IM: Intermediates.

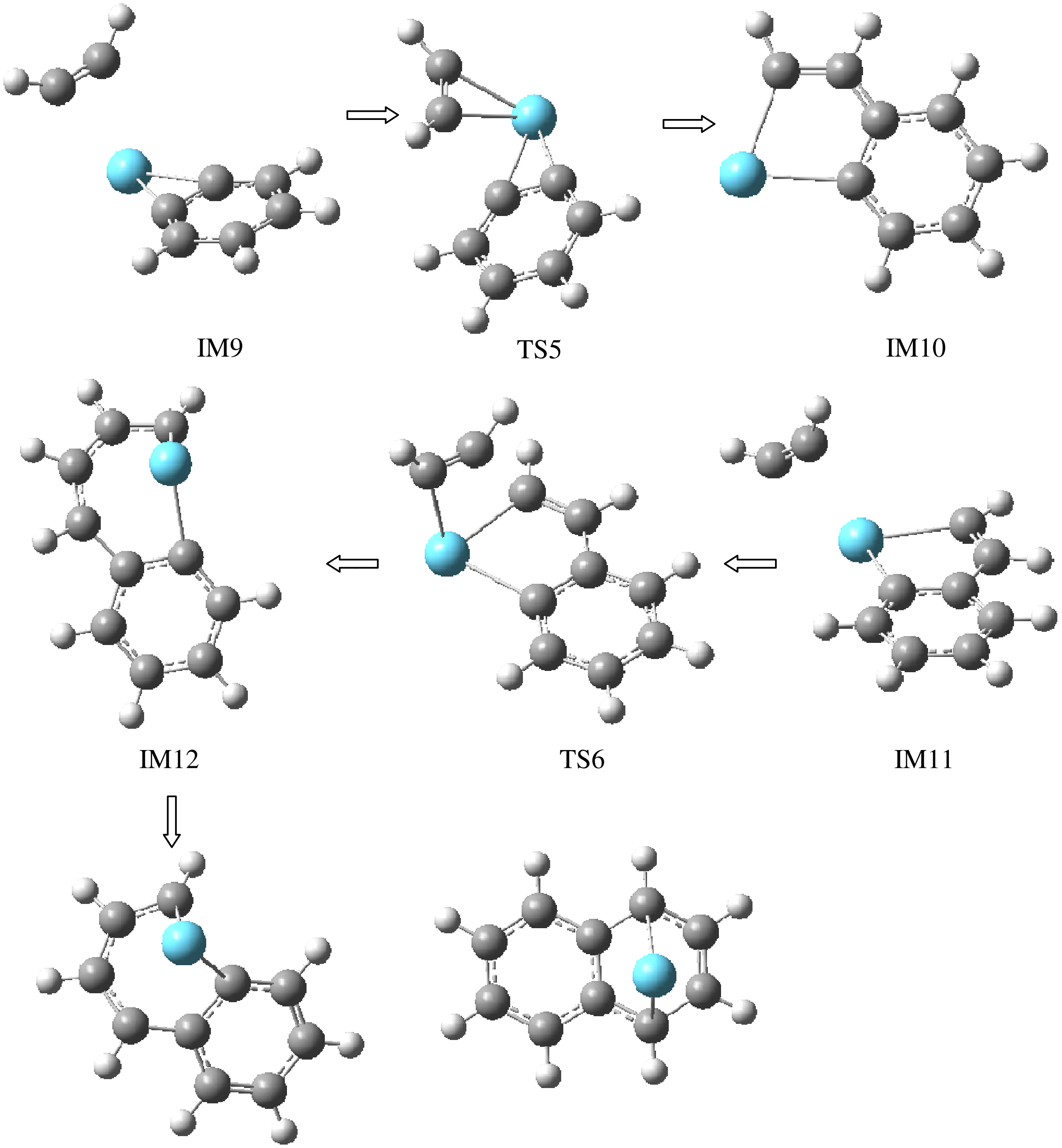

IM9 TS5 IM10

IM12 TS6 IM11

TS7 La-naphthalene

Figure 3.10 Stationary points of the reaction pathway for the formation of La-naphthalene from the reaction between La-benzyne and C_2H_2. TS: Transition States, IM: Intermediates.

3.4 Conclusions

LaC_2, LaC_2H_2, LaC_4H_2, LaC_4H_4, LaC_6H_4, LaC_8H_6, $LaC_{10}H_8$ and $LaC_{12}H_{10}$ are observed in the gas phase reaction of La with acetylene. The structures of LaC_6H_4 and $LaC_{10}H_8$ are determined as La-benzyne and La-naphthalene by vibrationally resolved MATI spectra for the first time. The experimental IEs of the complexes are measured to be 40875 cm^{-1} for La-benzyne and 36566cm^{-1} for La-naphthalene. The ground electronic states of La-benzyne and La-naphthalene are identified as $^2A_1$ and $^2A'$, respectively. The most active vibrational mode observed in the MATI spectra of the two complexes is the metal-hydrocarbon symmetric stretching mode. On the basis of the proposed reaction pathways, the formation of both La-benzyne and La-naphthalene is exothermic and thus thermodynamically favorable.

CHAPTER 4. LANTHANUM-MEDIATED C-H BOND ACTIVATION OF PROPYNE AND IDENTIFICATION OF LaC_3H_2 ISOMERS

Parts of this chapter are taken from "Lanthanum-mediated C-H bond activation of propyne and identification of $La(C_3H_2)$ isomers " *J. Phys. Chem. A* 2015, *119*, 2857. Copyright 2015 American Chemical Society.

4.1 Introduction

Hydrocarbons are not only the major constituents of petroleum and natural gas, but also the most abundant, low-cost stock for functionalized organic chemicals. Because of their chemical inertness, the transformation of hydrocarbons to value-added products requires activation of thermodynamically stable C-H and C-C bonds. The goal of designing selective and effective reagents for such reactions has stimulated extensive research activities on metal-medicated hydrocarbon activation in condensed[1,2,4,14,17,31,32] and gas[5,11,25,28,29,33-46,51-53,144,145] phases. Gas-phase studies provide an efficient means to investigate intrinsic reactivity patterns, reaction pathways, and structure-reactivity relationships of crucial intermediates and to distinguish the intrinsic chemistry from solvation or counter ion effects. Solvation potentially changes the relative energies of the reactants, products, and most importantly, transition states. If it alters the energy landscape of a reaction, differences are expected between the gas and solution phases; on the other hand, if the solvent effect does not change the overall shape of the potential energy surface of the reaction, parallels may exist between the two phases. Although connections remain to be found and rationalized for reactions in different environments, similarities have been reported for alkane reactions with radicals and on metal surfaces.[146-148] An approach for searching for the connections is to examine systems in different phases to allow for detailed comparisons.

Although a large body of experimental measurements for gas-phase metal-mediated hydrocarbon activation is available in literature, structural arrangements and electronic states of intermediates and products formed in such reactions are still hard to find in spite of their importance in devising plausible reaction pathways. For propyne ($CH_3C{\equiv}CH$) reactions with metal ions or atoms, The Ohanessian group observed W^+-induced dehydrogenation and the formation of a series of $WC_{3n}H_{2n}^+$ ions using Fourier transform ion cyclotron resonance mass spectrometry.[149] They proposed three possible isomers for the smallest complex WC_3H_2, each containing a W-C double bond, but were not able to establish the lowest energy structure. On the other hand, Bohme group observed no bond breaking but sequential association of propyne with Fe^+ in a selected-ion tube apparatus.[150] More recently, the Davis group observed MC_3H_2 (M = Y, Zr, Nb, and Mo) formed by H_2 elimination of propyne in a crossed molecular beam experiment.[5] Their analysis of possible C-H bond activation mechanisms leads to two likely isomers of MC_3H_2: M-$CCCH_2$ and M-HCCCH. Following the elegant crossed-molecule beam study, Li et. al reported a density functional theory (DFT) study of the C-C and C-H bond activation of propyne by Y atom.[6] They predicted that a concerted H_2-elemination path had no energy barrier and the dehydrogenation resulted in three possible isomers of YC_3H_2 in doublet ground states: Y(HCCCH) (C_2), Y($CCCH_2$) (C_s), and Y-$CCCH_2$ (C_{2v}). However, a reliable prediction of the electronic states and molecular structures of organotransition metal radicals is complicated by the existence of multiple low-energy structural isomers of each complex and high-dense low-energy states of each isomer. Therefore, a reliable identification of structural isomers and electronic states generally requires the confirmation by spectroscopic measurements, especially high-resolution spectroscopic techniques.

Our attempt in this work is to investigate the bond activation of propyne by La metal atom. We report two low-energy isomers of LaC_3H_2: (η^2-propadienylidene lanthanum) [La(η^2-$CCCH_2$)] and deprotiolanthanacyclobutadiene [La(HCCCH)]. These isomers are formed by the reaction of La atom with propyne in a molecule beam source and characterized by mass-analyzed threshold ionization (MATI) spectroscopy combined with electronic structure calculations and spectral simulations. To our knowledge, this work represents the first spectroscopic identification of the structural isomers for a MC_3H_2 (M = metal) radical formed in a neutral metal atom-mediated small hydrocarbon activation reaction.

4.2 Experimetal and Computational Details

The metal-cluster beam instrument used in this work consists of the reaction and spectroscopy vacuum chambers and was described in Chapter 2. The metal-hydrocarbon reaction was carried out in laser vaporization metal cluster beam source. $CH_3C{\equiv}CH$ (95% , GFS Chemicals) or $CD_3C{\equiv}CD$ (99.4 atom% D, CDN isotopes) was seeded in a He carrier gas with a concentration of 10^{-4} - 10^{-5} in a stainless steel mixing cylinder. La metal atoms were generated by pulsed-laser (Nd:YAG, Continuum Minilite II, 535 nm, 1.0-1.5 mJ/pulse) vaporization of a La rod (99.9%, Alfa Aesar) in the presence of the hydrocarbon/He mixture (40 psi) delivered by a home-made piezoelectric pulsed valve. The metal atoms and gas mixture entered into a clustering tube (2 mm diameter and 2 cm length) where chemical reaction occurred. The reaction mixture were then expanded into the reaction chamber, collimated by a cone-shaped skimmer (2 mm inner diameter), and passed through a pair of deflection plates. Ionic species in the molecular beam that were formed during laser vaporization were removed by the electric field (100 Vcm^{-1}) applied on the deflection plates. The neutral products were identified by photoionization time-of-flight mass spectrometry. A separate experiment was carried out to confirm that propyne was activated by La atom rather than the vaporization laser, In this experiment, propyne was introduced by a second pulsed valve (Parker, Series 9) 3 cm downstream of the laser vaporization point.

Prior to the MATI measurements, photoionization efficiency spectra of LaC_3H_2 were recorded to locate the approximate ionization threshold of the La complex to simplify the MATI experiment. In the MATI experiment, the LaC_3H_2 complex was excited to high-lying Rydberg states in a single-photon process and ionized by a delayed pulsed electric field. The excitation laser was the same as that for photoionization in the mass spectrometry and photoionization efficiency experiments and was the frequency doubled output of a tunable dye laser (Lumonics HD-500), pumped by the third harmonic output (355 nm) of a Nd:YAG laser (Continuum Surelite II). The laser beam was collinear and counter propagating with the molecular beam. The ionization pulsed field (320 V cm^{-1}) was generated by two high voltage pulse generators (DEI, PVX-4140) and delayed by 10-20 μs from the laser pulse by a delayed pulsed generator (SRS, DG641). A small DC field (6.0 V cm^{-1}) was applied to separate the prompt ions produced by direct photoionization from the MATI ions generated by delayed field ionization. The MATI ion signal was obtained by scanning the wavelength of the tunable dye laser, detected by a dual microchannel plate detector, amplified by a preamplifier (SRS, SR445), averaged by a gated integrator (SRS, SR280), visualized by a digital oscilloscope (Tektronix TDS 3012), and stored in a laboratory computer. Laser wavelengths were calibrated against vanadium atomic transitions in the spectral region.[129] The Stark shift induced by the DC separation field was calculated using the relation of $\Delta IE = 6.1E_f^{1/2}$, where E_f is in V cm^{-1} and ΔE is in cm^{-1}.[130]

Geometry optimization and vibrational frequency calculations were carried out using Gaussian 03 software package.[92] In these calculations we used the Becker's three-parameter hybrid functional with the correlation functional of Lee, Yang, and Parr (B3LYP)[82,83] and 6-311+G(d,p)[93,94] basis set for C and H and effective-core-potential SDD[95] basis set for La.

We have extensively used DFT/B3LYP and found this method generally produced adequate results for helping the spectral and structural assignments of organometallic radicals.[131] No symmetry restrictions were imposed in the geometry optimizations. For each optimized stationary point, vibrational analysis was performed to identify the nature of the stationary point (minimum or saddle point). In predicting reaction pathways, minima connected by a transition state were confirmed by intrinsic reaction coordinate calculations.

To compare with the experimental MATI spectra, multi-dimensional FC factors were calculated from the equilibrium geometries, harmonic vibrational frequencies, and normal coordinates of the neutral and ionized complexes.[132] In these calculations, the recursion relations from Doktorov et al.[133] were employed, and the Duschinsky effect[99] was considered to account for a possible axis rotation from the neutral complex to the cation. Spectral simulations were obtained using the experimental linewidth and a Lorentzian line shape. Transitions from excited vibrational levels of the neutral complex were considered by assuming thermal excitation at specific temperatures.

4.3 Results and Discussion

Figure 4.1 displays the TOF mass spectrum of the products formed by the reaction between laser vaporized La atom and $CH_3C{\equiv}CH$ at the laser ionization wavelength of 220 nm. The observed major products are LaC_3H_2, LaC_5H_4, LaC_6H_6 and LaC_9H_{10}. Even though we have tried to perform the MATI spectroscopy on all four species, we have been successfull only in LaC_3H_2 and LaC_6H_6. The ion intensity of LaC_5H_4 was too small to collect a PIE spectrum or a MATI spectrum and we were not able to increase the production of LaC_5H_4 by changing the seeding concentration of propyne. Attempts to record the MATI spectrum of LaC_9H_{10} were also unsuccessful due to the slow ion signal onsets in the PIE spectrum.

Therefore, the focus of this chapter is the spectroscopy and structure of LaC_3H_2 and its deuterated analogue.

4.3.1 LaC_3H_2 and LaC_3D_2

Figure 4.2 displays the PIE spectra of LaC_3H_2(a) and LaC_3D_2(b). There is a slowly rising signal onset followed by a very sharp one in each spectrum. The PIE spectra of LaC_3H_2 and LaC_3D_2 show their sharp onsets at 42950 (50) and 42975 (50) cm^{-1} respectively. Figure 4.3 presents the MATI spectra of LaC_3H_2 (a) and LaC_3D_2 (b) seeded in a helium carrier gas. The spectrum of LaC_3H_2 displays the strongest band at 42953 (5) cm^{-1} which matches with the sharp signal onset of the PIE spectrum. This band arises from the vibronic transition (0-0 band labeled in Figure 4.3) between the ground states of the neural complex and singly charged cation. The band position corresponds to the adiabatic ionization energy (AIE) of the neutral species. A small band is measured at 408 cm^{-1} below the origin band and a short 425 cm^{-1} progression is observed above. Besides, the spectrum of LaC_3H_2 exhibits a strong band at 43609 (5) cm^{-1}, 656 cm^{-1} above the strongest band. Since no other bands with a 656 cm^{-1} interval is observed in the spectrum, this band is unlikely from vibrational excitation. In another word, if this band were a vibrational band, at least an additional band at ~ 2 x 656 cm^{-1} is expected on the basis of the Franck-Condon (FC) principle. On the other hand, the spectrum shows a short progression of 548 cm^{-1} (with two intervals) above the 43609 cm^{-1} band and a small band at 456 cm^{-1} below. Therefore, the 43609 cm^{-1} band is likely the origin band of another electronic transition of the same structural isomer or of an electronic transition of a different isomer.

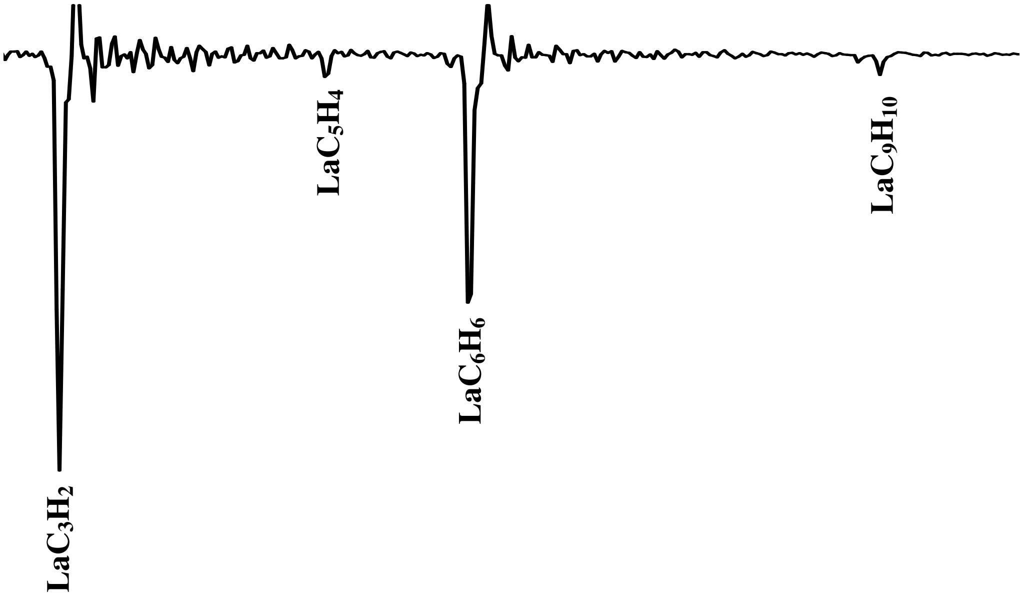

Figure 4.1 TOF-MS spectrum of the La + $CH_3C{\equiv}CH$ reaction recorded at the laser ionization wavelength of 220 nm. The seeding concentration of $CH_3C{\equiv}CH$ in He is 10^{-5}.

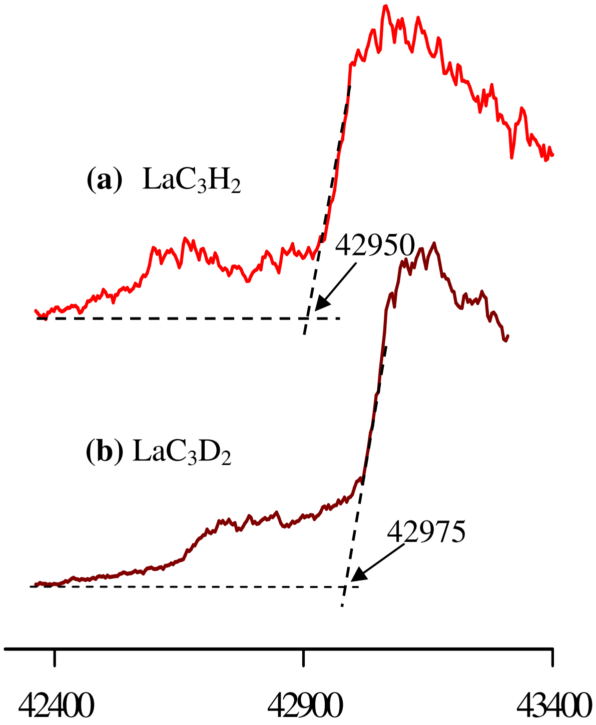

Figure 4.2 PIE spectra of LaC_3H_2 (a) and LaC_3D_2 (b).

Since the IE of the complex (42953 cm^{-1}) is lower than that of La atom (44980 cm^{-1}),[151] the La-C_3H_2 bonding is stronger in the ion than in the neutral state (by 2027 cm^{-1}). Because of a short FC spectral profile, the electron removed by ionization is expected to be weakly bound in the highest occupied molecular orbital.

The spectral profile of LaC_3D_2 (Figure 4.3b) is very similar to that of its parent complex. The strongest band (42959 cm^{-1}) is shifted by 6 cm^{-1} compared to the strongest band of LaC_3H_2, and the positions of the second strongest bands (43609 cm^{-1}) are the same in both parent and deuterated species. Deuteration reduces the vibrational intervals of 425/408 cm^{-1} to 390/385 cm^{-1}. However, the reduction is much smaller for the 548/456 cm^{-1} modes, as the corresponding intervals for the deuterated species are 540/456 cm^{-1}. At least two conclusions can be drawn from the comparison of the LaC_3H_2 and LaC_3D_2 spectra. First, deuteration has a very similar effect on the ionization energy. Second, the 425/408 cm^{-1} vibrations must involve considerably larger H/D displacements than the 548/456 cm^{-1} vibrations.

Figure 4.4 presents the structures of propyne and possible LaC_3H_2 isomers. The formation of LaC_3H_2 is the result of H_2 elimination of propyne. The 1,3-dehydrogenation produces La(η^2-$CCCH_2$) with La in an η^2 binding mode or La-$CCCH_2$ with La binding to a single carbon atom and LaCCC in a linear configuration. The 3,3-dehydrogenation leads to the formation of the metallacycle, La(HCCCH). Table 4.1 lists the electronic states and relative energies of La(η^2-$CCCH_2$), La(HCCCH), and La-$CCCH_2$ predicted by DFT/B3LYP calculations. In La(η^2-$CCCH_2$) and La(HCCCH), La atom is coordinated with two C atoms by sharing a valence electron with each C. Since a La atom has three valence electrons ($4d^1 6s^2$), only one electron is left unpaired on the metal center after the formation of the two La-C bonds. Therefore, the most stable electronic state of these two isomers is expected to be in a doublet electronic state. In La-$CCCH_2$, the La atom is doubly bound to one C atom and the La-C double bond length is much shorter than those in La(η^2-$CCCH_2$) and La(HCCCH) as shown in Table 4.2. Thus, the ground state of La-$CCCH_2$ is also expected to be a doublet state. Indeed, the $^2A'$ ground state is predicted for La(η^2-$CCCH_2$) (C_s), ^2A for La(HCCCH) (C_2), and $^2A_1$ for La-CCCH (C_{2v}). The most stable isomer in the doublet ground state is predicted to be La(η^2-$CCCH_2$) (C_s), followed by La(HCCCH) (C_2) at 0.09 eV, and La-$CCCH_2$ (C_{2v}) at 0.67 eV. The quartet states are calculated to be 1.14 and 0.99 eV above the doublet ground states of La(HCCCH) and La-$CCCH_2$, respectively. For La(η^2-$CCCH_2$), the geometry of the quartet state is converted to that of La-$CCCH_2$. Ionization of the doublet state of each isomer yields a preferred singlet ion state by the removal of the La 6s-based electron in the neutral state. Ionization has a very small effect on the geometries of the organic fragment in each isomer but significantly reduces the La-C distances as a result of an additional charge interaction.

Two isomers of LaC_3H_2: La(HCCCH) and La(η^2-$CCCH_2$), are determined by comparison of the spectroscopic measurements with the theoretical calculations. They are two lowest energy isomers predicted by theory. Figure 4.5 compares the measured spectrum (Figure 4.5a) and simulated spectra of La(HCCCH) (Figure 4.5b, pink trace) and La (η^2-$CCCH_2$) (Figure 3b, blue trace). Because La(HCCCH) is predicted to have a lower IE (43772 cm^{-1}) than La(η^2-$CCCH_2$) (44579 cm^{-1}) (Table 4.1), the 0-0 transition of La(HCCCH) ($^1A \leftarrow {}^2A$) is aligned with the strongest band of the experimental spectrum at 42953 cm^{-1}, whereas that of La(η^2-$CCCH_2$) ($^1A' \leftarrow {}^2A'$) is aligned with the strong band at 43609 cm^{-1}. The predicted IE difference of 807 cm^{-1} between the two isomers is in very good agreement with the measured value of 656 cm^{-1}. Although neither of the simulations reproduces all observed major bands, their combination matches the experimental spectrum nicely. The third isomer is at a much higher energy and its simulation does not match either portion of the experimental spectrum. For La(HCCCH), the IE of the complex is predicted to be 43772 cm^{-1} and measured to be 42953 cm^{-1}. The frequencies of a symmetric La-ligand stretching mode are calculated to be 448 and 408 cm^{-1} and measured as 425 and 408 cm^{-1} in the ionic and neutral states, respectively. The theoretical and experimental IEs, and metal-ligand stretching frequencies are in very reasonable agreement. Similarly, the calculated and measured IEs and stretching frequencies of La(η^2-$CCCH_2$) are comparable to each other, as shown in Table 4.2. It is noted that the origin band of La(HCCCH) is observed to be stronger than that of La(η^2-$CCCH_2$) even though the former is predicted to be slightly less stable (by 0.09 eV) than the latter. This is because the intensity of the 0-0 band is not only dependent on the number of the particles in the initial state but also the FC factors. Because of a larger geometry change (i.e., the La-C_1 distance) upon ionization, the intensity ratios of the 0-0 band to other transitions in La(η^2-$CCCH_2$) are expected to be smaller than those in La(HCCCH). This expectation is consistent with the observation where the intensity ratio of the 0-0 band to the first-quantum La-ligand stretching excitation of La(η^2-$CCCH_2$) is about one half of La($HCCCH_2$). Moreover, Table 4.2 shows interesting effects of deuteration on the IEs and La-ligand stretching frequencies of the two isomers. First, the deuteration does not affect the IEs because of the similar changes on the vibrational zero point energies of the neutral and ionic states upon the deuterium substitution. Second, although it does not affect the La-ligand stretching frequencies of La(η^2-$CCCH_2$), the deuteration significantly reduces the metal-ligand stretching frequencies of La(HCCCH). This differential effect can be rationalized by considering the structures of the two isomers. In La(η^2-$CCCH_2$), the La atom is bound with the two carbon atoms that have no hydrogen atoms being attached, and thus the metal-ligand stretching involves no hydrogen movements. On the other hand, in La(HCCCH), the La atom is bound with two terminal carbon atoms, each with a hydrogen being attached, and the La-(HCCCH) stretching engages the motions of both carbon and hydrogen atoms. A literature search discovered that reactions between terminal acetylenes and fluoroalkoxide molybdenum in solution yield similar deprotiomolybdenacyclobutadiene complexes of the type of $Mo(C_3R_2)(OR')_2$ ($R = C(CH_3)_3$ or C_6H_5, $R' = CH(CF_3)_2$ or $C(CH_3)_2CF_3$).[152]

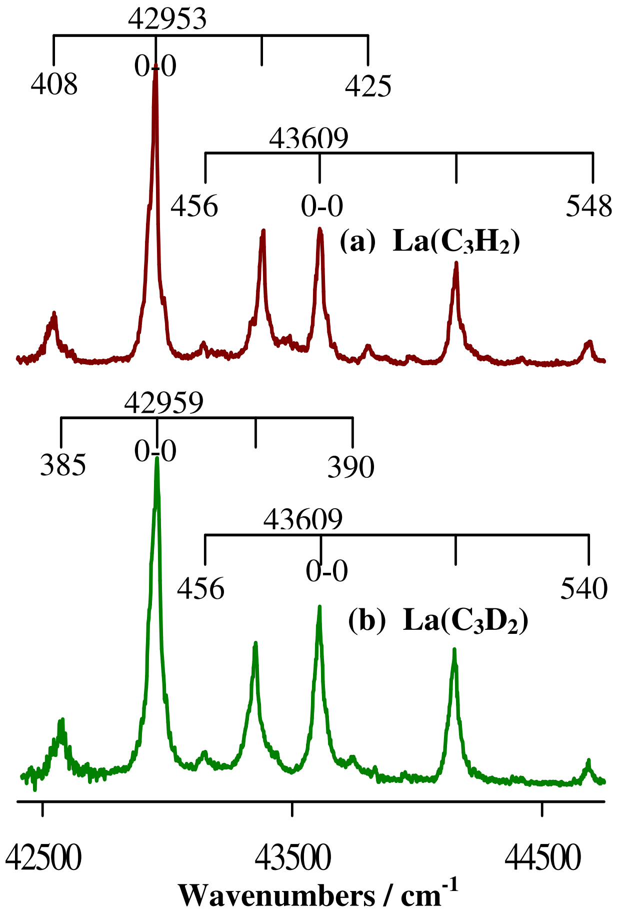

Figure 4.3 MATI spectra of LaC_3H_2 (a) and LaC_3D_2 (b) formed by reactions of La with $CH_3C≡CH$ or $CD_3C≡CD$. $CH_3C≡CH$ or $CD_3C≡CD$ were seeded in 40 psi He gas with concentration of 10^{-4} - 10^{-5}.

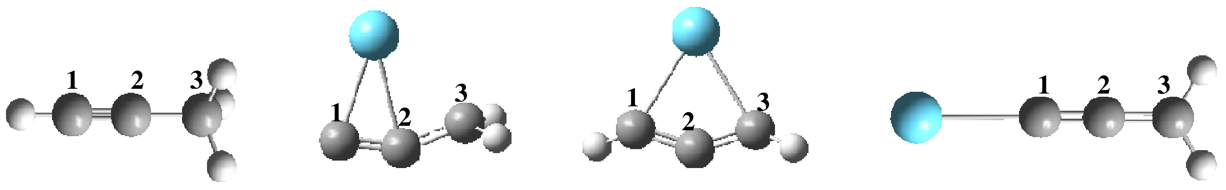

C_{3V} ($^1A_1$) C_s ($^2A'$) C_2 (^2A) C_{2V} ($^2A_1$)

(a) $CH_3C≡CH$ **(b) La(η^2-$CCCH_2$)** **(c) La(HCCCH)** **(d) La-$CCCH_2$**

Figure 4.4 Structures of $CH_3C≡CH$ (a), La(η^2-$CCCH_2$) (b), La(HCCCH) (c) , and La-$CCCH_2$ (d).

Table 4.1 Point groups (**PG**), electronic states (**ES**), relative energies including the vibrational zero-point corrections (**E_0**, cm^{-1}), bond lengths (Å) and bond angles (degrees) of $CH_3C\equiv CH$, La(η^2-$CCCH_2$), La(HCCCH) and La-$CCCH_2$ calculated at the DFT/ B3LYP level. The labels of the carbon atoms are the same as those in Figure 4.4

	$CH_3C\equiv CH$	La(η^2-$CCCH_2$)		La(HCCCH)		La-$CCCH_2$	
PG	C_{3v}	C_s	C_s	C_2	C_2	C_{2v}	C_{2v}
ES	$^1A_1$	$^2A'$	$^1A'$	^2A	^1A	$^2A_1$	$^1A_1$
E_0		0	44579	712	44484	5399	49313
C_1-C_2	1.20	1.26	1.27	1.32	1.31	1.29	1.30
C_2-C_3	1.46	1.40	1.39	1.32	1.31	1.33	1.31
La-C_1		2.31	2.20	2.40	2.35	2.13	2.07
La-C_2		2.43	2.39	2.45	2.41		
La-C_3		2.62	2.62	2.40	2.35		
$\angle C_3$-C_2-C_3	180	151	149	145	142		
$\angle C_3$-C_2-C_1-H	180	110	110	136	136	180	180

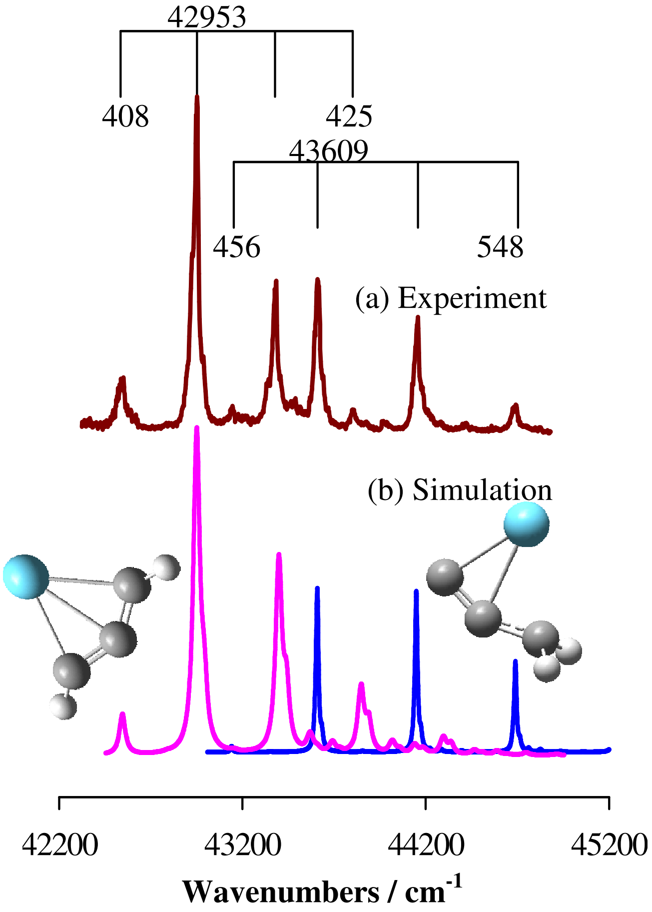

Figure 4.5 Experimental MATI spectrum (a) and the simulated spectra of the $^1A \leftarrow {}^2A$ transition of La(HCCCH) (b, pink trace) and the $^1A' \leftarrow {}^2A'$ transition of La(η^2-CCCH$_2$) (b, blue trace) at 350 K.

Table 4.2 Adiabatic ionization energies (AIE, cm^{-1}) and vibrational frequencies (cm^{-1}) of La(HCCCH) / La(DCCCD) and La(η^2-$CCCH_2$) / La(η^2-$CCCD_2$) from MATI measurements and DFT / B3LYP calculations. The uncertainty of the experimental IE values is 5 cm^{-1}

Isomers	MATI	B3LYP
La(HCCCH) / La(DCCCD), C_2		
AIE : $^1A_1 \leftarrow {}^2A_1$	42953 / 42959	43772 / 43732
La-hydrocarbon symmetric stretching	425 / 390	448 / 407
La^+-hydrocarbon symmetric stretching	408 / 385	408 /380
La(η^2-$CCCH_2$) / La(η^2-$CCCD_2$), C_s		
AIE ($^1A' \leftarrow {}^2A'$)	43609 / 43609	44579 / 44568
La-hydrocarbon symmetric stretching	548 / 540	540 / 540
La^+-hydrocarbon symmetric stretching	456 / 456	469 / 468

Table 4.3 MATI band positions (cm^{-1}) and assignments of La(HCCCH) and La(η^2-$CCCH_2$). The uncertainty associated with the band positions is 5 cm^{-1}

La(HCCCH)		La(η^2-$CCCH_2$)	
Band position of MATI	Assignment	Band position of MATI	Assignment
42545	6^0_1	43153	7^0_1
42953	0^0_0	43609	0^0_0
43378	6^1_0	44157	7^1_0
43803	6^2_0	44705	7^2_0

4.3.2 Reaction Pathways for the Formation of La(HCCCH) and La(η^2-CCCH$_2$)

La + $CH_3C\equiv CH$ → $LaC_3H_2 + H_2$

LaC_3H_2 is the La-bound dehydrogenated product of propyne as shown above. We have confirmed that the bond activation of propyne is La metal mediated, rather than the vaporization laser assisted by conducting a control experiment. The details of the control experiment can be found under the experimental details (section 4.2). The reaction products formed in the original and control experiments were identical, though a higher propyne concentration in the latter experiment was required to produce a comparable ion intensity in the mass spectra. Because propyne bypassed the vaporization region in the control experiment, vaporization laser played no role for the hydrocarbon activation. This observation should not be surprising because the laser flux used in metal vaporization is rather low and propyne has low absorption cross sections for visible light.

The reaction pathway of LaC_3H_2 formation and the structural details of the stationary points are presented in Figure 4.6 and 4.7 respectively. The formation of LaC_3H_2 involves three major steps (Figure 4.6). The initial step is the formation of a La-propyne association complex through La addition to the C≡C triple bond (i.e., La + $CH_3C\equiv CH \rightarrow$ IM1 in Figure 4.6). Upon the association complex formation, the C≡C triple bond of propyne is elongated (by 0.14 Å) and becomes a double bond (with the C-C bond length of 1.35 Å) due to the cleavage of one of the π bonds between the two carbon atoms. Molecular orbital analysis reveals that the unpaired pπ electron on each of the two carbon atoms is shared with a La 5d electron to form a La-C σ bond. The association complex is the most stable species along the reaction pathway. The next step is the activation of a methyl C(sp^3)-H bond (i.e., IM1→TS1 → IM2 → Undefined TS2 → IM3 → TS3 →IM4). The activation via TS1 involves a methyl group rotation (by 60^o) to bring a hydrogen atom to the vicinity of the La atom. The local minimum IM2 has a 16% stretched methyl C-H bond compared to IM1. The H atom in the elongated C-H bond migrates towards to La to form a La-H bond on the CCC plane in IM3. Locating a transition state between IM2 and IM3 has not been successful because the potential energy surface is flat after IM2. Thus, an "undefined TS2" between the two local minima is labeled in Figure 4.6. The H atom in the La-H bond continues to rotate out of the CCC plane in TS3 and rests in a plane with a dihedral angle of 84^o to the CCC plane in IM4. The third step is the H_2 elimination through the activation of the C(sp)-H bond or a second C(sp^3)-H bond in the methyl group (IM4 $\rightarrow$TS5 $\rightarrow$IM6 $\rightarrow$ TS6 $\rightarrow$ La(η^2-CCCH$_2$) + H_2 or IM4 $\rightarrow$TS4 $\rightarrow$IM5 $\rightarrow$ La(HCCCH) + H_2). The C(sp)-H bond breakage leads to the formation of La(η^2-CCCH$_2$), whereas the second C(sp^3)-H bond cleavage results in the formation of La(HCCCH). In either case, LaC_3H_2 is formed by a concerted H_2 elimination process. In this process, the H atom from the C(sp)-H bond or the second C(sp^3)-H bond is migrated to the H atom in La-H to form a (C_3H_2)La···(H-H) structure prior to the H_2 elimination. For the formation of La(η^2-CCCH$_2$), the H atom in the La-H bond continues the rotation towards the α H atom to form IM6 (via TS5). The activation of the α H atom in IM6 costs 110 kJ mol^{-1} to form the transition state TS6. Elimination of a H_2 molecule from TS6 leads to the product of La(η^2-CCCH$_2$). For the formation of La(HCCCH), the activation of the second C(sp^3-H) bond is through the transition state TS4 to form the local minimum IM5 before the H_2 elimination. The activation barrier of the C(sp^3-H) bond from IM4 to TS4 (152 kJ mol^{-1}) is about 40 kJ mol^{-1} higher than that of the C(sp)-H bond. The concert H_2 elimination predicted for the La + propyne reaction is consistent with previous studies on the propyne and other small unsaturated hydrocarbon activations by other transition metal atoms.[21,153-155] The energy barriers for the formation of La(η^2-CCCH$_2$) and La(HCCCH) via the

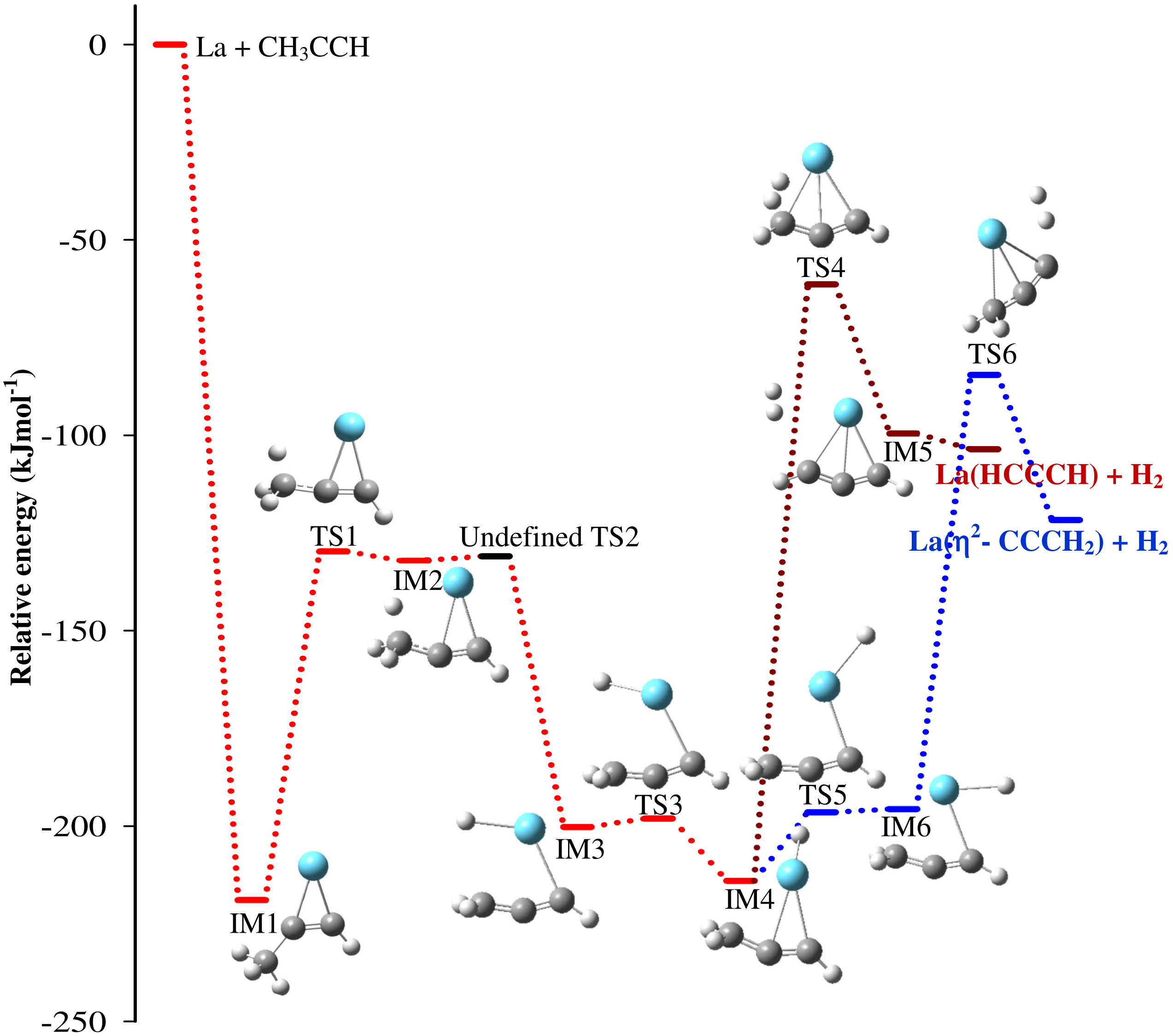

Figure 4.6. Reaction pathways for the formation of La(HCCCH) and La(η^2-CCCH$_2$) from the reaction between La and CH$_3$C≡CH at the DFT/B3LYP level. TS: transition states, IM: intermediates.

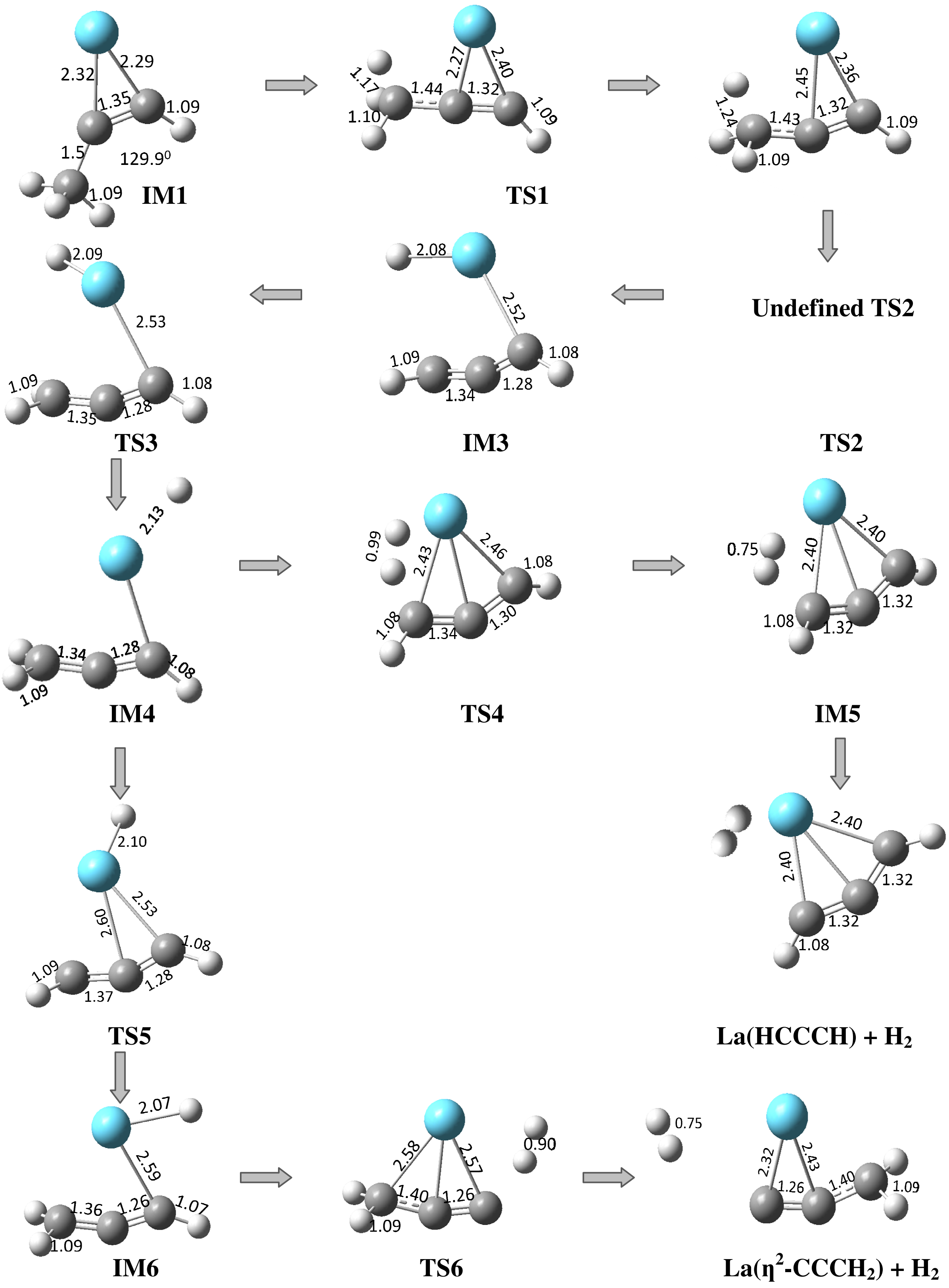

Figure 4.7 Stationary points of the reaction pathway for the formation of La(HCCCH) and La(η^2-CCCH$_2$) from the reaction between La and CH$_3$C≡CH.

concerted H_2 elimination are below the energy of the reactants. According to the calculation, the required energy for further H elimination is nearly 165 $kJmol^{-1}$ at CCSD(T) / SDD, aug-cc-pvtz level of theory and therefore it will not occur.

4.4 Conclusion

In conclusion, this study demonstrates that the C-H activation of propyne by La atom leads to the formation of the dehydrogenated product of LaC_3H_2 and MATI spectroscopy combined with theoretical calculations shows the existence of the La(η^2-$CCCH_2$) and La(HCCCH) isomers of the organometallic radical. The isomers are formed by concerted 1,3- or 3,3-hydrogen elimination processes and have a doublet ground electronic state with an unpaired electron located on the metal center. Moreover, although La is in the formal oxidation state of +2, the ionization energies of these isomers are significantly lower than that of the free atom. This observation suggests that the concept of the formal oxidation state widely used in chemistry textbooks is not useful in predicting the change of the ionization energy of a metal atom upon ligation. To extend this work, the investigation of the C-C bond coupling product (LaC_6H_6) of propyne is in progress.

CHAPTER 5. C-C BOND ACTIVATION AND COUPLING OF PROPENE INDUCED BY LANTHANUM ATOM

5.1 Indtroduction

Over the past few decades, considerable attention has been drawn to the study of reactions between ground state transition metal atoms, especially Y, Zr, and Nb, and small olefinic hydrocarbons.[5,25,41-44,46,156-164] This is because such studies can lead to better understand and improve the catalytic activity of transition metal compounds such as Ziegler-Natta.[22,24,160,165-168] Particularly, gas-phase measurements provide an efficient mean to investigate reactivity patterns, reaction mechanisms, bonding and structures and structure-reactivity relationships of crucial intermediates even though they do not account for the precise thermodynamics and kinetics operating in applied catalysis. Moreover, since the gas phase systems are free from effects of solvents and counter ions, they can be more conveniently treated with quantum chemical calculations. The quantitative comparison of the theoretical calculations and experimental measurements provide new insights into elementary reaction mechanisms.

The present work aims to investigate the structures and electronic states of $LaCH_2$ and LaC_4H_6 (or LaC_4D_6) formed by the reaction of La with propene (C_3H_6, $CH_3CH=CH_2$); or C_3D_6 and the reaction pathways for the formation of the La-complexes. Although reactions between transition metal atoms and propene were investigated previously, there has been no sufficient report on the spectroscopic characterization of the reaction products.[21,28,164] Weisshaar *et al.* have measured the bimolecular rate constants and kinetic isotope effects for the primary reactions of Y atom ($4d^15S^2$) with C_3H_6 and C_3D_6 in a fast flow reactor.[46] They have investigated the branching ratios of the primary products and observed a significant change in the branching ratios with the deuterium substitution.[46] Davis et al. have investigated the competition between the C-C and C-H bond activation of propene by Y ($4d^15S^2$) atom using cross molecular beam (CMB) experiment in combination with Rice-Ramsperger-Kassel-Marcus (RRKM) theory, and proposed the schematic potential energy diagrams for the product formation. Guang et al. have investigated the reaction pathways for the product formation for the same system (Y + propene) using the B3LYP calculations.[21] Parnis et at. have determined the structure of a C-H bond insertion intermediate formed by the reaction between V atom ($4d^15S^2$) and C_3H_6 in Ar under matrix-isolation condition using Fourier-transform infrared (FTIR) spectroscopy.[164] Schwarz et al. have investigated the reactions of Ce^+ with propene using Fourier-transform ion-cyclotron resonance (FT-ICR) mass spectrometry.[11] For Ce^+ + propene, they observed products from both primary and secondary reactions.[11] They also proposed possible structures for the secondary products on the basis of collision induce dissociation (CID) patterns.[11] Freiser et al. have observed $LaCH_2^+$ from a reaction between La^+ and propene in a Fourier transform mass spectrometer (FTMS). Their photodissociation study has revealed that $LaCH_2^+$ exist as a metal carbene, even though they haven't proposed a geometry for $LaCH_2^+$.[169] Our group has investigated the structures, electronic states and formation of LaC_3H_4 and LaC_3H_6 from La + propene reaction by MATI / ZEKE spectroscopic measurements combined with DFT calculations in a previous work.[134] The current work aims to investigate the rest of the masses observed in La + propene reaction. La atom mediated C-C bond activation and coupling reaction of propene and its deuterated analogue will be discussed in this chapter. Detailed characterization of both primary and secondary products from a M + propene (M = metal or metal cation) reaction has not been reported before and our work provides the first detailed story on them.

5.2 Experimetal and Computational Details

The metal-cluster beam instrument used in this work consists of the reaction and spectroscopy vacuum chambers and is described in Chapter 2. The metal-hydrocarbon reaction was carried out in a laser vaporization metal cluster beam source. $CH_3CH=CH_2$ (> 99%, Sigma-Aldrich) was seeded in a He carrier gas with a concentration of 10^{-4} - 10^{-5} in a stainless steel mixing cylinder. La metal atoms were generated by pulsed-laser (Nd:YAG, Continuum Minilite II, 532 nm, 1.0-1.5 mJ/pulse) vaporization of a La rod (99.9%, Alfa Aesar) in the presence of the propene / He mixture (40 psi) delivered by a home-made piezoelectric pulsed valve. The metal atoms and gas mixture entered into a clustering tube (2 mm diameter and 2 cm length) where the chemical reactions occurred. The reaction mixture was then expanded into the reaction chamber, collimated by a cone-shaped skimmer (2 mm inner diameter), and passed through a pair of deflection plates. Ionic species in the molecular beam that were formed during laser vaporization were removed by the electric field (100 Vcm^{-1}) applied on the deflection plates. The neutral products were identified by photoionization time-of-flight mass spectrometry.

Prior to the MATI measurements, photoionization efficiency spectra were recorded to locate the approximate ionization thresholds of the La-hydrocarbon complexes to simplify the MATI experiment. In the MATI experiment, the metal complexes were excited to high-lying Rydberg states in a single-photon process and ionized by a delayed pulsed electric field. The excitation laser was the same as that for photoionization in the mass spectrometry and photoionization efficiency experiments and was the frequency doubled output of a tunable dye laser (Lumonics HD-500), pumped by the third harmonic output (355 nm) of a Nd:YAG laser (Continuum Surelite II). The laser beam was collinear and counter propagating with the molecular beam. The ionization pulsed field (320 V cm^{-1}) was generated by two high voltage pulse generators (DEI, PVX-4140) and delayed by 10-20 μs from the laser pulse by a delayed pulsed generator (SRS, DG641). A small DC field (6.0 V cm^{-1}) was applied to separate the prompt ions produced by direct photoionization from the MATI ions generated by delayed field ionization. The MATI ion signal was obtained by scanning the wavelength of the tunable dye laser, detected by a dual microchannel plate detector, amplified by a preamplifier (SRS, SR445), averaged by a gated integrator (SRS, SR280), visualized by a digital oscilloscope (Tektronix TDS 3012), and stored in a laboratory computer. Laser wavelengths were calibrated against vanadium atomic transitions in the spectral region.[129] The Stark shift induced by the DC separation field was calculated using the relation of $\Delta IE = 6.1E_f^{1/2}$, where E_f is in V cm^{-1} and ΔE is in cm^{-1}.[130]

Geometry optimization and vibrational frequency calculations were carried out using Gaussian 03 software package.[92] In these calculations we used the Becke's three-parameter hybrid functional with the correlation functional of Lee, Yang, and Parr (B3LYP)[82,83] and 6-311+G(d,p)[93,94] basis set for C and H and effective-core-potential SDD[95] basis set for La. We have extensively used DFT/B3LYP and found this method generally produce adequate results for the spectral and structural assignments of organometallic complexes.[131] No symmetry restrictions were imposed in the initial geometry optimization, but symmetry was imposed in the subsequent optimizations to identify the accurate electronic states. For each optimized stationary point, vibrational analysis was performed to identify the nature of the stationary point (minimum or saddle point). In predicting reaction pathways, minima connected by a transition state were confirmed by intrinsic reaction coordinate calculations.

To compare with the experimental MATI spectra, multi-dimensional FC factors were calculated from the equilibrium geometries, harmonic vibrational frequencies, and normal coordinates of the neutral and ionized complexes.[132] In these calculations, the recursion relations from Doktorov et al.[133] were employed, and the Duschinsky effect[99] was considered to account for a possible axis rotation from the neutral complex to the cation. Spectral simulations were obtained using the experimental linewidth and a Lorentzian line shape.

5.3 Results and Discussion

Figure 5.1 displays the TOF mass spectrum of the products formed by the reaction between laser vaporized La atom and $CH_3CH=CH_2$ at the laser ionization wavelength of 232 nm. The metal complexes shown in the mass spectrum are LaC, LaCH, $LaCH_2$, LaC_2, LaC_3H_3, LaC_3H_4, LaC_3H_6, LaC_4H_6, LaC_4H_{10}, LaC_6H_{10}, and LaC_6H_{12}. Because of the IEs of LaC, LaCH, and LaC_2 are predicted by the B3LYP/SDD/6-311+G(d,p) calculations to be much higher than 232 nm (44843 cm^{-1}), the observation of these species in the mass spectrum is likely due to a two-photon ionization of these neutral complexes or a two-photon dissociative ionization of larger complexes. Experimentally, we observed that the ion intensities of LaC, LaCH, and LaC_2 depended more strongly on the laser photon density than those of other species in the mass spectrum. When the laser beam was defocused, the ion intensities of these species were reduced considerably compared to the intensities of other complexes. For LaC_3H_3, although its IE is expected to be lower than 223 nm, we also observed a stronger effect of the laser photon density on its ion intensity than on the intensities of larger species. We recorded its PIE spectrum, but was not able to locate a reasonable IE for the complex because the PIE spectrum shows a very slow ion onset. This observation could be due to a large structural difference between the neutral and cation or a dissociative ionization process of a higher mass. Among other observed products, Sudesh Kumari who was a coworker in our group has measured MATI spectra of LaC_3H_4 and LaC_3H_6 and investigated their structures and formation.[134] Thus, these two species will not be discussed in this Chapter. Instead, I will focus on the structures, electronic states, and formation on $LaCH_2$ and LaC_4H_6. For LaC_6H_{10} and LaC_6H_{12}, we were not able to obtain sharp PIE spectra, likely due to the large structural difference between the neutral and cation species.

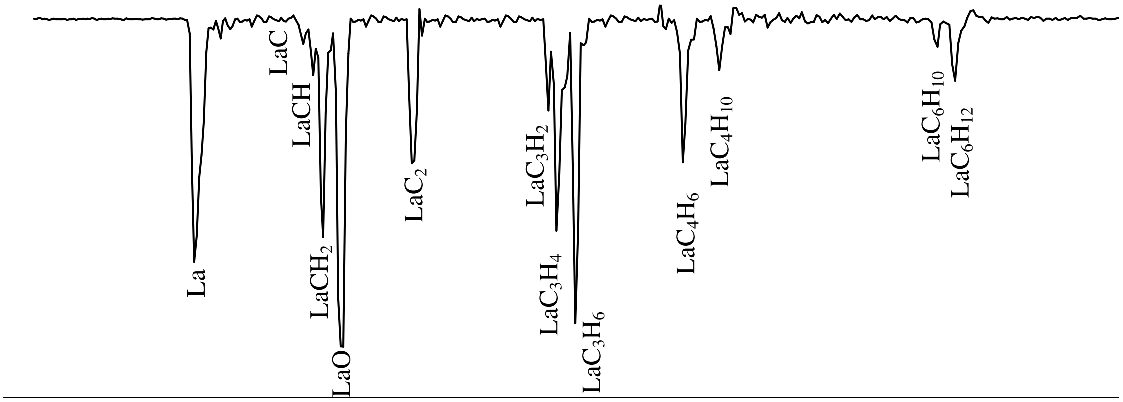

Figure 5.1 TOF-MS spectrum of the La + C_3H_6 reaction recorded at the laser ionization wavelength of 232 nm. The seeding concentration of C_3H_6 in He is 10^{-5}.

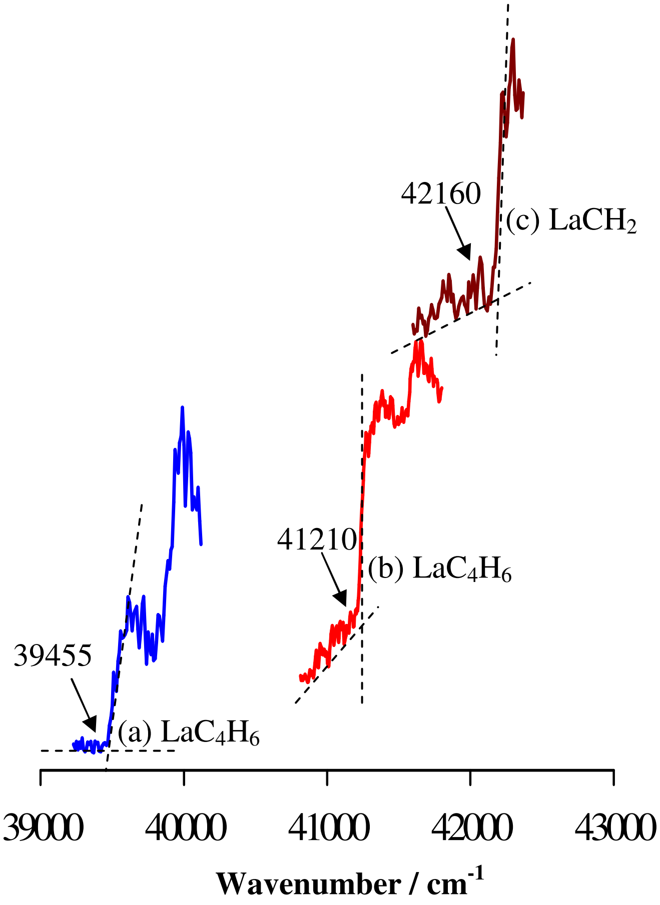

Figure 5.2 PIE spectra of LaC_4H_6 ((a) & (b)) and $LaCH_2$ (c).

5.3.1 $LaCH_2$

The PIE spectrum of $LaCH_2$ is presented in Figure 5.2(c). There is a slowly rising signal onset followed by a very sharp one in the spectrum. The slowly rising signal originates from the ionization of thermally excited vibrational levels of the neutral complex. The sharp signal onset at 42160 (100) cm^{-1} corresponds to the first ionization threshold of the complex. The ionization threshold from the PIE measurements is used to simplify the search for the MATI signal. Figure 5.6 displays the MATI spectrum of $LaCH_2$ which has an origin band at 42263 (5) cm^{-1}, a 677 cm^{-1} progression, 446 and 1123 cm^{-1} independent intervals. Because of the short progression of the MATI spectrum, we expect a small structural change of the complex upon the ionization.

The theoretical calculations were carried out to help the spectral and structural assignments. A pyramid-like structure was used as an initial guess in the geometry optimization, but was converged to a planar C_s structure which is a metal carbene. Because the planar structure was close to C_{2v} symmetry, we also performed geometry optimization under symmetry constraints to optimize the complex in C_{2v} symmetry. However, the optimized C_{2v} structure displays an imaginary frequency associated with a H rocking motion. Therefore the C_{2v} structure is not a minimum, but a transition state. Figure 5.3 shows the potential energy change of $LaCH_2$ as a function of the La-C-H_1 bond angle. As shown by the figure, the potential energy first increases as the angle increases from 90 to 125^o and then decreases as the angle increases from 125 to 158^o. However, this one-dimensional energy scan does not account for the effect of the La-C bond length. For example, we found that the elongation of a La-C bond (by 14%) in the C_{2v} symmetry leads to an energy minimum. This minimum is 98 $kJmol^{-1}$ (8192 cm^{-1}) higher in energy than the initially found minimum (C_s symmetry). To better understand how the potential energy change with respect to both La-C-H_1 bond angle and La-C bond length, a two-dimensional (2D) energy scan was carried out, and the result is shown in Figure 5.4. This 2D scan shows that the different combinations of La-C-H_1 bond angle and La-C bond length lead to many energy minima. However, the energy minimum found in the initial geometry optimization is the global minimum (C_s symmetry) which is shown in Figure 5.5. Table 5.1 summarizes the relative energies and geometries of $LaCH_2$ and its singly charged cation at different electronic states.

$LaCH_2$ is expected to be in the doublet spin state if the La maintains a double bond with the C. Either doublet or quartet spin state can be expected if only a single bond exist between them. Therefore, we consider the doublet and quartet spin states for the neutral complex and singlet and triplet states for the cation in our calculations. The ground electronic state of $LaCH_2$ is predicted to be $^2A'$, with La doubly bound to the C atom. The quartet state ($^4A_2$) is predicted to be an excited state at 8437 cm^{-1} above the doublet ground state. In this state, the complex is converged to C_{2v} symmetry, and the La-C bond (2.44 Å) is much longer than that in the $^2A'$ state (2.09 Å). The significant elongation of La-C bond in the $^4A_2$ state suggests that La is singly, rather than doubly, coordinated with the carbon atom as expected. Because it is at rather high energy and our experiment is conducted in supersonic molecular beam, the $^4A_2$ state is unlikely the carrier of the observed MATI spectrum. Therefore, in our spectral analysis, we considers only the $^1A' \leftarrow {}^2A'$ transition. As shown in Figure 5.6 and Table 5.4, the $^1A' \leftarrow {}^2A'$ simulation matches very nicely with the experimental spectrum. Predicted IE is 43141 cm^{-1}, which agrees reasonably with the observed IE of 42263 cm^{-1}. Therefore, our work prove that the C_{2v} structure proposed for $LaCH_2^+$ by Goddard III et al. in their ab initio calculations, involving multireference configuration interactions is inaccurate.[170] The vibrational intervals of 677 cm^{-1}

and 446 cm^{-1} are related to the La-C stretching (υ_4^+) and H rocking (υ_5^+) motions of $LaCH_2^+$. The small peak at 1123 cm^{-1} is a combinational band of υ_4^+ and υ_5^+. Theoretically predicted frequencies are within 20 cm^{-1} of the measured values. The band assignments of the MATI spectrum are listed in Table 5.5.

5.3.1.1 Agostic Interactions and Activity of $LaCH_2$

If we look carefully the structural details of $LaCH_2$ in Table 5.1, we can note at least three major structural features of the complex. First, a double bond exists between La and C. Second, the C-H_1 bond is slightly longer than the C-H_2 bond. Third, the La-C-H_1 bond angle is around 90^0. These features indicate that the so-called agostic interactions exists between the C-H_1 $\boldsymbol{\sigma}$ bond and La metal atom. Agostic interaction which was first discovered by Brookhart and Green,[171] currently is an established bonding type in organometallic chemistry and catalysis. Agostic is an intra-molecular 3 center 2 electron bond which involve the interaction of coordinatively-unsaturated transition metal with a single C-H bond. The bonding electrons of the C-H σ orbital are donated to the metal center forming three-center two-electron bond. If the metal center is electron rich, a back donation can also occur from the metal center to the antibonding $\boldsymbol{\sigma}$* orbital of the C-H bond. If the back donation is strong, the C-H bond may be broken because of electron occupation in the σ* orbital.[171,172] However, since the La metal center in $LaCH_2$ is not very electron rich, the back donation from the metal center to the C-H σ* orbital is expected to be weak. The interaction between the C-H_1 σ bond and La atom can be seen in the molecular orbitals presented in Figure 5.7. Similar agostic interactions in metal-carbene complexes have been considerably studied experimentally and theoretically because of their significance in organometallic chemistry.[23,52,162,166,173-187] Agostic bonds can increase the rigidity of the transition state in a reaction. This increased rigidity influences the stereoselectivity of a reaction. Particularly, we have observed α agostic interactions in $LaCH_2$. The existence of α agostic interactions in olefin polymerization reactions dramatically lower the activation barrier in the olefin insertion step and lead to stereospecific polymerization.[23,52,166,175-177]

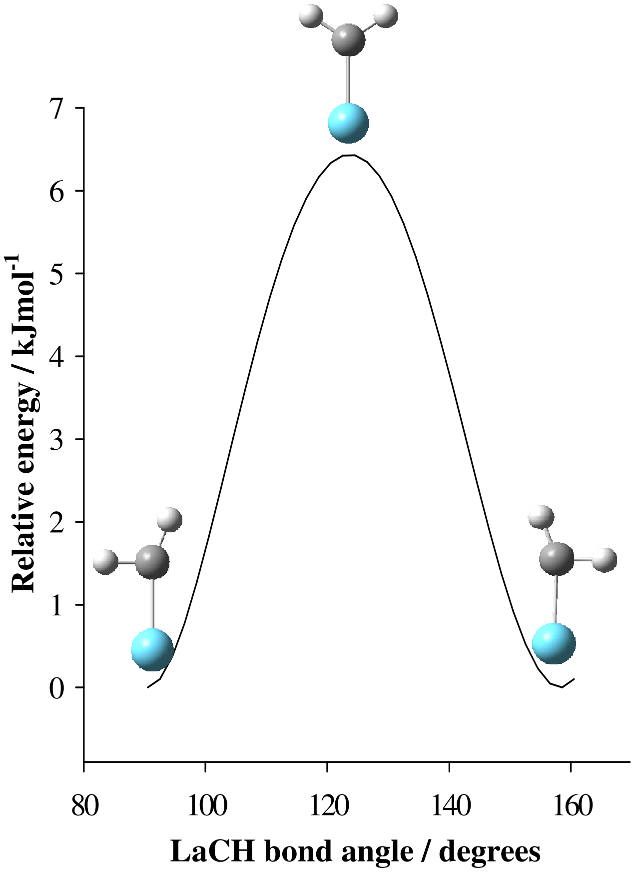

Figure 5.3 Potential energy (kJ mol^{-1}) scan of $LaCH_2$ as a function of the La-C-H_1 bond angle(degrees) calculated at the DFT/ B3LYP level.

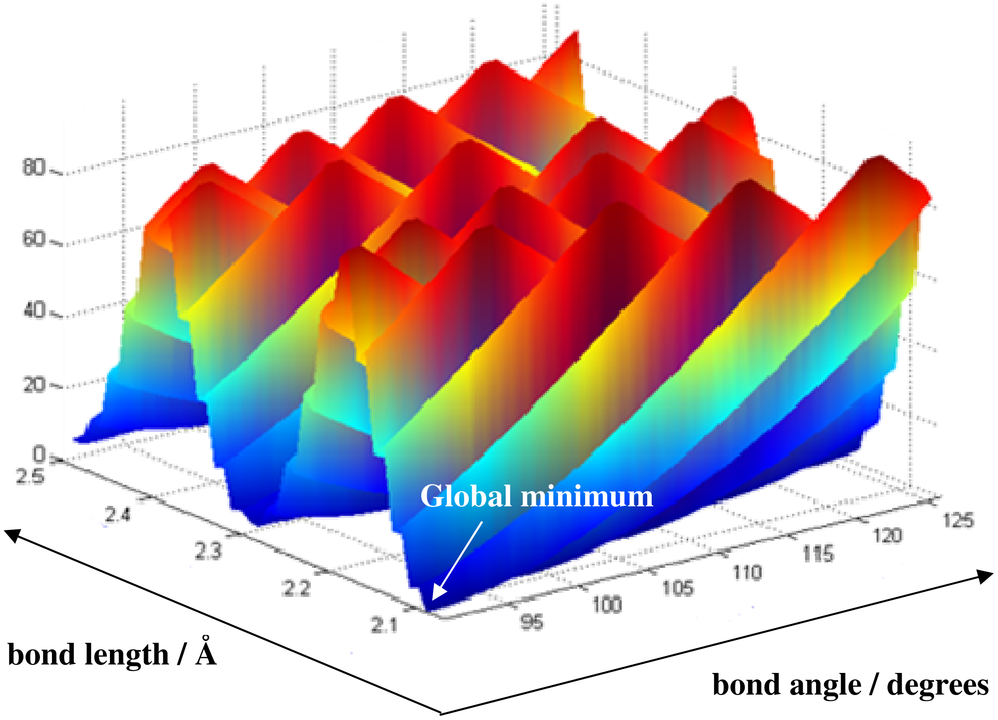

Figure 5.4 Potential energy (kJ mol^{-1}) scan of $LaCH_2$ as a function of the La-C-H_1 bond angle (degree) and La-C bond length (Å) calculated at the DFT/ B3LYP level.

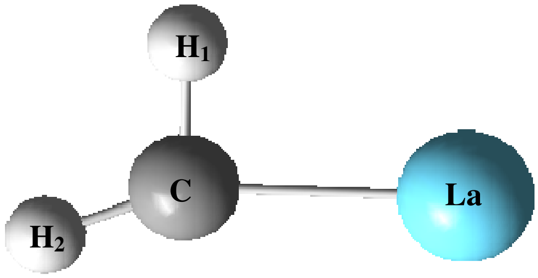

Figure 5.5 The global minimum structure of $LaCH_2$.

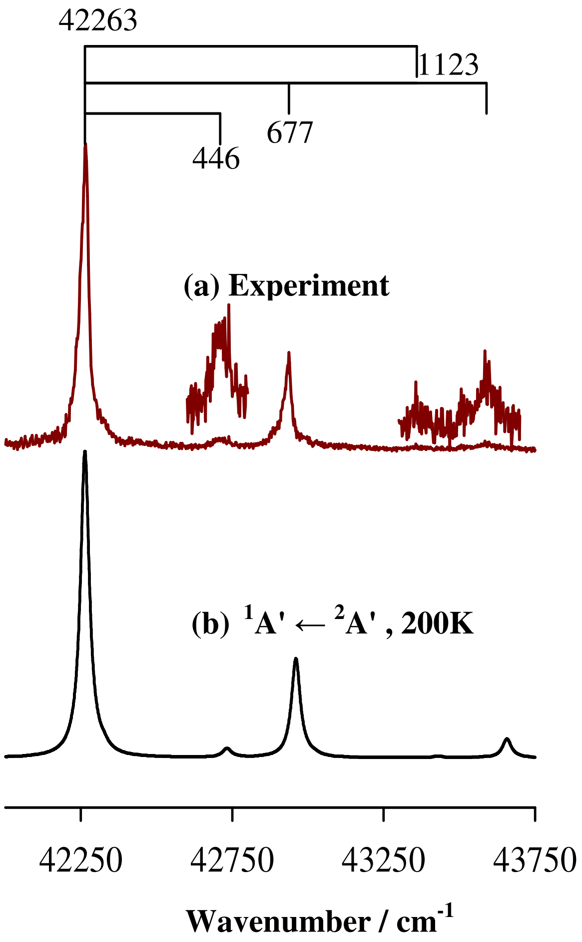

Figure 5.6 MATI spectrum of $LaCH_2$ (a) and the simulated spectrum of the $^1A' \leftarrow ^2A'$ transition of $LaCH_2$ at 200K with FWHM of 35 cm^{-1} (b).

Table 5.1 Point groups (PG), relative energies ($E_{0,}$ cm^{-1}), bond lengths (Å) and bond angles (degrees) of $LaCH_2$ calculated at the DFT/ B3LYP level. Atomic labels are the same as those in Figure 5.5

	$^2A'$	**$^1A'$**	**$^3B_1$**	**$^4A_2$**
PG	Cs	Cs	C_{2v}	C_{2v}
E_0	0	43830	52253	8437
La-C	2.09	2.04	2.31	2.44
C-H_1	1.12	1.12	1.10	1.10
C-H_2	1.09	1.09	1.10	1.10
< La-C-H_1	91	92	125	126
< La-C-H_2	158	155	125	126
< H_1-C-H_2	111	112	109	107

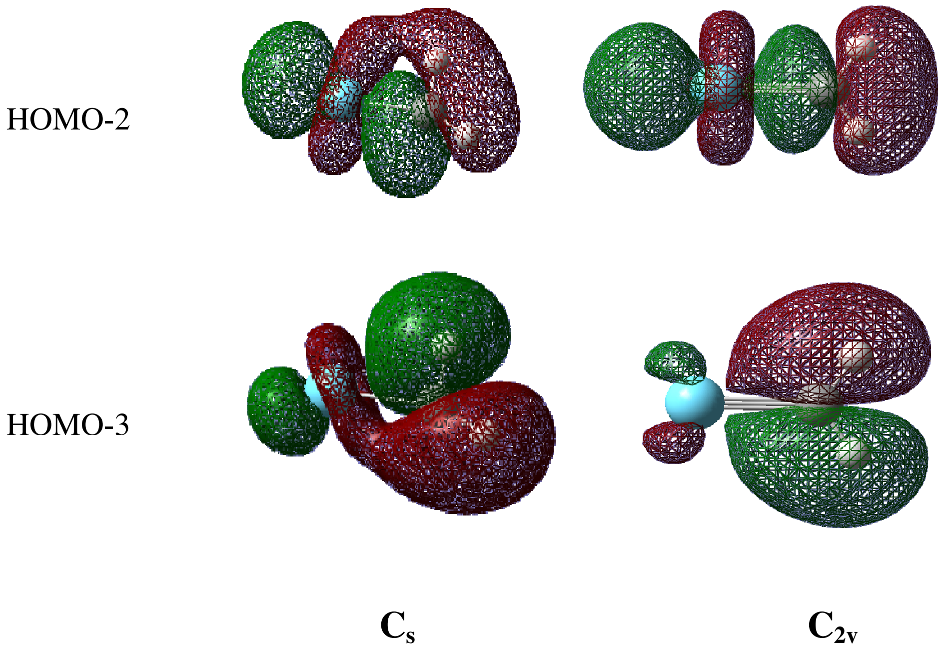

Figure 5.7 Molecular orbitals stabilized by the agostic interactions in C_s symmetry compared to C_{2v} symmetry.

5.3.2 LaC_4H_6

As shown in Figures 5.2(a) and 5.2(b), two PIE curves with ion signal onsets separated by nearly 1750 cm^{-1} are observed for LaC_4H_6. The PIE spectra in Figure 5.2(a) and Figure 5.2 (b) display their first sharp onsets at 39455 (50) and 41210 (50) cm^{-1} respectively. The two PIE spectra could arise from two electronic transitions of the same structural isomer or from transitions of two different isomers. Figure 5.9(a) displays the experimental MATI spectrum of LaC_4H_6 in the region of 39000-40500 cm^{-1}. This MATI spectrum is related to the PIE curve in Figure 5.2(a). The strongest band at 39420 (5) cm^{-1} is the origin band of an electronic transition. To the right side of the origin band are a 398 cm^{-1} progression and 320 and 470 cm^{-1} bands. Superimposed on the 398 cm^{-1} progression is a 26 cm^{-1} sequence band. To the left side of the origin bands are 285 and 370 cm^{-1} intervals. Other bands that are not labeled in the figure are combination bands arising from excitations of two or more modes. Figure 5.10 (a) exhibits a MATI spectrum of LaC_4H_6 in the region of 40800-42500 cm^{-1}. The strongest band in this MATI spectrum is observed at 41260 (5) cm^{-1}. This band corresponds to the sharp onset in the PIE spectrum in Figure 5.2(b) and may be considered to be a second origin band for the complex. The MATI spectrum in this region is simpler than that in the lower energy region and consists of a 346 cm^{-1} progression on the right side of the origin band, and a 356 cm^{-1} band on the left. This spectrum has been analyzed by Sudesh Kumari, a former colleague in our group, and the spectral analysis can be found in her dissertation.[134] I will discuss below the spectrum in the region of 39000-40500 cm^{-1} and structure of LaC_4H_6 responsible for the observed spectrum.

Numerous possible isomers of LaC_4H_6 have been considered, and four of which are presented in Figure 5.8 and Table 5.2. Isomer A (lanthanum trimethylenemethane) is predicted to be the lowest energy isomer even though the formation of this isomer requires significant changes in the parent hydrocarbon. It has C_{3v} symmetry with a $^2A_1$ ground state. The $^1A_1 \leftarrow ^2A_1$ electronic transition of this isomer is responsible for the MATI spectrum shown in Figure 5.10(a) as reported in Kumari's dissertation.[134] The 346 and 356 cm^{-1} vibrational intervals have been identified as La-hydrocarbon symmetric stretching mixed with H wagging of the neutral and cation respectively. The $^3A \leftarrow ^2A_1$ transition of this isomer was considered in the present work, but was ruled out since the predicted IE (54720 cm^{-1}) for this transition is too high compared to the experimental value. Besides the $^2A_1$ ground state, a quartet excited state (^4A) was predicted for isomer A. In this high spin state, the La metal maintains weaker interactions with the central C (C_1 in Figure 5.8), stronger interactions with one of the terminal C (C_3 in Figure 5.8), and much weaker interactions with the rest of the terminal C atoms (C_2 and C_4 in Figure 5.8) than those in the $^2A_1$ ground state. Because the La-C_2, -C_3, and -C_4 bond lengths are unequal, the molecular symmetry in the ^4A state is reduced to C_1 from C_{3v} in the ground state. Since it is high in energy (16342 cm^{-1} , 2.03 eV), the ^4A state is unlikely to survive in the supersonic molecular beam. Moreover, the IE of $^3A \leftarrow ^4A$ (38378 cm^{-1}) is considerably low compared to the measured value. Thus, the $^3A \leftarrow ^4A$ transition can be ruled out from the observed spectrum. Therefore, we must consider other possible isomers in order to assign the MATI spectrum in Figure 5.9(a). Isomer B (1-lanthana-3-cyclopentene), a metallacycle, is predicted at slightly higher in energy (157 cm^{-1}) than isomer A. This isomer has C_s symmetry with the ground electronic state of $^2A'$. In the $^2A'$ ground state of isomer B, La is located on a different plane from the carbon skeleton's plane and maintains stronger interactions with the terminal C (C_1 and C_4 in Figure 5.8) atoms than with the internal C (C_2 and C_3 in Figure 5.8) atoms. In contrast to the $^2A'$ state, La maintains weaker interactions with the terminal C atoms than with the internal C atoms in an excited $^4A'$ state at 9991 cm^{-1}. Among all possible transitions of isomer B, we have found that only the $^1A' \leftarrow ^2A'$ transition contributes to the observed MATI spectrum in Figure 5.9 (a), as shown by the comparison of the simulated and measured spectra. The IE of this transition (40050 cm^{-1}) agrees well with the observed value (39455 cm^{-1}). We have also considered isomers C and D and found that these two high energy isomers are not responsible for the MATI spectrum in Figure 5.9. Isomer C is the trans form of isomer B. The ^2A ground state of isomer C is predicted to be in C_2 symmetry at 3782 cm^{-1}. The simulation of $^1A \leftarrow ^2A$ transition of isomer C (Figure 5.9 (c)) does not produce the experimental spectrum. A quartet excited state (^4B) predicted at 7439 cm^{-1} above the ^2A ground state is unlikely to survive in the supersonic molecular beam. Isomer D was previously proposed by Schwarz and coworkers in their FT MS / Collision Induces Dissociation (CID) measurements as a possible isomer of $Ce^+(C_4H_6)$ formed by the reaction between Ce^+ and C_3H_6.[11] However, since it has a very high energy (19900 cm^{-1} above isomer A), and ionization leads to a large structural change, isomer D is very unlikely candidate for the observed MATI spectrum. Therefore the observed MATI spectrum is clearly from the $^1A' \leftarrow ^2A'$ transition of isomer B. The 26 cm^{-1} sequence bands arise from the sequence transitions between the excited in-plane carbon skeleton bending mixed with the hydrogen wagging vibration levels of neutral and cation electronic states. The 320 cm^{-1} interval is due to the vibrational excitation of an out of plane ring bending mixed with a central H wagging motion of the cation complex and 285 cm^{-1} is the same vibrational mode of the neutral state. The 370 and 398 cm^{-1} vibrational intervals are related to an in-plane carbon skeleton bending mixed with a H rocking and a La-hydrocarbon stretching motion of the neutral and cation states, respectively. The 470 cm^{-1} interval is related to a H twisting motion of the cation. Calculated vibrational frequencies for all the observed modes are in excellent agreements with the measured values (Table 5.3). The band assignments of the

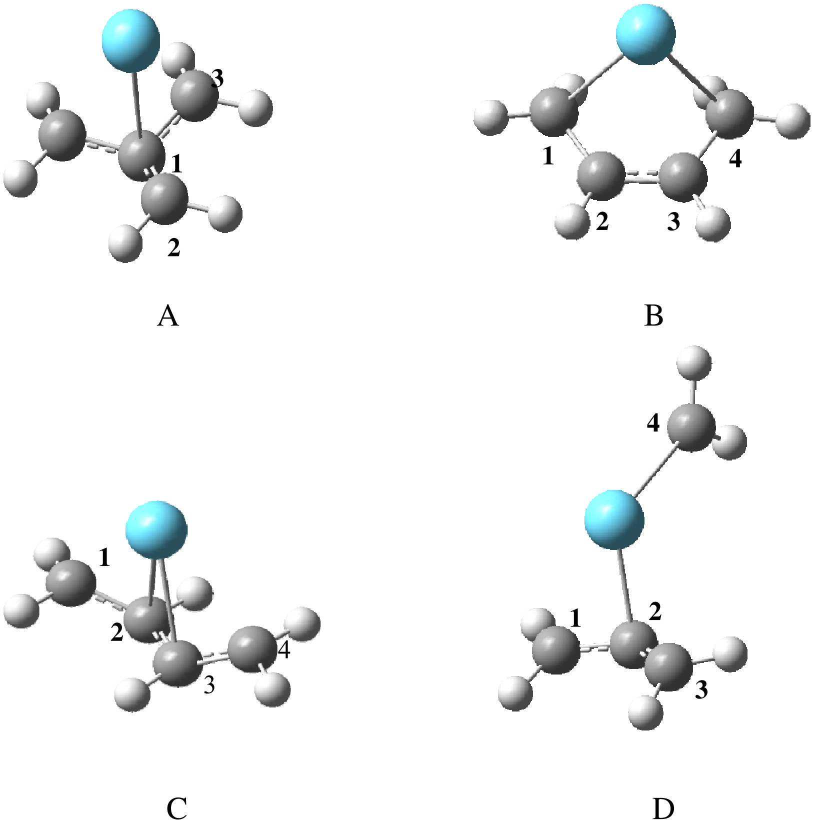

Figure 5.8 Possible structural isomers of LaC_4H_6.

Table 5.2 Point groups (PG), electronic states, relative energies (E_0, cm^{-1}), bond lengths (Å), and bond angles (degrees) of the LaC_4H_6 isomers calculated at the DFT / B3LYP level. The atomic labels are the same as those in Figure 5.8

	A		**B**		**C**		**D**	
	$^2A_1$	^4A	$^2A'$	$^4A''$	^2A	^4B	$^2A'$	$^4A''$
PG	C_{3v}	C_1	C_s	C_s	C_2	C_2	C_s	C_s
E_0	0	16342	157	10148	3782	11221	19900	27052
La-C_1	2.48	2.71	2.51	2.80	2.63	2.85	2.70	2.73
La-C_2	2.58	3.16	2.67	2.74	2.52	2.63	2.29	2.64
La-C_3	2.58	2.56						
La-C_4	2.58	3.09					2.45	2.42
C_1-C_2	1.43	1.41	1.45	1.39	1.43	1.39		
C_2-C_3			1.39	1.44	1.40	1.45		
C_1-C_3	1.43	1.45						
C_1-C_4	1.09	1.08						
<C_1-C_2-C_3			125	124	125	122	129	147
<C_2-C_1-C_3	116	120						
<C_2-C_1-C_4	116	116						
<C_3-C_1-C_4	116	121						

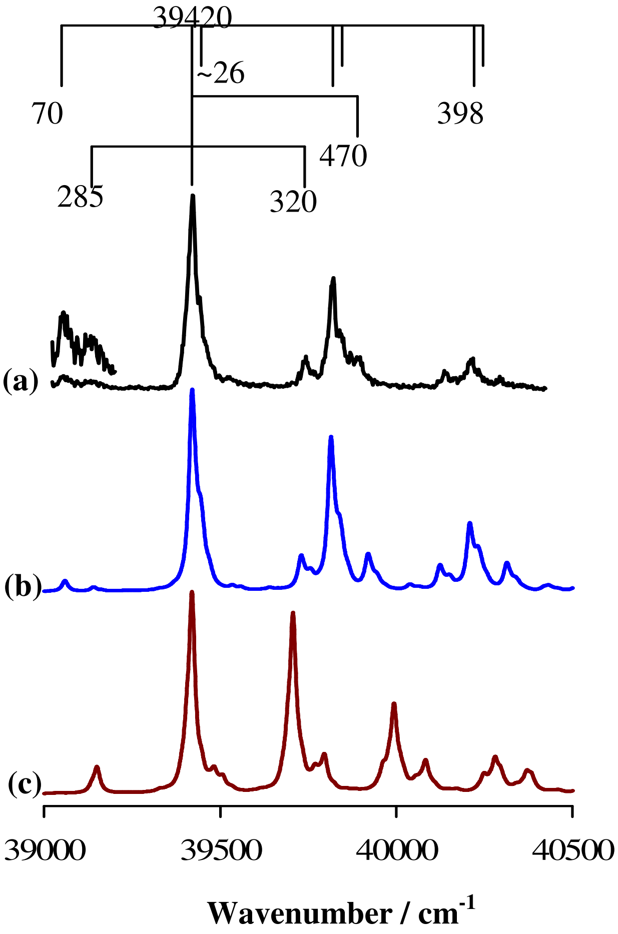

Figure 5.9 MATI spectrum of LaC_4H_6 (a), and the simulated spectra of the $^1A' \leftarrow {}^2A'$ transition of isomer B (b) and the $^1A \leftarrow {}^2A$ transition of isomer C (c). The simulations are done at 200 K with the FWHM of 20 cm^{-1}.

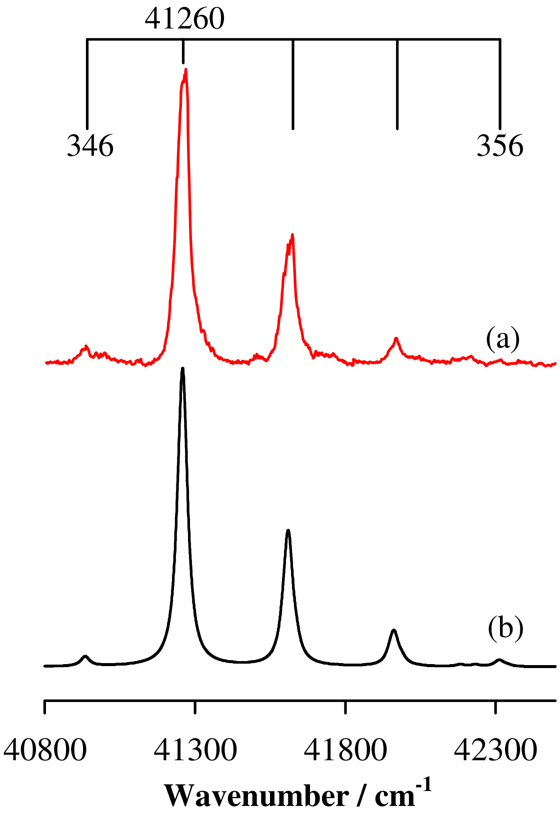

Figure 5.10 MATI spectrum of LaC_4H_6 (a) and the simulated spectrum of the $^1A_1 \leftarrow ^2A_1$ transition of isomer A with the FWHM of 20 cm^{-1} at 200 K (b).[134]

MATI spectra of two LaC_4H_6 isomers can be found in Table 5.4.

5.3.3 Isotopic Shift Induced by Deuterium Substitution

The deuterium substituted propene is used to investigate the isotopic shift. We have successfully recorded MATI spectra of LaC_4D_6, but were not able to isolate MATI signal of $LaCD_2$. The $LaCD_2$ ion signal produced by direct photoionization was buried underneath of the LaO ion signal since $LaCD_2$ and LaO have the same mass. Again, due to strong MATI bands of LaO, those of $LaCD_2$ were not distinguishable in the measured MATI spectrum. The MATI spectra of LaC_4D_6 corresponding to isomers B and A are presented in Figures 5.11 and 5.12 respectively, and the IEs and vibrational frequencies measured from these spectra are summarized in Table 5.4. The IE of deuterium substituted isomer A is 41230 (5) cm^{-1} and is 30 cm^{-1} red shifted from that of the parent complex (41260 (5) cm^{-1}) due to differential changes of the vibrational zero-point energies in the neutral and ion states. Again, the deuterium substitution reduces the frequency of the La-hydrocarbon symmetric stretching mixed with H wagging (ν_{12}) motion by 44 and 28 cm^{-1} in the neutral an ion states, respectively. For isomer B, the deuterium substitution decreases the IE by 21 cm^{-1}. The deuterium substitution also reduces the vibrational frequency of H twisting motion (υ_{11}^+) by 83 cm^{-1}. For ν_{12} and ν_{13}, the experimental frequencies are hard to measure accurately due to the overlap of the MATI bands. However, we have theoretically predicted considerable shifts for these two modes (Table 5.4). The shifts are 50 and 59 cm^{-1} for ν_{12} and ν_{12}^+ and 28 and 30 cm^{-1} for ν_{13} and ν_{13}^+, respectively. ν_{12} is an in-plane C skeleton bending with H rocking mixed with a La-hydrocarbon stretching. ν_{13} is an out of plane ring bending with central H wagging. In both cases, the involvement of the H rocking or waging motion contributes to the large isotopic shift.

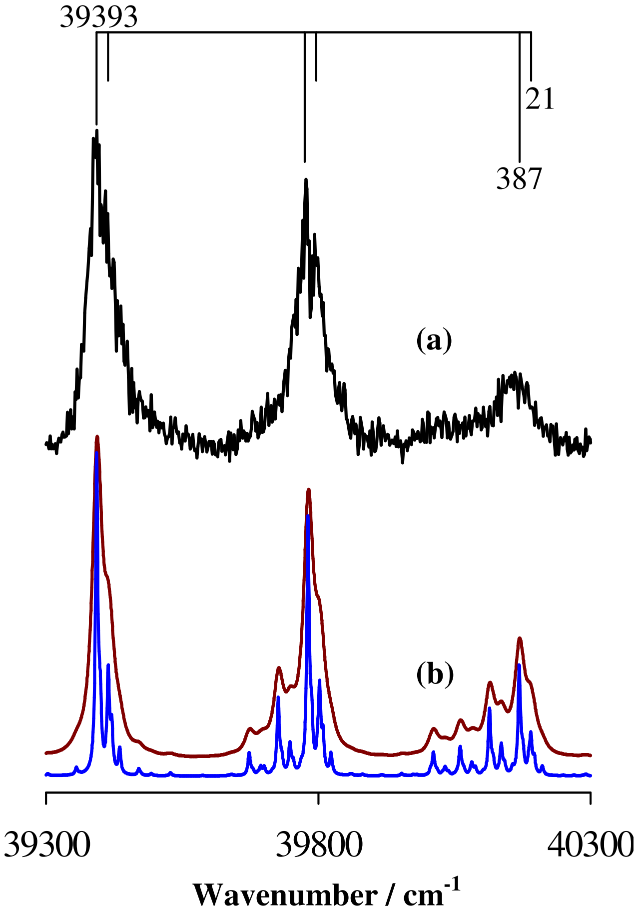

Figure 5.11 MATI spectrum of LaC_4D_6 (a) and the simulated spectra of the $^1A' \leftarrow {}^2A'$ transition of isomer B with FWHMs of 20 cm^{-1} (b, dark red) and 5 cm^{-1} (b, blue) at 200K.

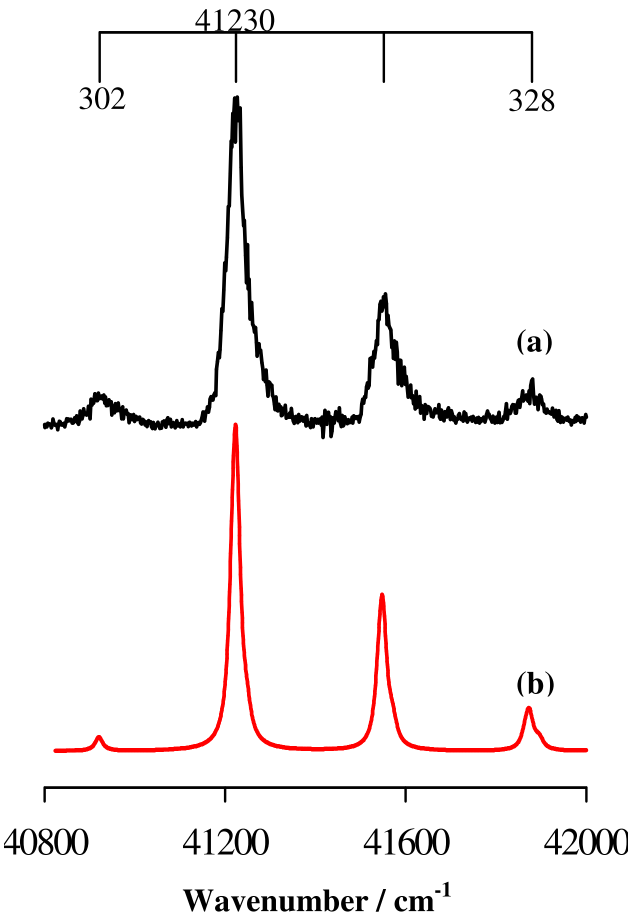

Figure 5.12 The MATI spectrum of LaC_4D_6 (a) and the simulated spectrum of the $^1A_1 \leftarrow ^2A_1$ transition of isomer A (b) with a FWHM of 20 cm^{-1} at 200K.

Table 5.3 Adiabatic ionization energies (AIE, cm^{-1}) and vibrational frequencies (cm^{-1}) of $LaCH_2$ and two isomers of $La(C_4H_6)$ / $La(C_4D_6)$ from MATI measurements and DFT / B3LYP calculations. The uncertainty of the experimental IE values is 5 cm^{-1}

	MATI	B3LYP
$LaCH_2$, C_s		
AIE : $^1A' \leftarrow {}^2A'$	42263	43064
H rocking of cation	446	467
La- C stretching of cation	677	697
$La(C_4H_6)$ / $La(C_4D_6)$, C_{3v}: Isomer A		
AIE : $^1A_1 \leftarrow {}^2A_2$	41260 / 41230	41806 / 41770
La- hydrocarbon symmetric stretching, H wagging of neutral, υ_{12}	346 / 302	326 / 303
La^+- hydrocarbon symmetric stretching, H wagging of cation, υ_{12}^+	356 / 328	351 / 325
$La(C_4H_6)$ / $La(C_4D_6)$, C_s : Isomer B		
AIE : $^1A' \leftarrow {}^2A'$	39420 / 39393	40178 / 40145
In plane C skeleton bending, terminal and central H wagging (υ_{14}^+ - υ_{14})	~26 / ~21	24 / 21
Out of plane ring bending, central H wagging of neutral, υ_{13}	285 / -	280 / 252
Out of plane ring bending, central H wagging of cation, υ_{13}^+	320 / -	310 / 280
In plane C skeleton bending, H rocking, La-hydrocarbon stretching, υ_{12}	370 / -	360 / 310
In plane C skeleton bending, H rocking, La^+-hydrocarbon stretching, υ_{12}^+	398 / -	391 / 330
H twisting of cation, υ_{11}^+	470 / 387	492 / 386

Table 5.4 MATI band positions (cm^{-1}) and assignments of $LaCH_2$ and two isomers of LaC_4H_6. The uncertainty associated with the band positions is 5 cm^{-1}

$LaCH_2$		lanthanum-trimethylenemethane		1-lanthana-3-cyclopetene	
Position	Assignment	Position	Assignment	Position	Assignment
42263	0^0_0	40914	12^0_1	39050	12^0_1
42709	5^1_0	41260	0^0_0	39135	13^0_1
42940	4^1_0	41616	12^1_0	39420	0^0_0
43386	$5^1_0 4^1_0$	41972	12^2_0	39446	14^1_1
43617	4^2_0	42428	12^3_0	39740	13^1_0
				39818	12^1_0
				39844	$12^1_0 14^1_1$
				39890	11^1_0
				40138	$12^1_0 13^1_0$
				40198	12^2_0
				40224	$12^2_0 14^1_1$
				40288	$11^1_0 12^1_0$

5.3.4 Reaction Pathways for the Formation of $LaCH_2$ and LaC_4H_6

We have confirmed that the bond activation of propyne is La metal assisted, rather than the vaporization laser assisted by conducting a similar control experiment as described in Chapter 3 (sections 3.2, 3.3.3) and Chapter 4 (sections 4.2, 4.3.2).

$La + CH_3CH{=}CH_2 \rightarrow LaCH_2 + H_2C{=}CH_2$

$LaCH_2 + CH_3CH{=}CH_2 \rightarrow LaC_4H_6 + H_2$

$LaCH_2$ is produced by the primary reaction between La metal and $CH_3CH{=}CH_2$ as shown above. The predicted reaction pathway for the $LaCH_2$ formation is shown in Figure 5.13 and structures of stationary points in details are shown in Figure 5.14. According to our theoretical predictions, La metal atom interacts with the double bond of propene to form an metal association complex (IM1) at the initial step of the reaction. IM1 is 124.1 $kJmol^{-1}$ lower in energy than the reactants. In the next step, La inserts into one of the C-H bonds in the CH_3 group to form the metal insertion intermediate IM2 through the transition state TS1. IM2 is 164.3 kJ mol^{-1} below the reactants and is the most stable species along the reaction coordinate. We have experimentally identified the structure of IM2 as a lanthanum allyl hydride in a previous study using La and propene.[134] A similar metal allyl hydride was also proposed in the reaction of V atom with propene in an Ar matrix by FTIR measurement.[11] In the third step, reverse hydrogen migration from the La center toward the central C atom forms the metallacyclobutane intermediate IM3 via the transition state TS2. Unfortunately, we were not able to confirm the existence of IM3 by MATI measurements even after numerous attempts. IM3 leads to IM4 via undefined transition state. Finally, $LaCH_2$ is formed by the C-C bond dissociation of IM4. The proposed pathway for the La + propene reaction is similar to what was previously proposed for the Y + propene reaction by Tao *et al.* from their DFT calculations other than the formation of

YCH_2 is endothermic in their work and the formation of $LaCH_2$ is exothermic in our theoretical prediction.[21] However, the spectroscopic identification of MCH_2 (M = metal atom or ion) has not been previously reported.

LaC_4H_6 is formed through a secondary reaction between $LaCH_2$ and $CH_3CH=CH_2$. Figure 5.15 and 5.16 respectively display the reaction pathway for the formation of isomer B and structures of stationary points in details. Formation of isomer A has been disscussed in Kumari's dissertation.[134] In the initial step of the formation of isomer B, the La atom in $LaCH_2$ interacts with the C=C double bond in $CH_3CH=CH_2$ to form IM6. Then the carbon atom in $LaCH_2$ interacts with the terminal sp^2 carbon atom of propene via TS3 to form IM7, a four member metallacycle. After the formation of this metallacycle, La mediated C-H bond activation occurs at a central C atom (terminal sp^2 carbon of propene) to form IM8 via TS4, followed by a socond C-H activation of CH_3 group to form IM9 via TS5. The concerted H_2 elimination from IM9 via TS6 and IM10 forms isomer B of LaC_4H_6. Along the reaction coordinate, all intermediates have lower energy than the reactants. We have predicted the reaction pathway for the formation of isomer A[134] and B of LaC_4H_6 from La + propene reaction and identified their structures spectroscopically for the first time.

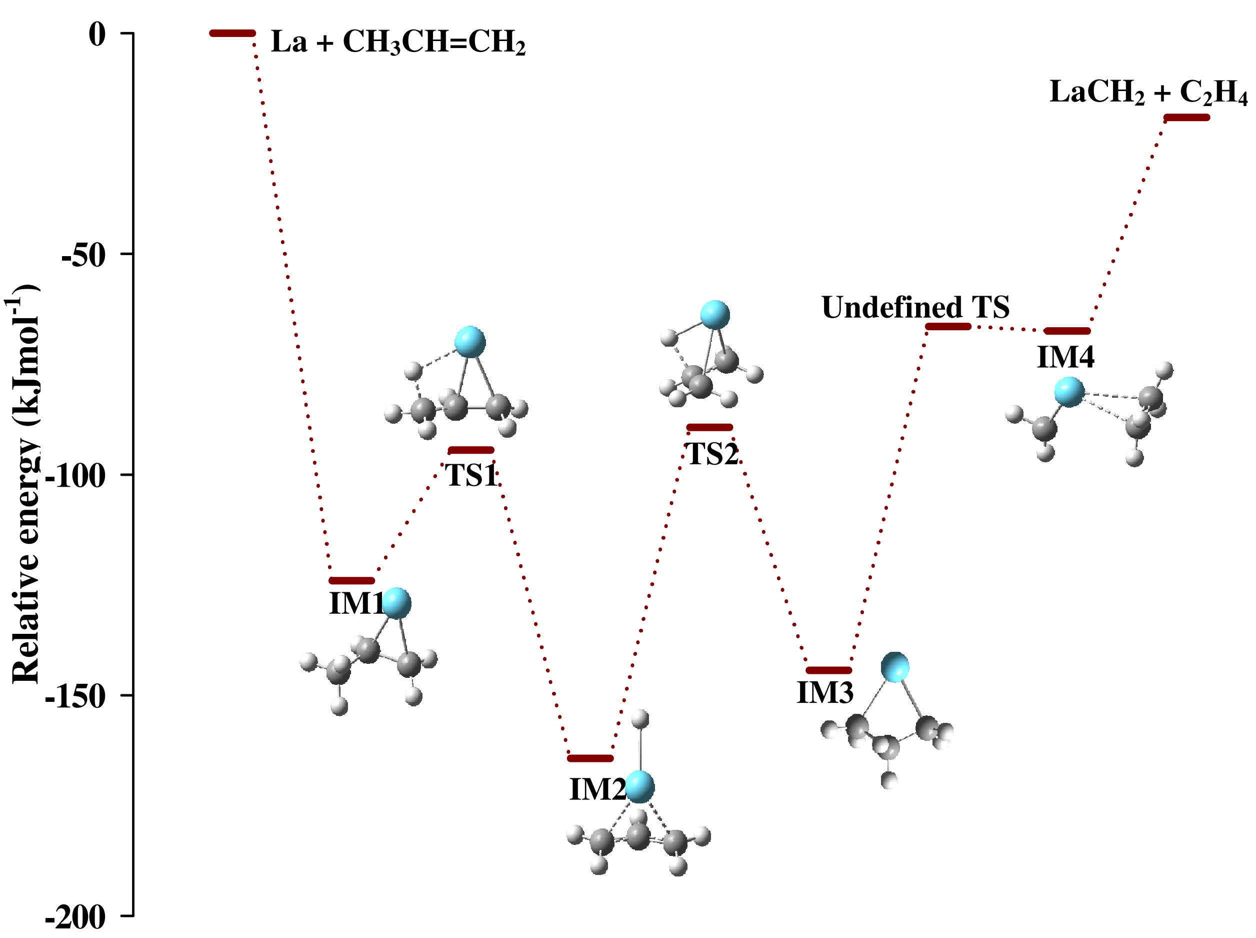

Figure 5.13 Reaction pathway for the formation of $LaCH_2$ from the reaction between La and $CH_3CH=CH_2$ calculated at the DFT/B3LYP level. TS : Transition States, IM : Intermediates.

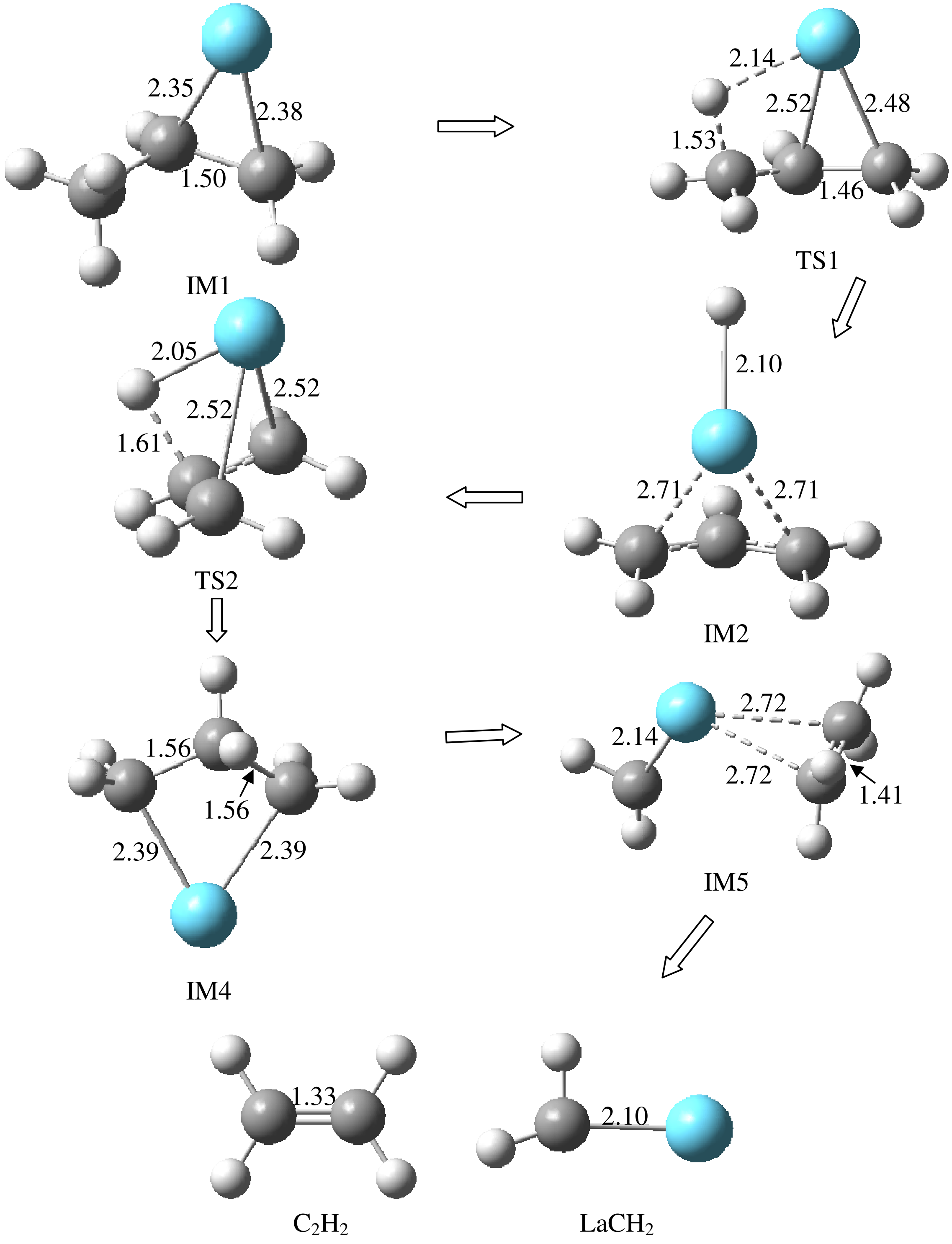

Figure 5.14 Stationary points of the reaction pathway for the formation of $LaCH_2$ from the reaction between La and $CH_3CH{=}CH_2$ calculated at the DFT / B3LYP level.

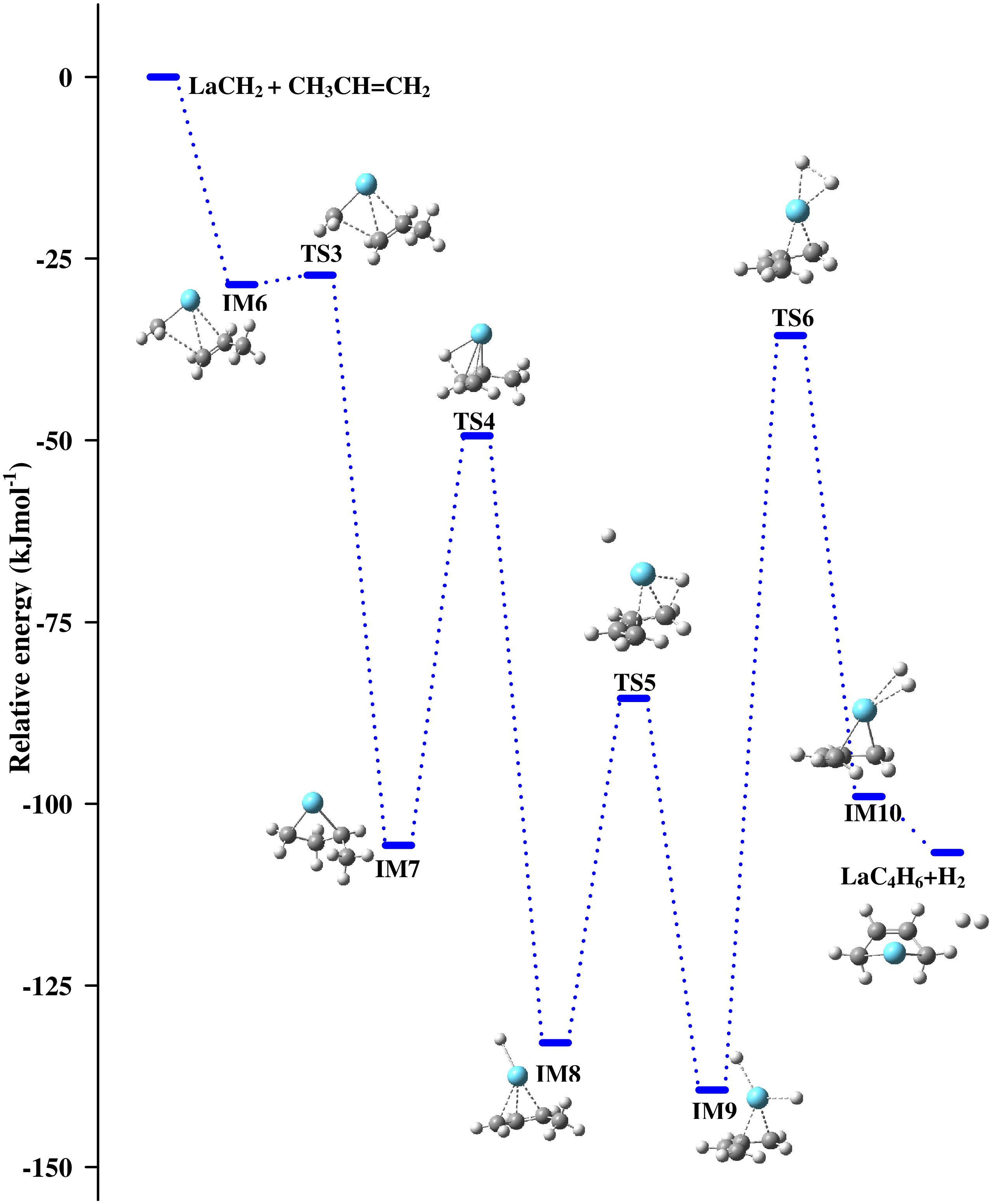

Figure 5.15 Reaction pathway for the formation of isomer B of LaC_4H_6 from the reaction between $LaCH_2$ and $CH_3CH=CH_2$ at the DFT/B3LYP level. TS: Transition States, IM: Intermediates.

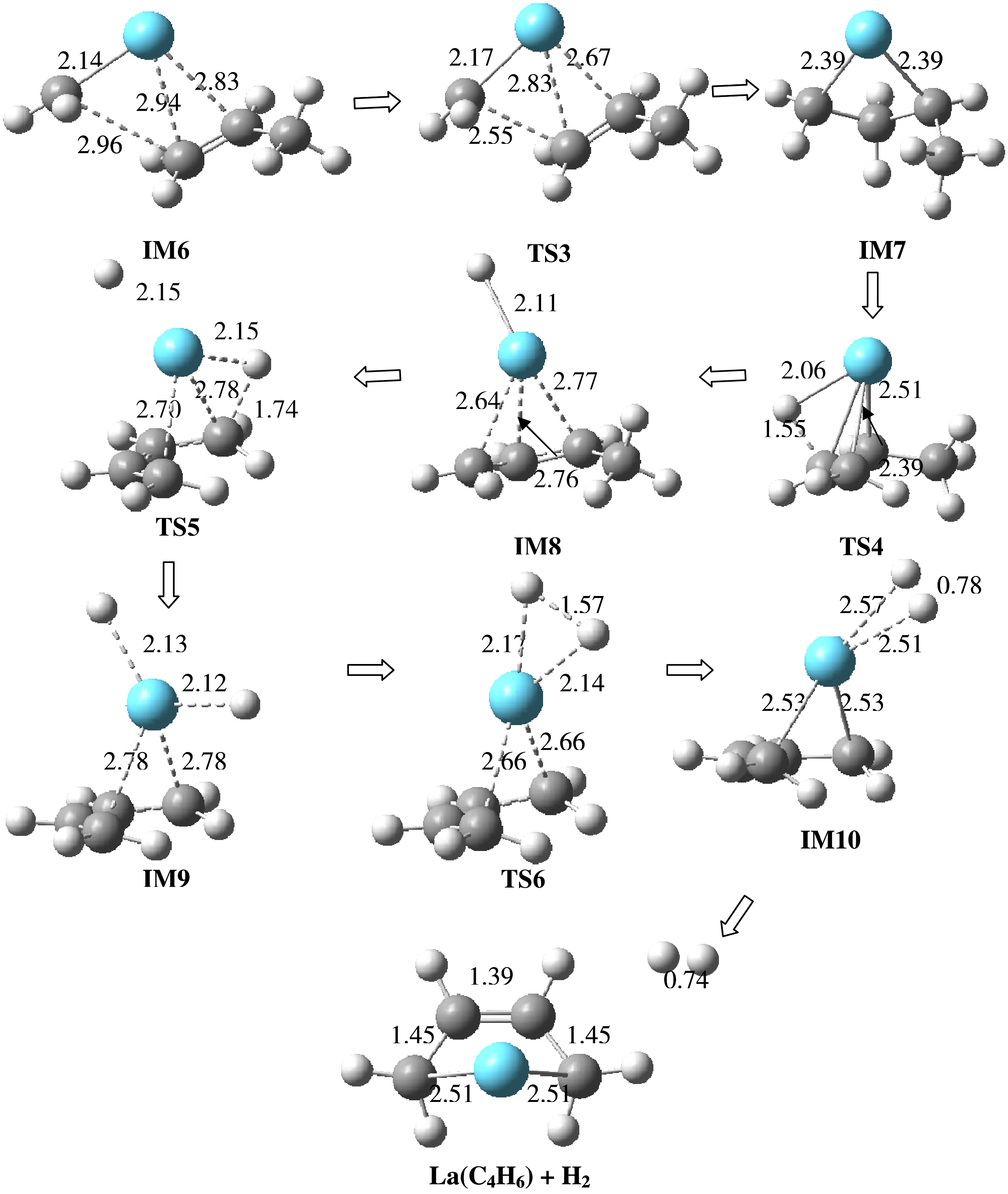

Figure 5.16 Stationary points of the reaction pathway for the formation of isomer B of LaC_4H_6 from the reaction between $LaCH_2$ and $CH_3CH{=}CH_2$ calculated at the DFT/B3LYP level.

5.4 Conclusions

The structures, electronic states and formations of $LaCH_2$ and two isomers of LaC_4H_6 have been investigated using MATI spectroscopy and DFT calculations. $LaCH_2$ is formed by the C-C bond breakage and 1,2-hydride shift of propene. It has a C_s symmetry and the structure prefers the neutral and cationic electronic states of $^2A'$ and $^1A'$, respectively. The AIE of $LaCH_2$ is measured to be 42263 (5) cm^{-1}. The α agostic interaction in $LaCH_2$ is identified by the theoretical calcultions. LaC_4H_6 is formed by the reaction of $LaCH_2$ with a second propene molecule by C-C bond coupling followed by dehydrogenation. Two structural isomers, lanthanum trimethylenemethane (isomer A)[134] and 1-lanthana-3-cyclopentene (isomer B), have been identified for the complex. Lanthanum trimethylenemethane has a C_{3v} symmetry, whereas 1-lanthana-3-cyclopentene has a C_s symmetry. The preferred neutral and cationic electronic states of lanthanum trimethylenemethane are $^2A_1$ and $^1A_1$,[134] and those of 1-lanthana-3-cyclopentene are $^2A'$ and $^1A'$, respectively. The AIEs of lanthanum trimethylenemethane and 1-lanthana-3-cyclopentene are measured to be 41260 (5)[134] and 39420 (5) cm^{-1}, respectively. Isotopic shift induced by deuterium substitution on IEs and vibrational frequencies have been determined for LaC_4H_6. Deuteration of LaC_4H_6 has a considerable effect on the AIEs of the two isomers and significant effect on the frequencies of the vibrational modes involving considerable H motions. La-hydrocarbon stretching modes have been observed to be the most active vibrational modes for both $LaCH_2$ and LaC_4H_6 (two isomers).

CHAPTER 6. C-C AND C-H BOND ACTIVATION, AND COUPLING OF 1,3-BUTADIENE INDUCED BY LANTHANUM ATOM

6.1 Introduction

1,3-butadiene (CH_2=CHCH=CH_2, butadiene) is a commercially important chemical since it is used as a building block in the production of synthetic rubber, styrene-butadiene latex, and nitrile rubber.[188] It is also used to synthesize common organic compounds, such as cyclooctadiene and cyclododecatriene via nickel- or titanium-catalyzed dimerization and trimerization reactions.Because of its wide uses in organic synthesis and chemical industry, metal-promoted butadiene activations have attracted considerable attentions in both gas[189-194] and condensed[153,195-205] phase studies. . For gas phase studies, Castleman et al. have reported the product branching ratios forthe reactions between 1,3-butadiene and tantalum oxide cluster cations ($TaO_{2\text{-}3}^+$, $Ta_2O_{4\text{-}5}^+$, $Ta_3O_{7\text{-}8}^+$). They have observed $Ta_xO_yC_2H_4$ as the major product in most of the reactions as a result of the C_2-C_3 bond cracking. [189,190] The same group has studied the effects of the oxidation states, structures, and sizes of the vanadium oxide cluster cations ($V_2O_{4\text{-}6}^+$, $V_3O_{6\text{-}9}^+$, $V_4O_{8\text{-}10}^+$, $V_5O_{11\text{-}13}^+$, $V_6O_{13\text{-}15}^+$, $V_7O_{16\text{-}18}^+$) on the bond activation of 1,3-butadiene.[191] Beside the C_2-C_3 bond cleavage, they have also observed the products formed by association and dehydrogenation reactions. Schwarz et al. have studied the M^+ (M =Cr, Mn, Fe, and Co) mediated cycloaddition of butadiene and acetylene and observed the formation of the M^+-benzene complexes.[192] Bakhtiar et al. have studied Fe^+ mediated cycloaddition of butadine to acetylene and propyne and observed the formation of Fe^+-benzene and Fe^+-toluene, respectively.[193] For condensed phases, the previous studies have focused on the selective hydrogenation and regio- and/or stereo specific polymerization of butadiene by first and second raw transition metal complexes.[153,195-205] In either the gas or condensed phase, however, studies of the spectroscopy and structures of the reaction products are limited. In this chapter, I will describe the structures and electronic states of the products formed by the La mediated bond activation of butadiene and the reaction pathways for the products formation.

6.2 Experimental and Computational Details

The metal-cluster beam instrument used in this work consists of the reaction and spectroscopy vacuum chambers and was described in Chapter 2. The metal-hydrocarbon reaction was carried out in a laser vaporization metal cluster beam source. CH_2=CHCH=CH_2 ($\geq$ 99%, Sigma-Aldrich) was seeded in a He carrier gas with a concentration of 10^{-4} - 10^{-5} in a stainless steel mixing cylinder. La atoms were generated by pulsed-laser (Nd:YAG, Continuum Minilite II, 535 nm, 1.0-1.5 mJ/pulse) vaporization of a La rod (99.9%, Alfa Aesar) in the presence of the hydrocarbon/He mixture (40 psi) delivered by a home-made piezoelectric pulsed valve. The metal atoms and gas mixture entered into a clustering tube (2 mm diameter and 2 cm length) where the chemical reaction occurred. The reaction mixture was then expanded into the reaction chamber, collimated by a cone-shaped skimmer (2 mm inner diameter), and passed through a pair of deflection plates. Ionic species in the molecular beam that were formed during laser vaporization were removed by a electric field (100 Vcm^{-1}) applied on the deflection plates. The neutral products were identified by photoionization time-of-flight mass spectrometry.

Prior to the MATI measurements, photoionization efficiency spectra of La complexes were recorded to locate their approximate ionization thresholds to simplify the MATI experiment. In the MATI experiment, the complexes were excited to high-lying Rydberg states in a single-photon process and ionized by a delayed pulsed electric field. The excitation laser was the same as that for photoionization in the mass spectrometry and photoionization efficiency experiments and was the frequency doubled output of a tunable dye laser (Lumonics HD-500), pumped by the third harmonic output (355 nm) of a Nd:YAG laser (Continuum Surelite II). The laser beam was collinear and counter propagating with the molecular beam. The ionization pulsed field (320 V cm^{-1}) was generated by two high voltage pulse generators (DEI, PVX-4140) and delayed by 10-20 μs from the laser pulse by a delayed pulsed generator (SRS, DG641). A small DC field (6.0 V cm^{-1}) was applied to separate the prompt ions produced by direct photoionization from the MATI ions generated by delayed field ionization. The MATI ion signal was obtained by scanning the wavelength of the tunable dye laser, detected by a dual microchannel plate detector, amplified by a preamplifier (SRS, SR445), averaged by a gated integrator (SRS, SR280), visualized by a digital oscilloscope (Tektronix TDS 3012), and stored in a laboratory computer. Laser wavelengths were calibrated against vanadium atomic transitions in the spectral region.[129] The Stark shift induced by the DC separation field was calculated using the relation of $\Delta IE = 6.1E_f^{1/2}$, where E_f is in V cm^{-1} and ΔE is in cm^{-1}.[130]

Geometry optimization and vibrational frequency calculations were carried out using Gaussian 03 software package.[92] In these calculations, we used the Becke's three-parameter hybrid functional with the correlation functional of Lee, Yang, and Parr (B3LYP)[82,83] and 6-311+G(d,p)[93,94] basis set for C and H and the effective-core-potential SDD[95] basis set for La. We have extensively used DFT/B3LYP and found this method to generally produce adequate results for helping the spectral and structural assignments of organometallic radicals.[131] No symmetry constraints were imposed in initial geometry optimizations. However, geometry re-optimizations with appropriate symmetry constraints (i.e. with defined point groups) were carried out to identify the electronic symmetries. For each optimized stationary point, vibrational analysis was performed to identify the nature of the stationary point (minimum or saddle point). In predicting reaction pathways, minima connected by a transition state were confirmed by intrinsic reaction coordinate calculations.

To compare with the experimental MATI spectra, multi-dimensional FC factors were calculated from the equilibrium geometries, harmonic vibrational frequencies, and normal coordinates of the neutral and ionized complexes.[132] In these calculations, the recursion relations from Doktorov et al.[133] were employed, and the Duschinsky effect[99] was considered to account for a possible axis rotation from the neutral complex to the cation. Spectral simulations were obtained using the experimental linewidth and a Lorentzian line shape. Transitions from excited vibrational levels of the neutral complex were considered by assuming thermal excitation at specific temperatures.

6.3 Results and Discussion

The TOF-MS spectrum recorded for the reaction between La and butadiene at the laser ionization wavelength of 220 nm is shown in Figure 6.1. The metal complexes identified in the mass spectrum are LaC_2H_2, LaC_4H_4, LaC_4H_6, LaC_6H_6 and LaC_6H_8. The primary products of the reaction are LaC_2H_2, LaC_4H_4 and LaC_4H_6. LaC_2H_2 is assumed to be formed by the C-C bond activation and H shifts of 1,3-butadiene, whereas LaC_4H_4 is formed by the dehydrogenation of butadiene. LaC_4H_6 is the association complex of the reaction. The smaller primary products react with a second butadiene molecule to produce the secondary products of LaC_6H_6 and LaC_6H_8. Figure 6.2 displays the PIE spectra of the complexes, except for that of LaC_6H_8. Each spectrum begins with a slowly rising signal followed by a sharp signal onset. The slowly rising signal originates from the ionization of thermally excited vibrational levels of the neutral complex. The sharp signal onsets, indicated by the arrows, correspond to the first ionization threshold of the complexes.

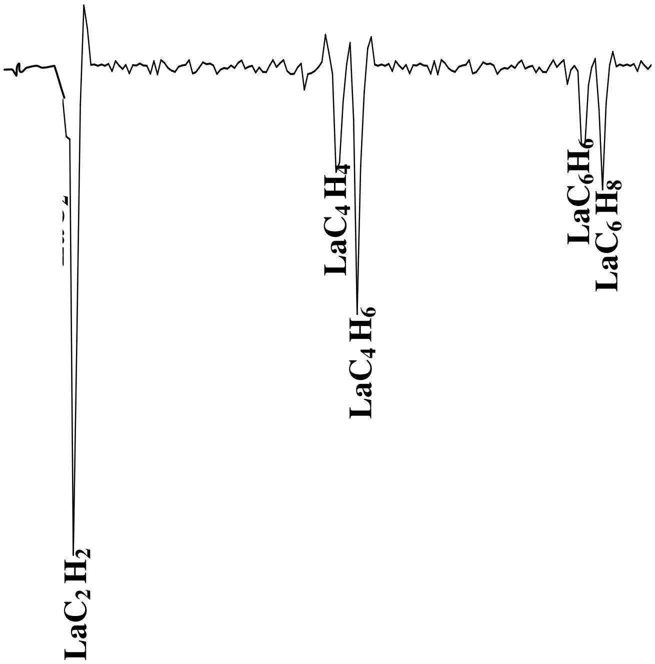

Figure 6.1 TOF-MS spectrum of the La + 1,3-butadiene reaction recorded at the ionization laser wavelength of 220 nm. The seeding concentration of 1,3-butadiene in He is 10^{-5}.

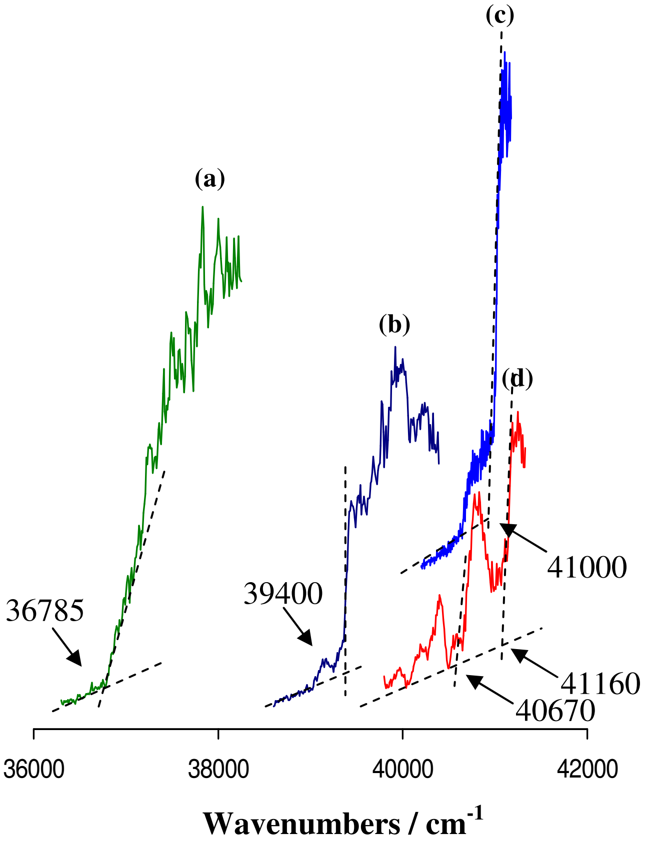

Figure 6.2 PIE spectra of LaC$_6$H$_6$ (a), LaC$_4$H$_6$ (b), LaC$_4$H$_4$ (c) and LaC$_2$H$_2$ (d).

6.3.1 LaC_2H_2

The PIE spectrum of LaC_2H_2 (Figure 6.2(d)) has two sharp onsets separated by about 490 cm^{-1} : the first one is at 40670 (50) cm^{-1} and the second at 41160 (50) cm^{-1}. The positions of the sharp onsets were used to search for and correlate with the MATI signal. The strongest band (i.e., the origin band) of the MATI spectrum is located at 41165 (5) cm^{-1} as shown in Figure 6.4(a). This band position corresponds to the second sharp signal onset of the PIE spectrum (Figure 6.2(d)). Above the origin band, the MATI spectrum shows a 520 cm^{-1} major progression and a 800 cm^{-1} interval. Below the origin band, the spectrum displays a 490 cm^{-1} short progression and a 800 cm^{-1} interval, which presumably originate from the transitions of the thermally excited vibrational levels of the neutral complex. The band located at 490 cm^{-1} below the origin band (40675 cm^{-1}) corresponds to the first sharp onset of the PIE spectrum (Figure 6.2(d)) of the complex.

The theoretical calculations were carried out to help the spectral and structural assignments. Two possible structural isomers of LaC_2H_2: La-CCH_2 and La-η^2-HCCH, were considered in the geometry optimization. La-CCH_2 is formed by a 2,3-H shift and the C_2-C_3 bond activation, whereas La-η^2-HCCH is formed by a 1,3-H shift and the C_2-C_3 bond activation. Both isomers are in C_{2v} symmetry, and La-η^2-HCCH is 6923 cm^{-1} more stable than La-CCH_2. The neutral and cation ground electronic states of both isomers are $^2A_1$ and $^1A_1$, respectively. Since we have constantly observed only the low spin states of the metal complexes in our previous works, high spin states were not considered in this work. The geometries of two isomers are presented in Figure 6.3 and Table 6.1. The La-$C_{1,2}$ bond lengths of La-η^2-HCCH are 2.31 Å, and the two C atoms are covalently bound to La. The C_1-C_2 bond length is 1.35 Å, suggesting that a double bond exists between C_1 and C_2. The La-C_2 bond length of La-CCH_2 is much shorter than the La-$C_{1,2}$ bond lengths of La-η^2-HCCH, suggesting that a double bond exists between La and C_2. Upon ionization, La-C bond lengths are considerably reduced in both isomers. However, ionization has negligible effects on the organic fragments.

The simulated spectrum of the $^1A_1 \leftarrow {}^2A_1$ electronic transition of La-η^2-HCCH is shown in Figure 6.4(b), which matches nicely with the experimental MATI spectrum. For this transition, the predicted IE (41908 cm^{-1}) agrees well with the observed one (, IE: 41165 cm^{-1}) too. On the other hand, the simulation of the $^1A_1 \leftarrow {}^2A_1$ transition of La-CCH_2 exhibits considerable differences from the experimental spectrum. Although it displays a similar FC profile and reasonable IE (42370 cm^{-1}) to the experimental spectrum, the predicted vibrational frequency (480 cm^{-1}) of the major progression is much smaller than the measured value (520 cm^{-1}). Second, the 800 cm^{-1} band in the experimental spectrum is missing in the simulation. Third, many sequence bands are predicted to be overlapped with the major progression in the simulation, but they are not presented in the experimental spectrum. Therefore, the experimental spectrum is clearly from the $^1A_1 \leftarrow {}^2A_1$ transition of the La-η^2-HCCH isomer, rather than that of La-CCH_2. The significant decrease of the La-$C_{1,2}$ bond lengths of La-η^2-HCCH upon ionization is consistent with the strong FC activity of the La-hydrocarbon stretching mode observed in the MATI spectrum. The La-hydrocarbon stretching frequencies are measured to be 520 and 490 cm^{-1} for the cation and neutral states, respectively. The frequencies of a H scissoring motion are measured to be 800 cm^{-1} for both the cation and neutral states. These observed frequencies are nicely reproduced by theory for the La-η^2-HCCH. Table 6.3 summarizes the experimental and theoretical IEs and vibrational frequencies.

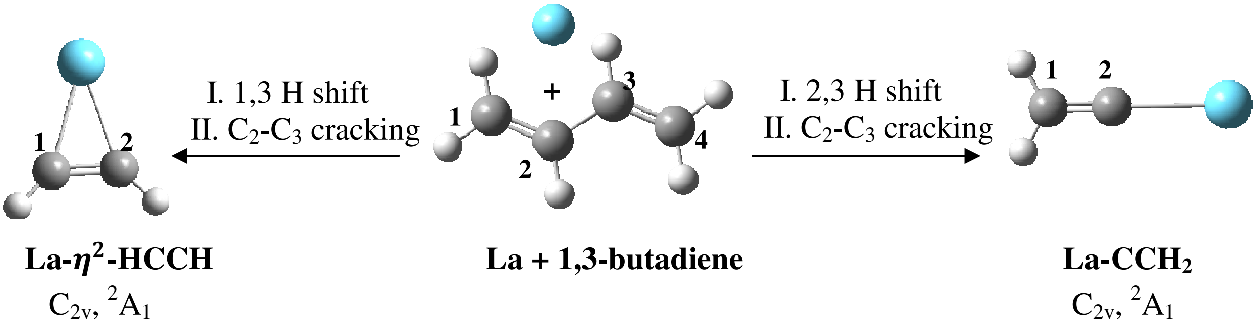

Figure 6.3 Isomers of LaC_2H_2 formed by La mediated H shifts and C-C bond activation of 1,3-butadine. The point groups and electronic states of the isomers are listed below the structures.

Table 6.1 Electronic states (ES), relative energies (E_0, cm^{-1}), and bond lengths (Å) and angles (degrees) of the LaC_2H_2 isomers calculated at the DFT / B3LYP level. The atomic labels are the same as those in Figure 6.3

	La-η^2-HCCH		**La-$CCCH_2$**	
ES	**$^2A_1$**	**$^1A_1$**	**$^2A_1$**	**$^1A_1$**
E_0	0	41908	6923	49293
La-C_2	2.31	2.25	2.14	2.08
C_1-C_2	1.35	1.35	1.33	1.34
La-C_1-C_2	73	73	180	180

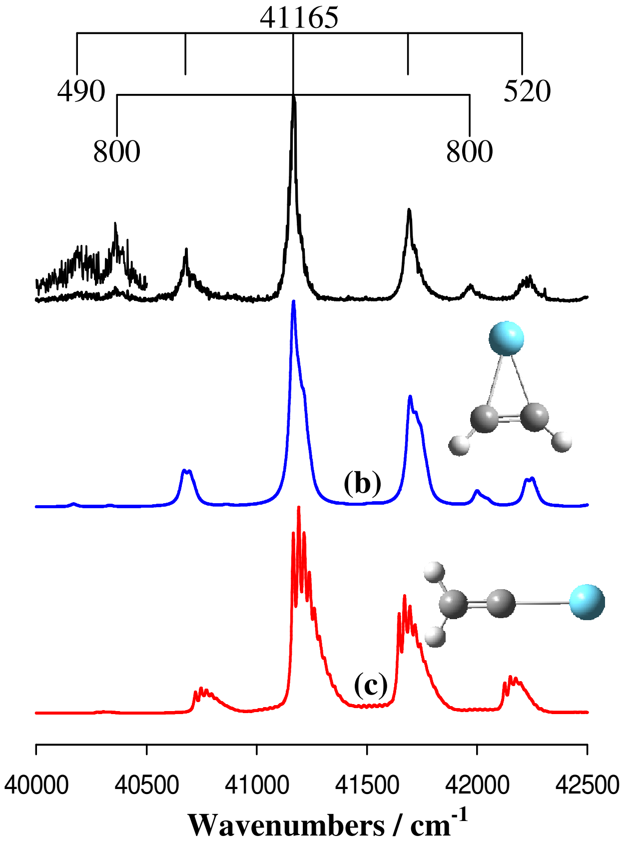

Figure 6.4 MATI spectrum of LaC_2H_2 (a) and the simulated spectra of the $^1A_1 \leftarrow {}^2A_1$ transition of La-η^2-HCCH at 800K (b) and the $^1A_1 \leftarrow {}^2A_1$ transition of La-η^1-CCH_2 at 400K (c) with a FWHM of 35 cm^{-1}.

6.3.2 LaC_4H_4

The first sharp onset of the PIE spectrum of LaC_4H_4 is at 41000 (20) cm^{-1} as shown in Figure 6.2(c). This onset nicely matches with the strongest peak at 41000 (5) cm^{-1} in the MATI spectrum of LaC_4H_4 in Figure 6.4(a). The MATI spectrum exhibits a short progression of 380 $cm^{-1}$and 316, 528, 616 and 900 cm^{-1} intervals above the origin band. In order to analyze and assign the spectrum in details, we have searched for possible structural isomers of LaC_4H_4. LaC_4H_4 is the metal bound dehydrogenated product of 1,3-butadiene. The dehydrogenation can occur at different C sites of 1,3-butadiene, and the metal complex may undergo rearrangements before or after the dehydrogenation to generate different isomers of LaC_4H_4. Four low energy isomers of LaC_4H_4 are presented in Figure 6.6. Isomer A is formed by 2,2-dehydrogenation and C by 1,4-dehydrogenation, and B and D are formed by 1,2-dehyderogenation (Figure 6.6). The ground state of each isomer is expected to be in a doublet spin state according to our past experience. Indeed, the $^2A_1$ ground state is predicted for isomer A (C_{2v}), ^2A for isomer B (C_1), $^2A_1$ for isomer C (C_{2v}), and $^2A'$ for isomer D (C_s) (Table 6.2). The most stable isomer is predicted to be isomer A, followed by B at 1250 cm^{-1} (0.15eV), C at 3065 cm^{-1} (0.38eV), and D at 4640 cm^{-1} (0.58eV). The major structural change in each isomer upon ionization is the reduction of the La-C bond lengths (Table 6.2). Among all isomers, isomer C undergoes the largest structural changes induced by ionization, including the reduction of the La-C bond lengths and the expansion of the C_1-La-C_4 bond angle.

Figure 6.3 compares the observed MATI spectrum with the simulated spectra of all four isomers. Figure 6.3(b) displays the simulated spectrum of the $^1A_1 \leftarrow ^2A_1$ transition of isomer A. Even though the predicted intensity profile is similar to the observed one, the predicted vibrational interval (326 cm^{-1}) of the major progression is smaller than the measured one (380 cm^{-1}). Moreover, the theoretical IE (42583 cm^{-1}) of this transition is considerably higher than the observed IE (41000 cm^{-1}). On the other hand, the simulation of the $^1A \leftarrow {}^2A$ transition of isomer B matches nicely with the experimental spectrum in both vibrational intervals and spectral intensity profile. The theoretical IE of this transition (41658 cm^{-1}) also agree reasonably well with the observed IE. The $^1A_1 \leftarrow {}^2A_1$ transition of isomer C as shown in Figure 6.3(d) has a long spectral profile as we can expect due to its significant structural change upon ionization, which does not resemble the experimental spectrum at all. The $^1A' \leftarrow {}^2A'$ transition of isomer D as shown in Figure 6.3(e) exhibits a short spectral profile as the experimental spectrum However, the predicted vibrational interval of the main progression (565 cm^{-1}) is much larger than the observed one. Therefore, among the four isomers, isomer B is a very likely carrier for the observed MATI spectrum. The observed major progression of 380 cm^{-1} is assigned to the La-hydrocarbon stretching, the 316 cm^{-1} interval to the La-C_1 and La-C_4 stretching,. the 528 cm^{-1} interval to the terminal H rocking , the 616 cm^{-1} interval to the C skeleton bending mixed with the H twisting motion, and the 900 cm^{-1} interval to the H wagging motion. All of these vibrational modes are for the ^1A ion state of isomer B.

Our group has also investigated La reactions with 1-butyne and 2-butyen and observed LaC_4H_4 from these two reactions. Figure 6.7 compares the MATI spectra of LaC_4H_4 formed by the La reactions with 1,3-butadiene, 1-butyne, and 2-butyen. The three spectra are very similar except the relative intensities of several small bands are different. For example, the intensity of the 2 x 386 cm^{-1} band is much stronger than that of the 900 cm^{-1} band in the spectrum of LaC_4H_4 formed by the 1,3-butadiene reaction (Figure 6.7a), while the intensities of these two bands are comparable in the spectra of LaC_4H_4 formed by the 1- and 2-butyne reactions (Figure 6.7 (b,c)). For the 1- and 2-butyne reactions, two isomers (isomers A and B) are identified for LaC_4H_4, as shown in Figure 6.7d. The band of isomer B at the 900 cm^{-1} interval overlaps with the origin band of isomer A. Since the intensity of the 900 cm^{-1} band in Figure 6.7a is week, we are not certain if isomer A is also formed in the 1,3-butadiene reaction. On the other hand, we are not able to exclude the formation of isomer A in the butadiene reaction as well because many bands from isomers A and B are overlapped to each other.

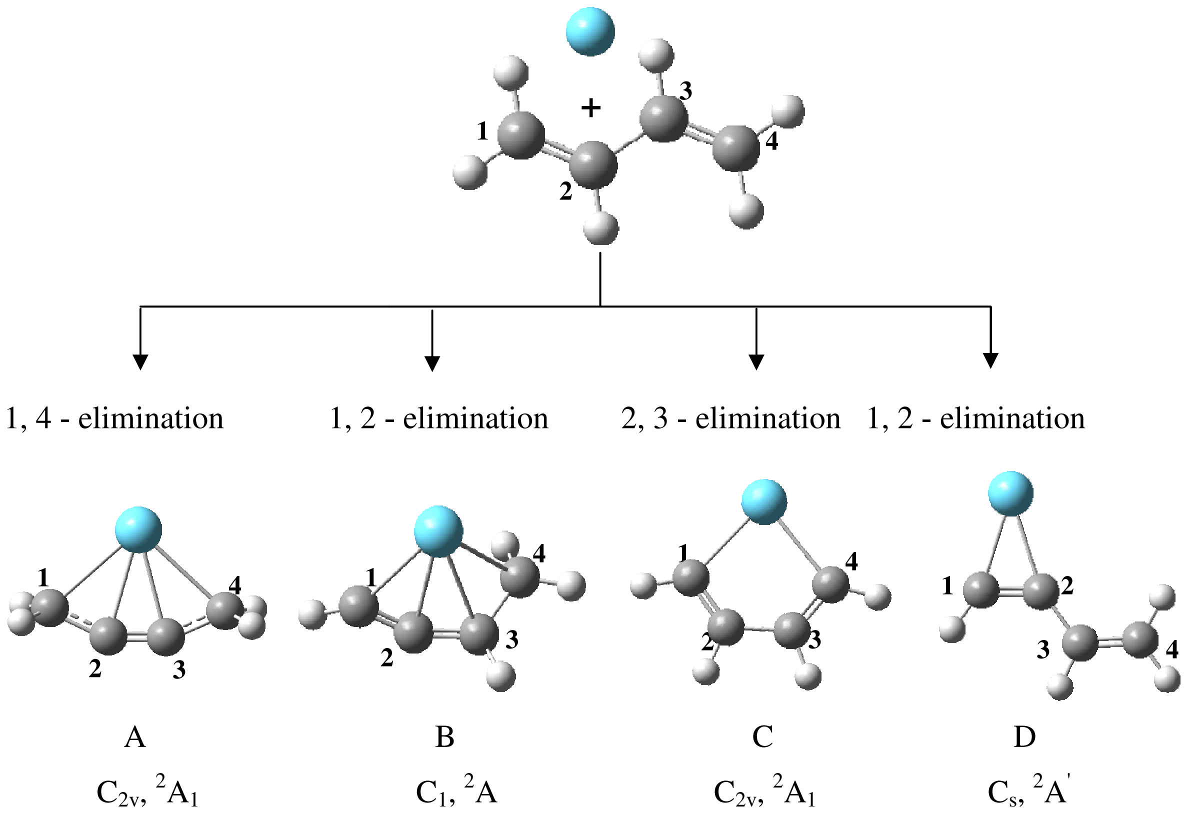

Figure 6.5 Isomers of LaC_4H_4 produced by the La mediated H elimination of 1,3-butadine. The point groups and electronic states of the isomers are listed below the structures.

Table 6.2 Electronic states (**ES**), relative energies including vibrational zero point corrections (**E_0**, cm^{-1}), and bond lengths (Å) and angles (degrees) of the LaC_4H_4 isomers calculated at the DFT / B3LYP level. The atomic labels are the same as those in Figure 3.3

	Isomer A		Isomer B		Isomer C		Isomer D	
ES	$^2A_1$	$^1A_1$	^2A	^1A	$^2A_1$	$^1A_1$	$^2A'$	$^1A'$
E_0	0	42583	1250	41658	3065	40690	4640	41400
La-C_1	2.60	2.54	2.47	2.41	2.39	2.30	2.30	2.23
La-C_2	2.45	2.40	2.49	2.44	2.96	2.78	2.33	2.28
La-C_3	2.45	2.40	2.58	2.53	2.96	2.78		
La-C_4	2.60	2.54	2.57	2.52	2.39	2.30		
C_1-C_2	1.42	1.41	1.30	1.30	1.36	1.37	1.35	1.36
C_2-C_3	1.25	1.25	1.36	1.36	1.49	1.50	1.46	1.45
C_3-C_4	1.42	1.41	1.45	1.45	1.36	1.37	1.34	1.34
< C_1-La-C_2	32	33	30	31			34	35
< C_1-La-C_4	94	96	87	88	83	90		
< C_1-C_2- C_3-C_4	0	0	57	55	0	0	0	0

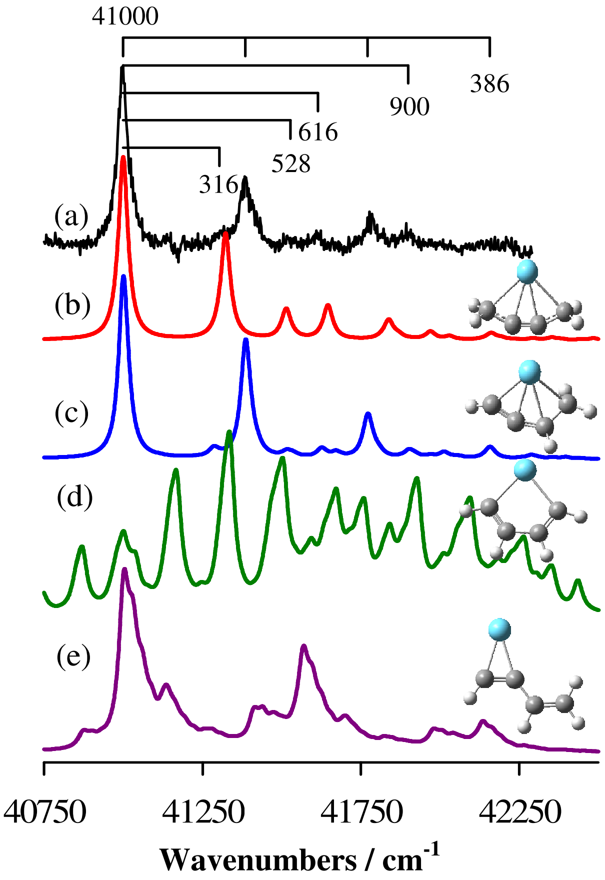

Figure 6.6 MATI spectrum of LaC_4H_4 (a) and the simulated spectra of the $^1A \leftarrow {}^2A$ transition of isomer A (b), the $^1A \leftarrow {}^2A$ transition of isomer B (c), the $^1A_1 \leftarrow {}^2A_1$ transition of isomer C (d) and the $^1A' \leftarrow {}^2A'$ transition of isomer D of LaC_4H_4 at 200K with FWHM of 30 cm^{-1}.

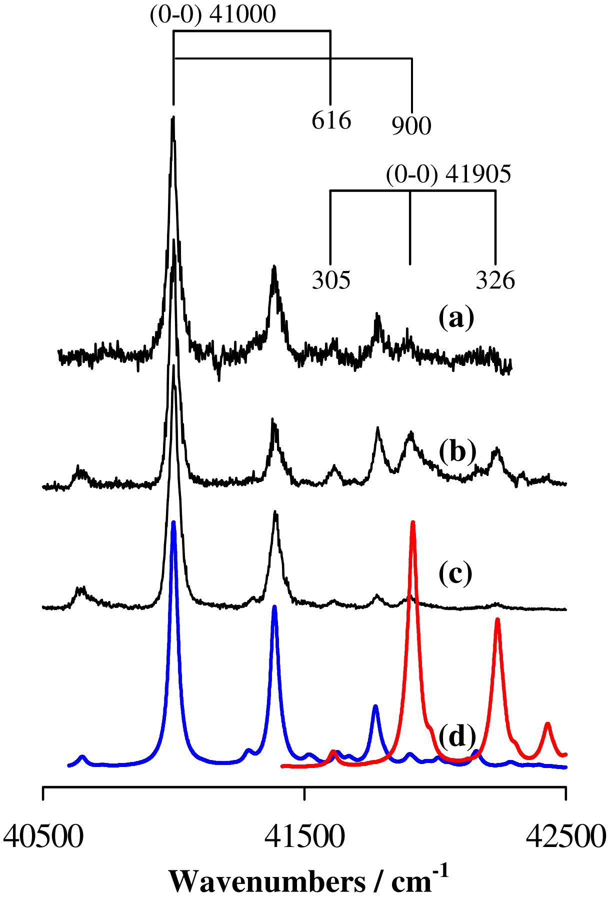

Figure 6.7 MATI spectra of LaC_4H_4 formed in the reactions: La + 1,3-butadine (a), La + 1-butyne (b) and La + 2-butyne (c) and the simulated spectra of LaC_4H_4: $^1A \leftarrow ^2A$ transition of isomer B (d-blue trace) and $^1A_1 \leftarrow ^2A_1$ transition of isomer A (d-red trace).

6.3.3 LaC_4H_6

The approximate first ionization energy of LaC_4H_6 is measured to 39400 (50) cm^{-1} from the PIE spectrum in Figure 6.2(b). This energy is used to help the search for the MATI signal. The origin band of LaC_4H_6 is measured at 39420 cm^{-1}, about 1600 cm^{-1} lower than that of LaC_4H_4. Moreover, although the spectra of both LaC_4H_6 and LaC_4H_4 display a short spectral profile, the spectrum of LaC_4H_6 (Figure 6.8(a)) exhibits rather different vibrational intervals from the spectrum of LaC_4H_4 (Figure 6.6(a)). The spectrum of LaC_4H_6 shows a 398 cm^{-1} major progression, 26 cm^{-1} sequence bands superimposed on the main progression, and two additional bands at 320 and 470 cm^{-1} above the origin band. In addition, two combination bands (not labelled in the figure) are observed at (400 + 320) and (400 + 470) cm^{-1}. Below the origin band, two weak bands at 285 and 370 cm^{-1} are observed.

LaC_4H_6 is formed by the simple association of La with butadiene. There are two possible isomers for the LaC_4H_6 adduct, and they are 1-lathana-3-cyclopentene and La-(1,3-butadiene, s-trans). The structures of two isomers are presented alone with their simulations in Figure 6.8. In the reaction of La + propene, we have also obtained the same MATI spectrum (Figure 5.9) as the one in Figure 6.8(a), and identified 1-lathana-3-cyclopentene (isomer B labeled in Chapter 5) as the carrier of MATI spectrum. The geometries of doublet and quartet spin states of this isomer have already been presented in Table 5.2 in Chapter 5. The observed and predicted IEs and vibrational frequencies of 1-lathana-3-cyclopentene with their isotopic shifts have been presented in Table 5.3 in Chapter 5. However, Table 6.3 also presents the observed and predicted IEs and vibrational frequencies of this isomer. The 26 cm^{-1} sequence bands are attributed to sequence transitions between the excited in-plane carbon skeleton bending mixed with the hydrogen wagging vibration levels of neutral and cation electronic states. The

320 cm^{-1} interval is due to the vibrational excitation of an out of plane ring bending mixed with a central H wagging motion of the cation complex and 285 cm^{-1} is the same vibrational mode of the neutral state. The 370 and 398 cm^{-1} vibrational intervals are related to an in-plane carbon skeleton bending mixed with a H rocking and a La-hydrocarbon stretching motion of the neutral and cation states, respectively. The 470 cm^{-1} interval is related to a H twisting motion of the cation.

The metal-butadiene binding in condensed-phase transition metal complexes has previously been studied based on their crystal structures and has been divided into σ^2,π-metallacyclopentene and π^2 modes as shown in Figure 6.9.[206,207] In the σ^2,π-binding mode, a metal atom or ion is strongly bound with the terminal C_1 and C_4 atoms than with the internal C_2 and C_3 atoms. This binding mode results in a shorter C_2-C_3 bond than either C_1-C_2 or C_3-C_4. This geometric feature of C_4H_6 in the metal complexes is in clear contrast with that of the free ligand, where the C_2-C_3 bond is longer than the C_1-C_2 and C_3-C_4 bonds. On the other hand, a metal atom or ion is strongly bound with the internal C_2 and C_3 atoms than the terminal C_1 and C_4 atoms in the π^2-binding mode. In this case, the C_2-C_3 bond is longer than the C_1-C_4 and C_3-C_4 bonds as in the free ligand. For the 1-lathana-3-cyclopentene isomer of LaC_4H_6, we find that it is a σ^2,π-metallacyclopentene complex.

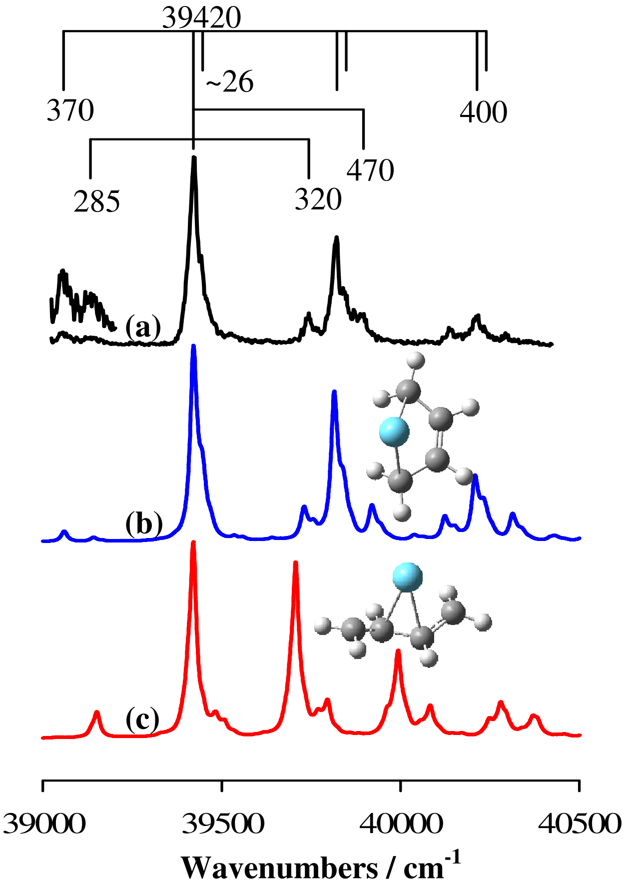

Figure 6.8 MATI spectrum of LaC_4H_6 (a) and the simulated spectra of the $^1A' \leftarrow {}^2A'$ transition of 1-lathana-3-cyclopentene (b) and the $^1A \leftarrow {}^2A$ transition of La-(1,3-butadiene, s-trans) (c). The simulations are performed at 200K with FWHM of 20 cm^{-1}.

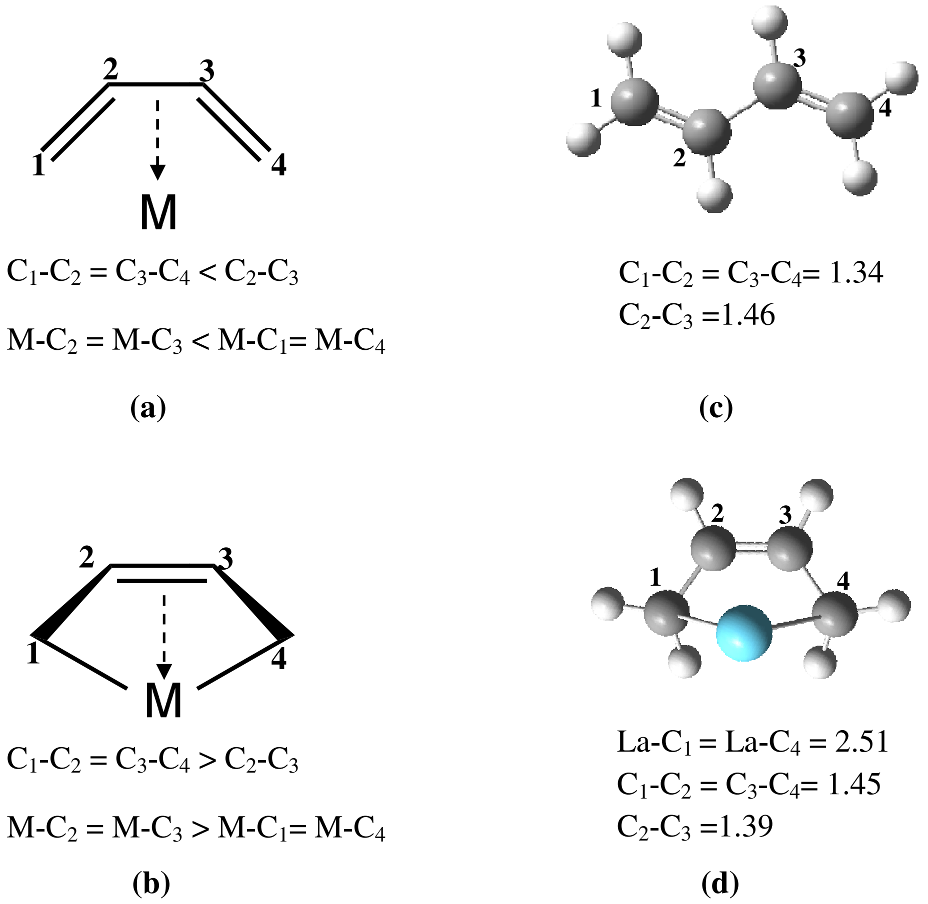

$C_1\text{-}C_2 = C_3\text{-}C_4 < C_2\text{-}C_3$

$M\text{-}C_2 = M\text{-}C_3 < M\text{-}C_1 = M\text{-}C_4$

(a)

$C_1\text{-}C_2 = C_3\text{-}C_4 = 1.34$
$C_2\text{-}C_3 = 1.46$

(c)

$C_1\text{-}C_2 = C_3\text{-}C_4 > C_2\text{-}C_3$

$M\text{-}C_2 = M\text{-}C_3 > M\text{-}C_1 = M\text{-}C_4$

(b)

$La\text{-}C_1 = La\text{-}C_4 = 2.51$
$C_1\text{-}C_2 = C_3\text{-}C_4 = 1.45$
$C_2\text{-}C_3 = 1.39$

(d)

Figure 6.9 π^2 model (a), σ^2, π-metallacyclopentene model (b), 1,3-butadiene (c) and 1-lanthana-3-cyclopentene (d). Bond lengths (Å) of 1,3-butadiene and 1-lanthana-3-cyclopentene are listed below the structures.

6.3.4 LaC_6H_6

The PIE spectrum of LaC_6H_6 (Figure 6.2(d)) displays its first sharp onset at 36785 (50) cm^{-1}. Comparable to the sharp onset, the MATI spectrum of LaC_6H_6 in Figure 6.10(a) shows the origin band at 36820 (5) cm^{-1}. The position of the origin band corresponds to the IE of LaC_6H_6, which is significantly lower than the IEs of the other three complexes presented in this chapter.. The MATI spectrum exhibits a 295 cm^{-1} major progression, sequence bands separated from the main progression by 39 cm^{-1} (or 39 x 2 cm^{-1}), and two additional bands at 152 and 527 cm^{-1} above the origin band. This MATI spectrum is very similar to the ZEKE spectrum of the La-benzene complex reported by our research group,[136] except the MATI spectrum is broader and noisier than the ZEKE spectrum (Figure 6.10(b)). Therefore, The LaC_6H_6 complex formed in the La + 1,3-butadiene must be La-benzene. The observation of the La-benzene formation is fascinating, and its formation will be discussed later in this chapter. In the ground state of the complex, La is bound to the benzene ring in a η^2 binding mode, and the benzene ring is bent. As a result, the La-benzene complex has C_{2v} symmetry, rather than C_{6v} as one normally assumes for a M-benzene species. The simulation of the $^1A_1 \leftarrow {}^2A_1$ electronic transition of La-benzene (Figure 6.10(c)) matches well with the experimental MATI spectrum. The 295 cm^{-1} major progression arises from the La-benzene symmetric stretching motion of the cation. The 527 cm^{-1} interval is from the C–H wagging mixed with an in-plane ring deformation of the cation. The 39 cm^{-1} sequence bands arise from the ring rocking along the y-axis of the complex. However, the weak band at 152 cm^{-1} is not produced by the simulation. The rest of the transitions are the combination bands arising from excitations of two or more vibrational modes. Further details of this molecule with MP2 level calculations can be found in the previous work.[136]

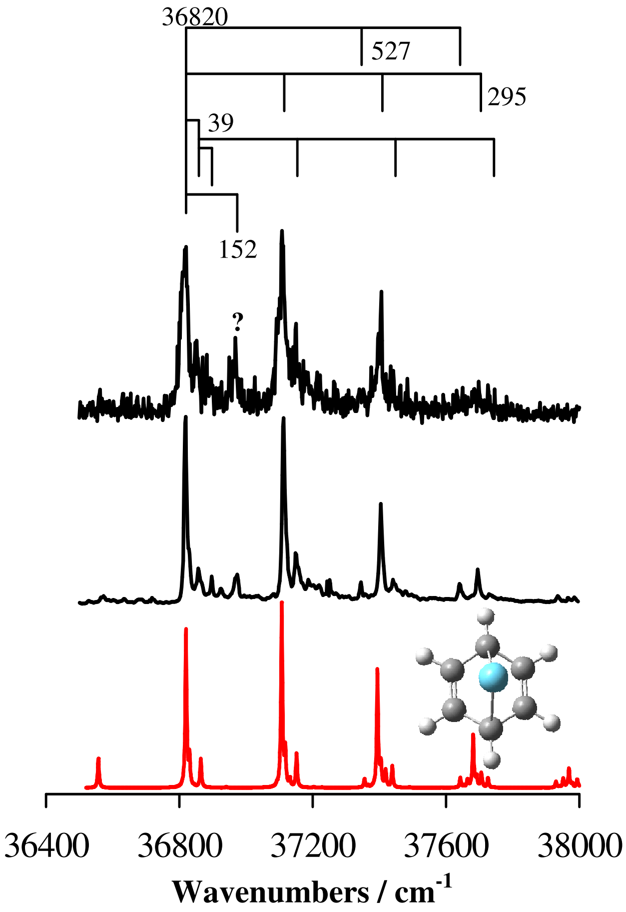

Figure 6.10 MATI spectrum of LaC$_6$H$_6$ (a), ZEKE spectrum of La-benzene (b), and the simulated spectrum of the $^1A_1 \leftarrow {}^2A_1$ transition of La-benzene (c) at 200K with a FWHM of 5 cm^{-1}.

Table 6.3 Adiabatic ionization energies (AIE, cm^{-1}) and vibrational frequencies (cm^{-1}) of La-η^2-HCCH, 1-lathana-3-cyclopetene, and La-benzene from MATI measurements and DFT / B3LYP calculations. The associated error in experimental IEs is 5 cm^{-1}

	Experiment	Theory
La-η^2-HCCH		
AIE : $^1A_1 \leftarrow {}^2A_1$	41165	41908
La-hydrocarbon symmetric stretching of neutral, υ_4	490	471
La-hydrocarbon symmetric stretching of cation, υ_4^+	520	528
H scissoring of neutral, υ_3	800	833
H scissoring of cation, υ_3^+	800	833
LaC_4H_4 - isomer B		
AIE : $^1A \leftarrow {}^2A$	41000	41658
La-hydrocarbon asymmetric stretching of cation, υ_{20}^+	316	284
La-hydrocarbon asymmetric stretching with H bending of cation, υ_{19}^+	380	373
Terminal H rocking of cation, υ_{17}^+	528	516
Bending of C skeleton and H twisting of cation, υ_{15}^+	616	626
H wagging of cation, υ_{12}^+	900	900
1-lathana-3-cyclopentene		
AIE : $^1A' \leftarrow {}^2A'$	39414	40178
In plane C skeleton bending, terminal and central H wagging (υ_{14}^+ - υ_{14})	~26	24
Central H wagging with small La- hydrocarbon stretching of neutral, υ_{13}	285	280
Central H wagging with small La- hydrocarbon stretching of cation, υ_{13}^+	320	310
In-plane C skeleton bending, terminal H twisting of neutral, υ_{12}	370	360
In-plane C skeleton bending, terminal H twisting of cation, υ_{12}^+	398	391
H twisting, υ_{11}^+	470	492
La-benzene		
AIE : $^1A_1 \leftarrow {}^2A_1$	36820	37273, 36391[a]
La- hydrocarbon symmetric stretching, υ_{10}^+	295	287, 303[a]
C–H wagging and in plane ring deformation, υ_8^+	527	535, 539[a]
Ring rocking along y-axis, (v_{24}^+- v_{24})	39	50, 35[a]

[a] Reference 136, Calculations done at MP2 level

Table 6.4 MATI band positions (MBP, cm^{-1}) and assignments of La-η^2-HCCH, LaC_4H_4 (isomer B), 1-lanthana-3-cyclopetene and La-benzene. The uncertainty associated with the band positions is 5 cm^{-1}

La-η^2-HCCH		LaC_4H_4 (isomer B)		1-lanthana-3-cyclopentene		La-benzene	
MBP	Assign.	MBP	Assign.	MBP	Assign.	MBP	Assign.
40365	3^0_1	41000	0^0_0	39044	24^0_1	36820	0^0_0
40675	4^0_1	41316	20^1_0	39134	25^0_1	36859	24^1_1
41165	0^0_0	41386	18^1_0	39404	0^0_0	36898	24^2_2
41685	4^1_0	41528	17^1_0	39724	25^1_0	37115	10^1_0
41965	3^1_o	41616	15^1_0	39815	24^1_0	37154	$10^1_0 24^1_1$
42205	4^2_0	41772	18^2_0	39877	22^1_0	37193	$10^1_0 24^2_2$
		41900	12^1_0	40124	$24^1_0 25^1_0$	37347	8^1_0
		42158	18^3_0	40204	24^2_0	37410	10^2_0
				40274	$22^1_0 24^1_0$	37449	$10^2_0 24^1_1$
						37642	$8^1_0 10^1_0$
						37705	10^3_0

6.3.5 Reaction Pathways for the Formation of LaC_2H_2, LaC_4H_4, LaC_4H_6 and LaC_6H_6

$La + CH_2{=}CHCH{=}CH_2 \rightarrow LaC_2H_2 + CH_2{=}CH_2$

$La + CH_2{=}CHCH{=}CH_2 \rightarrow LaC_4H_4 + H_2$

$La + CH_2{=}CHCH{=}CH_2 \rightarrow LaC_4H_6$

$LaC_2H_2 + CH_2{=}CHCH{=}CH_2 \rightarrow LaC_6H_6 + H_2$

LaC_2H_2, LaC_4H_4 and LaC_4H_6 are the primary products, and LaC_6H_6 is a secondary product of the reaction. The reaction pathways for the formation of all four products are discussed here. The atomic labels used in the discussion are the same as those in Figure 6.9. Figure 6.11 presents the predicted reaction pathway of the LaC_4H_4 formation. LaC_4H_6 is found as an intermediate along the pathway of the LaC_4H_4 formation. In the initial step, La metal binds to C_2 and C_3 atoms of butadiene to form IM1, La-(1,3-butadiene,s-trans). The La-(1,3-butadiene) association complex rearranges via TS1 to form IM2 (1-lanthana-3-cyclopentene), which is experimentally identified (see section 6.3.3). La then activates the C_3-H bond via TS2 to form IM3, an insertion intermediate. The H atom in La-H of IM3 rotates anti-clockwise via TS3 to form IM4. The La-C_3 bond is stronger, but the La-C_1 and La-C_4 bonds are weaker in IM4 than the corresponding bonds in IM3. In the final step, the C_2-H bond is activated, and the concerted elimination of a H_2 molecule occurs via TS4 to form isomer A. In the formation of isomer B, La inserts into the C_2-H bond to form IM5 via TS6. Then, the La-H bond in IM5 rotates clockwise via TS6 to form IM6. In the final step, the C_1-H bond activation is followed by the concerted H_2 elimination to form isomer B. Since the energy barrier for the H_2 elimination is much higher in the formation of isomer A (TS4) than that of isomer B (TS7), the reaction produces much less isomer A than B. The reaction pathway of the LaC_2H_2 formation starting from LaC_4H_6 is shown in Figure 6.12. In the initial step, La of LaC_4H_6 activates C_2-H bond to form the insertion product IM7 via TS8. H atom in IM7 rotates clockwise as in TS9 or anticlockwise as in TS12 to form IM8. This H then migrates to C_3 carbon to form IM9 via TS10. Finally C_2-C_3 bond dissociates to form LaC_2H_2 and C_2H_4.

Figure 6.13 presents the reaction pathway of the LaC_6H_6 formation. Initially, LaC_2H_2 interacts with a second butadiene molecule to form an adduct, IM7. The adduct formation has no energy barrier. Following the adduct formation, an intramolecular C-C coupling reaction forms IM8 via TS8, and a cyclization reaction of IM8 yields IM9 via TS9, LaC_6H_8. The La-benzene complex is then formed by the metal insertion in to a C-H bond and H_2 elimination (i.e., IM9 → TS10 →IM10 →TS11 →La-benzene + H_2). Our predicted reaction pathway is comparable with a qualitative reaction pathway proposed by Schwarz et al. for the reactions of M^+ (M=Cr, Mn, Fe and Co) with acetylene and butadiene to form M^+-benzene.

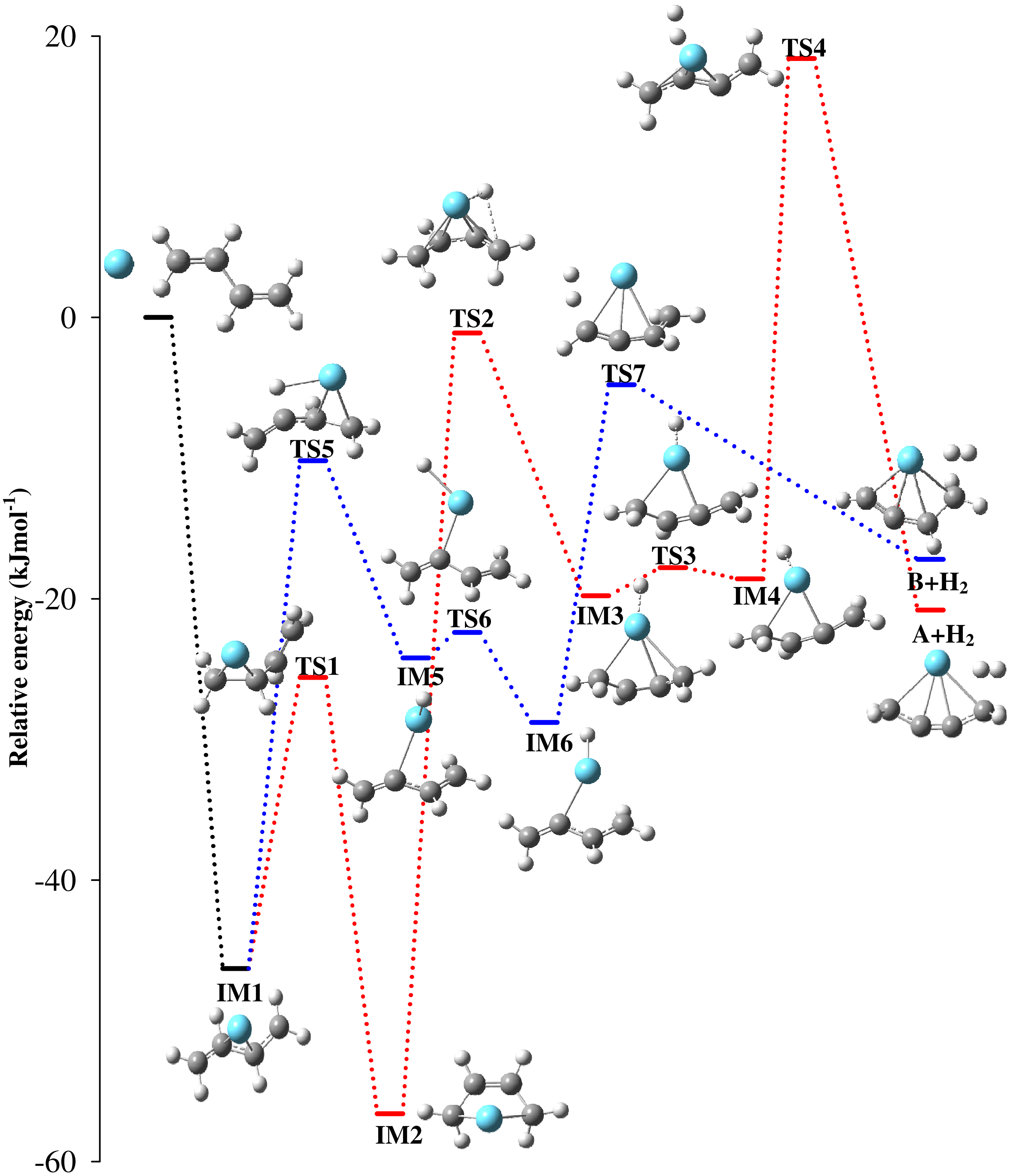

Figure 6.11 Reaction pathway for the formation of LaC_4H_6 and LaC_4H_4 from the reaction between La and $CH_2=CHCH=CH_2$ calculated at the DFT/B3LYP level. TS: Transition States, IM: Intermediates.

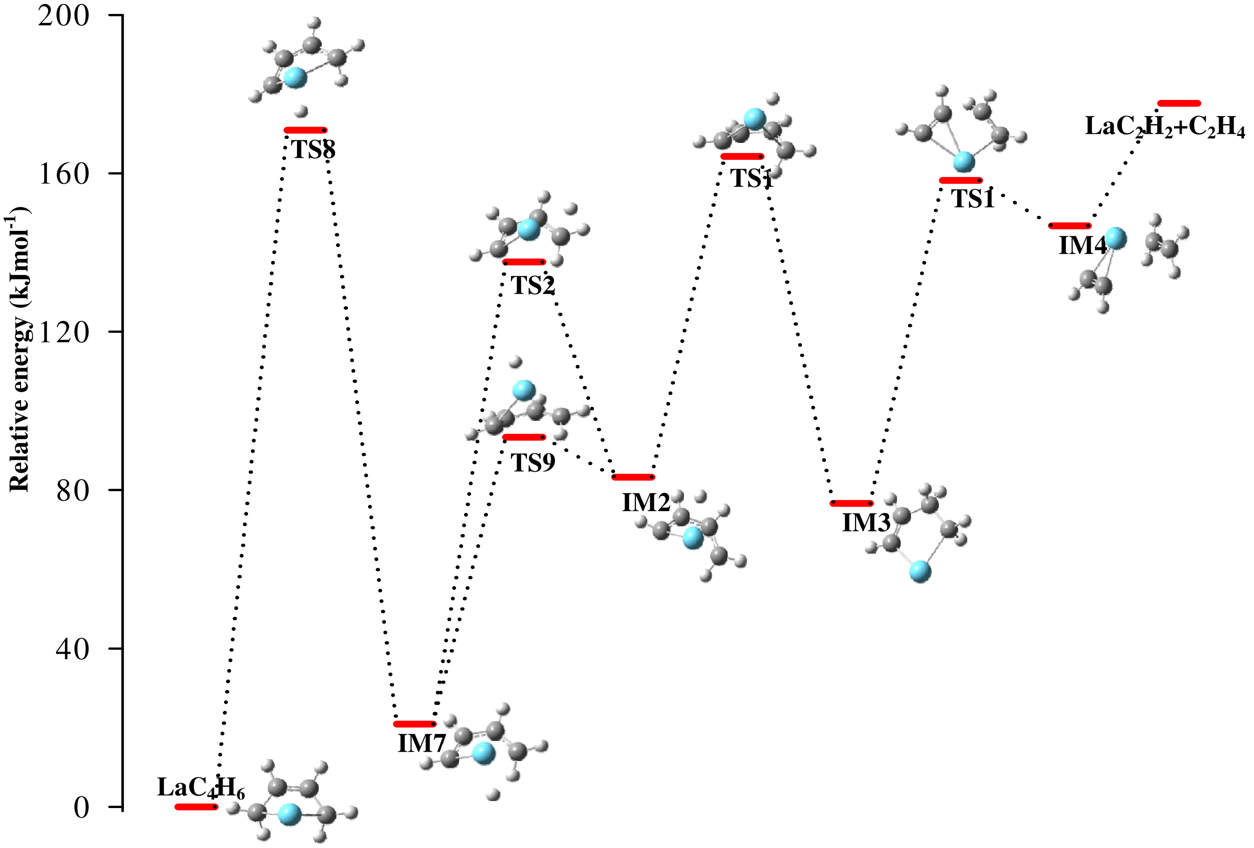

Figure 6.12 Reaction pathway for the formation of LaC_2H_2 starting from LaC_4H_6 calculated at the DFT/B3LYP level. TS: Transition States, IM: Intermediates.

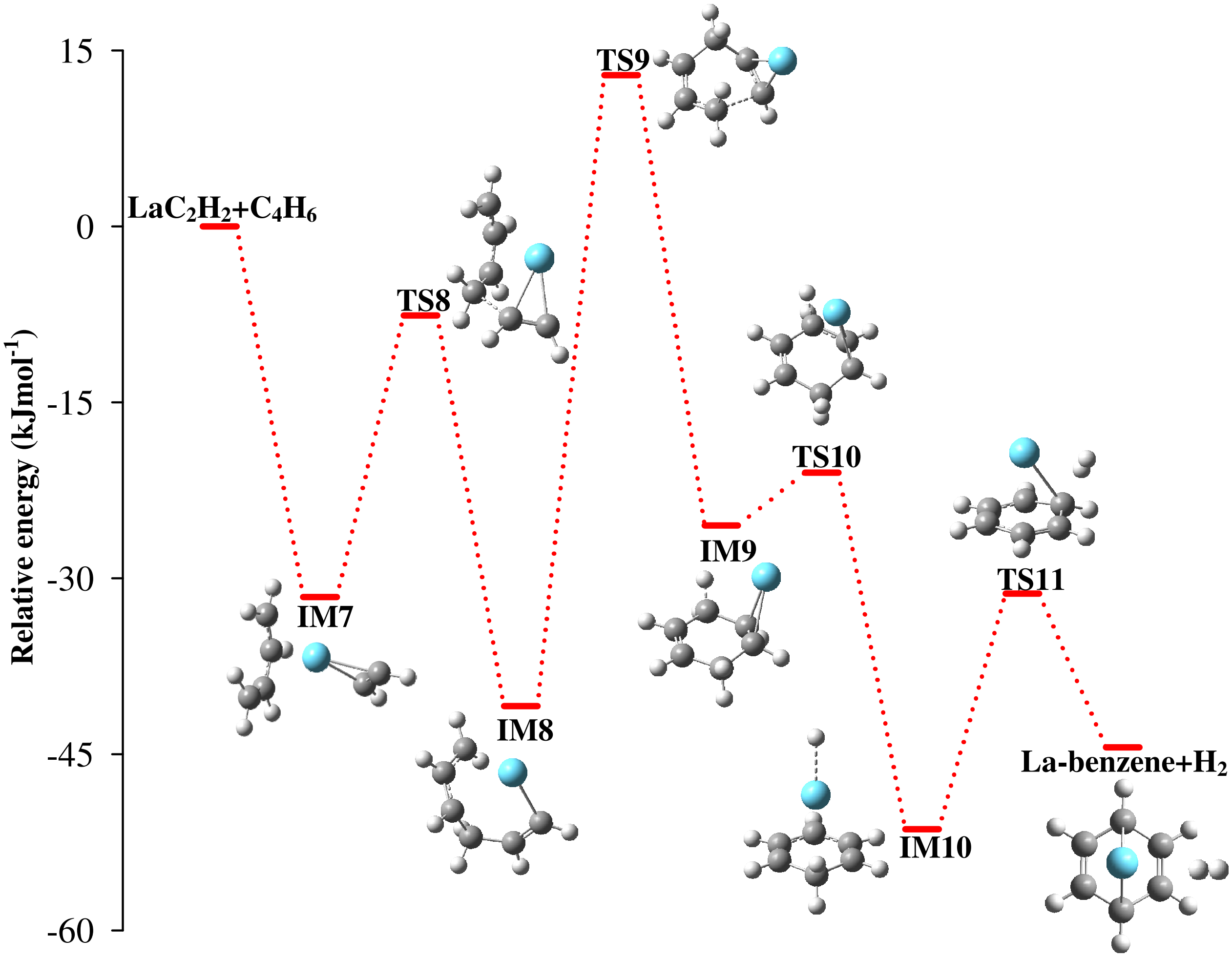

Figure 6.13 Reaction pathway for the formation of LaC_6H_6 from the reaction between LaC_2H_2 and CH_2=CHCH=CH_2 calculated at the DFT/B3LYP level. TS: Transition States, IM: Intermediates.

6.4 Conclusions

La atom mediated C-C and C-H bonds activation and C-C bond coupling of butadiene were observed in the La + 1,3-butadiene molecular beam. Structures, electronic states and AIEs of LaC_2H_2, LaC_4H_4, LaC_4H_6 and LaC_6H_6 were determined using the MATI spectroscopic measurements. The reaction pathways for formations of the above products, but LaC_2H_2) were predicted by the DFT calculations. LaC_2H_2 exists as the La-η^2-HCCH isomer, which is formed by the C_2-C_3 bond activation and 1,3-H shift of butadiene. This isomer has C_{2v} symmetry with the $^2A_1$ neutral ground electronic state The major isomer of LaC_4H_4 was identified as isomer B. This isomer has C_1 symmetry with the ^2A ground electronic state and is formed by 1,2-hydrogen elimination of butadiene. LaC_4H_6 was identified as 1-lanthana-3-cyclopentene, a σ^2,π-metallacyclopentene. 1-lanthana-3-cyclopentene has C_s symmetry with the $^2A'$ neutral ground electronic state. LaC_6H_6 was identified as La-benzene in the $^2A_1$ (C_{2v}) neutral ground state. La-benzene is formed by a secondary reaction of LaC_2H_2 with a butadiene molecule. In each of the complexes, the MATI spectrum exhibits the strong Franck-Condon activity of the La-hydrocarbon stretching vibration.

CHAPTER 7. LANTHANUM ATOM MEDIATED BOND ACTIVATION OF 1-BUTENE

7.1 Introduction

We have studied the La atom-mediated bond activation of a series of small hydrocarbons, including both alkenes and alkynes as discussed in Chapters 3, 4, 5 and 6. The work presented in this chapter is the continuation of the project by expanding the research on the reaction between 1-butene and La atom. Transition metal-mediated bond activation of 1-butene and other butene isomers has been considerably studied in both condensed and gas phases due to their academic and commercial importance.[167,168,189,191,208-215] Gas phase studies have mainly focused on the reactivity patterns and potential energy surfaces of the metal-mediated bond activation.[189,191,210] Castleman et al. have investigated the structure-reactivity relationship of metal oxide clusters (Ta_xO_y, V_xO_y) using 1-butene.[189,191] For most of the clusters they investigated, C_2-C_3 bond cleavage of 1-butene has been observed as the major bond activation. Davis et al. have investigated the competition between Y metal mediated C-C and C-H bond activation of four butene isomers including 1-butene.[210] They have observed YC_4H_6 and YH_2 by the C-H bond activation and YCH_2 by the C-C bond activation. Existence of a higher energy barrier for the C-C bond activation than for the C-H bond activation has been confirmed by their study. However, the structures and electronic states of the bond activated metal complexes have not been investigated as their work focused on the reaction dynamics.

In the present work, we report the lowest energy isomer of LaC_2H_2 and two low-energy isomers of LaC_4H_6 from the La+1-butene reaction. To our knowledge, this work is the first spectroscopic identification of the structural isomers for these complexes formed by the C-H bond activation of 1-butene.

7.2 Experimetal and Computational Details

The metal-cluster beam instrument used in this work consists of the reaction and spectroscopy vacuum chambers and was described in Chapter 2. The metal-hydrocarbon reaction was carried out in a laser vaporization metal cluster beam source. 1-butene (95% , GFS Chemicals) was seeded in a He carrier gas with a concentration of 10^{-4} - 10^{-5} in a stainless steel mixing cylinder. La metal atoms were generated by pulsed-laser (Nd:YAG, Continuum Minilite II, 535 nm, 1.0-1.5 mJ/pulse) vaporization of a La rod (99.9%, Alfa Aesar) in the presence of the hydrocarbon/He mixture (40 psi) delivered by a home-made piezoelectric pulsed valve. The metal atoms and gas mixture entered into a clustering tube (2 mm diameter and 2 cm length) where chemical reaction occurred. The reaction mixture was then expanded into the reaction chamber, collimated by a cone-shaped skimmer (2 mm inner diameter), and passed through a pair of deflection plates. Ionic species in the molecular beam that were formed during laser vaporization were removed by the electric field (100 Vcm^{-1}) applied on the deflection plates. The neutral products were identified by photoionization time-of-flight mass spectrometry.

Prior to the MATI measurements, photoionization efficiency spectra were recorded to locate the approximate ionization thresholds of the La-hydrocarbon complexes formed in the reaction to simplify the MATI experiment. In the MATI experiment, the complexes were excited to high-lying Rydberg states in a single-photon process and ionized by a delayed pulsed electric field. The excitation laser was the same as that for photoionization in the mass spectrometry and photoionization efficiency experiments and was the frequency doubled output of a tunable dye laser (Lumonics HD-500), pumped by the third harmonic output (355 nm) of a Nd:YAG laser (Continuum Surelite II). The laser beam was collinear and counter propagating with the molecular beam. The ionization pulsed field (320 V cm^{-1}) was generated by two high voltage pulse generators (DEI, PVX-4140) and delayed by 10-20 μs from the laser pulse by a delayed pulsed generator (SRS, DG641). A small DC field (6.0 V cm^{-1}) was applied to separate the prompt ions produced by direct photoionization from the MATI ions generated by delayed field ionization. The MATI ion signal was obtained by scanning the wavelength of the tunable dye laser, detected by a dual microchannel plate detector, amplified by a preamplifier (SRS, SR445), averaged by a gated integrator (SRS, SR280), visualized by a digital oscilloscope (Tektronix TDS 3012), and stored in a laboratory computer. Laser wavelengths were calibrated against vanadium atomic transitions in the spectral region.[129] The Stark shift induced by the DC separation field was calculated using the relation of $\Delta IE = 6.1E_f^{1/2}$, where E_f is in V cm^{-1} and ΔE is in cm^{-1}.[130]

Geometry optimization and vibrational frequency calculations were carried out using Gaussian 03 software package.[92] In these calculations we used the Becke's three-parameter hybrid functional with the correlation functional of Lee, Yang, and Parr (B3LYP)[82,83] and 6-311+G(d,p)[93,94] basis set for C and H and effective-core-potential SDD[95] basis set for La. We have extensively used DFT/B3LYP and found this method generally produced adequate results for helping the spectral and structural assignments of organometallic radicals.[131] No symmetry restrictions were imposed in initial geometry optimizations. However, geometry re-optimizations with appropriate point groups were carried out to identify the electronic states. For each optimized stationary point, vibrational analysis was performed to identify the nature of the stationary point (minimum or saddle point).

To compare with the experimental MATI spectra, multi-dimensional FC factors were calculated from the equilibrium geometries, harmonic vibrational frequencies, and normal coordinates of the neutral and ionized complexes.[132] In these calculations, the recursion relations from Doktorov et al.[133] were employed, and the Duschinsky effect[99] was considered to account for a possible axis rotation from the neutral complex to the cation. Spectral simulations were obtained using the experimental linewidth and a Lorentzian line shape. Transitions from excited vibrational levels of the neutral complex were considered by assuming thermal excitation at specific temperatures.

7.3 Results and discussion

The observed La-complexes in the reaction are LaC_2H_2, LaC_5H_{12}, LaC_4H_6 and LaC_8H_{14} as shown in Figure 7.1. The structure of LaC_2H_2 is characterized by the MATI measurement and is the same as that formed by the La + acetylene and La + 1,3-butadiene reactions (i.e. La-η^2-HCCH). The spectral and structural assignments of La-η^2-HCCH have been discussed in Chapter 6. Thus, the spectrum and structure of LaC_2H_2 will not be discussed in this chapter. MATI measurements on LaC_5H_{12} were not successful due to its low yield as shown in the mass spectrum (Figure 7.1). We tried to increase the production of LaC_5H_{12} by changing the concentration of 1-butene, and found that the LaC_5H_{12} ion intensity did not improve at different butene concentrations, but the LaC_8H_{14} ion intensity instead. Attempts to record the MATI spectrum of LaC_8H_{14} were also unsuccessful due to the slow ion signal onsets in the PIE spectrum. Therefore, the focus of this chapter is the spectroscopy and structure of LaC_4H_6.

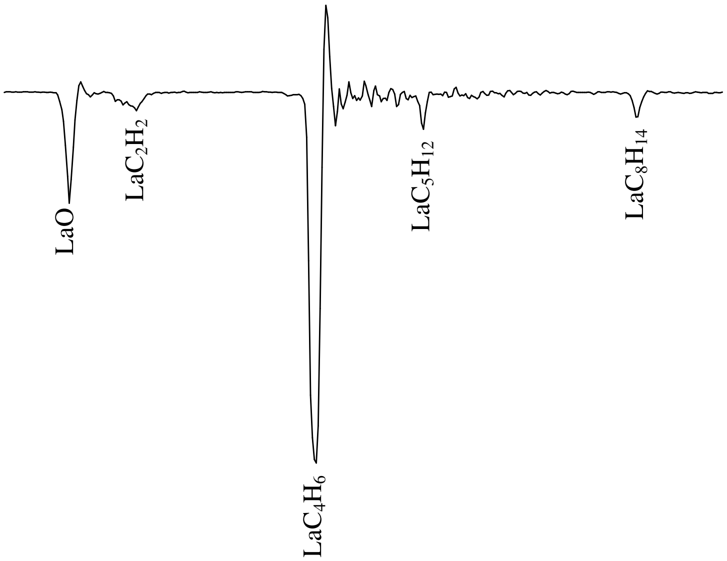

Figure 7.1 TOF-MS spectrum of the La + 1-butene reaction recorded at the laser ionization wavelength of 250 nm. The seeding concentration of 1-butene in He is 10^{-5}.

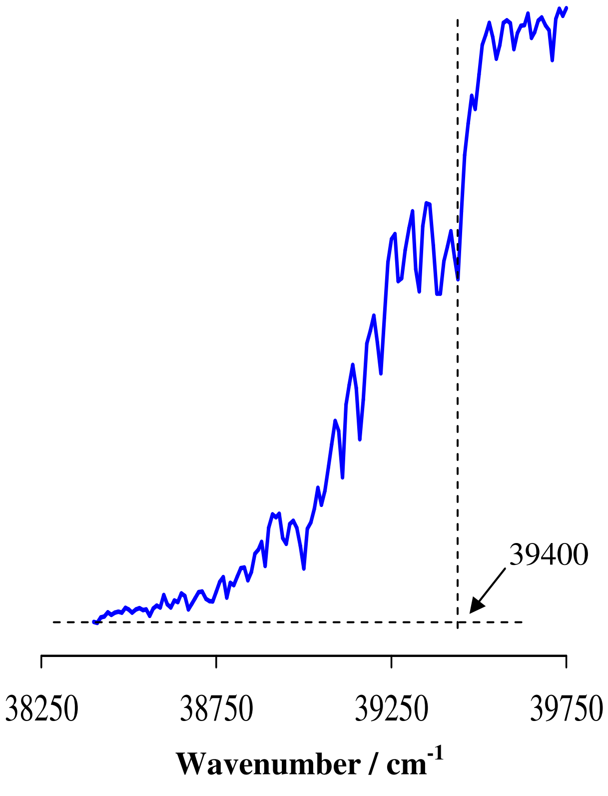

Figure 7.2 PIE spectrum of LaC_4H_6.

7.3.1 LaC_4H_6

The PIE spectrum of LaC_4H_6 shown in Figure 7.2 displays a relatively slowly rising signal onset followed by a very sharp one at 39400 (50) cm^{-1}. The slowly rising signal originates from the ionization of thermally excited vibrational levels of the neutral complex. The sharp onset corresponds to the first ionization threshold of the complex. Figure 7.3(a) presents the MATI spectrum of LaC_4H_6 seeded in a helium carrier gas. The spectrum in the region of 39000-40500 cm^{-1} exhibits the strongest band at 39420 (5) cm^{-1}, which is the origin band of an electronic transition. To the right of the origin band are a 398 cm^{-1} progression and 320 and 470 cm^{-1} intervals. To the left of the origin bands are 285 and 370 cm^{-1} intervals originating from the thermally excited neutral vibrational levels. The spectrum also shows several combination bands arising from the excitations of two or more vibrational modes. The MATI spectrum in this region is the same as those of LaC_4H_6 formed in the La + propene (Figure 5.9(a) in Chapter 5) and La + 1,3-butadiene reactions (Figure 6.8(a) in Chapter 6), and the structure of LaC_4H_6 responsible for the observed spectrum has been identified to be 1-lanthana-3-cyclopentene (i.e. isomer B labeled in Chapter 5). Besides the stronger bands in the region of 39000-40500 cm^{-1}, the spectrum displays several weaker bands in the region of 40800-42100 cm^{-1}. None of these weak bands in this region belongs to the MATI spectrum of 1-lanthana-3-cyclopentene. This part of the spectrum shows a 356 cm^{-1} interval on the right and a 346 cm^{-1} interval on the left of the band at 41260 (5) cm^{-1}. The band positions of this MATI spectrum are the same as those of lanthanum trimethylenemethane (i.e. isomer A labeled in Chapter 5) formed in the La + propene reaction, even though the signal here is much weaker. Thus, the carrier of the spectrum in the region of 39000-40500 cm^{-1} in La + 1-butene reaction can be assigned to lanthanum trimethylenemethane as well. The geometries of two isomers can be found in Table 5.3 in

Chapter 5. Figure 7.3 compares the experimental spectrum (Figure 7.3(a)) with the simulations of the $^1A' \leftarrow ^2A'$ transition of isomer B (Figure 7.3 (b), red trace) and the $^1A_1 \leftarrow ^2A_1$ transition of isomer A (Figure 7.3(b), blue trace). The major difference between the MATI spectrum of the isomer B formed in the La + 1-butene reaction (Figure 7.3) and the spectrum of the same isomer formed in the La + propene reaction (Figure 5.9) is the missing of the 26 cm^{-1} sequence bands in Figure 7.3. Since the sequence bands arise from the transition of excited vibrational levels in the neutral state, the missing of the 26 cm^{-1} bands in Figure 7.3 indicates that isomer B of LaC_4H_6 from the La + 1-butene reaction is colder than that from the La + propene reaction. This observation may not be surprising because LaC_4H_6 isomer B in two reactions are formed via different mechanisms. In the La + propene reaction, isomer B is formed in two steps: the first step is the formation of $LaCH_2$ by the cleavage of the C-C double bond of propene, and the second step is the C-C coupling between $LaCH_2$ and C_3H_6 followed by the dehydrogenation of LaC_4H_8. In the La + 1-butene reaction, on the other hand, the isomer is formed directly by the dehydrogenation of the LaC_4H_8 association complex. The reaction pathway of LaC_4H_6 formation in the La + 1-butene reaction is discussed in details in the following section. The second difference between the La + 1-butene and La + propene reaction is that the formation of isomer A is less favorable in the former than in the latter. In Chapter 5, we have discussed the reaction pathway for the formation of isomers A in the La + propene reaction in details and the detailed reaction pathway of La + 1-butene reaction will provide the reasons for the minor formation of isomer A. In the following section, I will briefly discuss about the reaction mechanisms for the formation of isomer A in the La + 1-butene reaction since the calculations on detailed reaction pathway is still in progress.

Table 7.1 summarizes the measured and calculated IEs and vibrational frequencies of two isomers. The deuterium subsituted isotopic shifts in IEs and vibrational frequencies of two isomers can be found in Table 5.4 in Chapter 5. The active vibational modes identified for isomer B are out of plane ring bending mixed with central H wagging motion, in-plane carbon skeleton bending mixed with H rocking and La-hydrocarbon stretching motion and H twisting motion. The only active vibrational mode identified for isomer A is La-hydrocarbon symmetric stretching motion mixed with H wagging motion. The band assignments of the MATI spectra of two LaC_4H_6 isomers can be found in Table 7.2.

7.3.2 Reaction Pathways for the Formation of LaC_4H_6 isomers

$La + CH_2{=}CHC_2H_5 \rightarrow LaC_4H_6 + H_2$

La assisted C-H bond activation of 1-butene produces LaC_4H_6. The detailed reaction pathway of LaC_4H_6 isomer B formation is presented in Figure 7.4 and the reaction mechanism of LaC_4H_6 isomer A formation is presented in Figure 7.5. In the formation of isomer B, the initial step is the formation of π association complex IM1 by the La atom interaction with the double bond of 1-butene. La atom then activates C_3-H bond to form IM2. In the next step La inserts in to C_3-H bond via transition state TS2 to form metal insertion product IM3. Activation of C_4-H bond and dehydrogenation occurs via TS3 and IM4 to form IM5. Finally IM5 isomerizes to isomer B via TS4. Further bond activation of isomer B of LaC_4H_6 produces LaC_2H_2 (i.e. La-η^2-HCCH) and this reaction pathway is discussed in chapter 6 since isomer B of LaC_4H_6 and La-η^2-HCCH are formed in the La + 1,3-butadiene reaction too.

In the formation of isomer A, π association complex (I) followed by the metal insertion complex (II) is formed. In the next step four member metallacycle (III) is formed. Then the inverse H migration from La to C_2 atom (IV) followed by the C_1-C_2 bond dissociation (V) occurs. Finally, the isomer A is formed after the concerted elimination of H_2 followed by the bond rearrangements (VI→VII→VIII→IX→A).

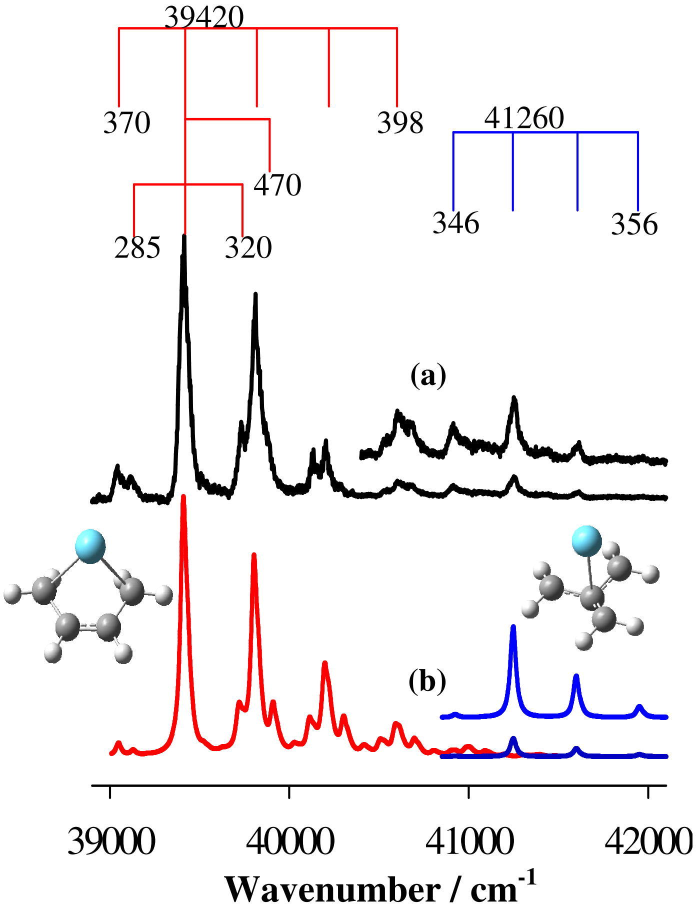

Figure 7.3 MATI spectra of LaC_4H_6 (a), and the simulated spectra of the $^1A' \leftarrow {}^2A'$ transition of isomer B (b, red trace) and the $^1A_1 \leftarrow {}^2A_1$ transition of isomer A (b, blue trace). The simulations are performed at 200 K with a FWHM of 20 cm^{-1}.

Table 7.1. Point group, adiabatic ionization energies (AIE, cm^{-1}) and vibrational frequencies (cm^{-1}) of the two isomers of LaC$_4$H$_6$ from the MATI measurements and DFT / B3LYP calculations. The associated error in experimental IEs is 5 cm^{-1}

	MATI	B3LYP
Lanthanum trimethylenemethane , C$_{3v}$		
AIE : $^1A_1 \leftarrow {}^2A_2$	41260	41806
La-hydrocarbon symmetric stretching, H wagging of neutral, υ12	327	326
La$^+$-hydrocarbonsymmetric stretching, H wagging of cation, υ12$^+$	347	351
1-lanthana-3-cyclopentene , C$_s$		
AIE : $^1A' \leftarrow {}^2A'$	39420	40178
Out of plane ring bending, central H wagging of neutral, υ13	285	280
Out of plane ring bending, central H wagging of cation, υ13$^+$	320	310
In plane C skeleton bending, H rocking, La-hydrocarbon stretching, υ12	370	360
In plane C skeleton bending, H rocking, La-hydrocarbon stretching, υ12$^+$	398	391
H twisting, υ11$^+$	470	492

Table 7.2 MATI band positions (cm^{-1}) and assignments of the two isomers of LaC_4H_6. The uncertainty associated with the band positions is 5 cm^{-1}

Lanthanum trimethylenemethane		1-lanthana-3-cyclopentene	
Position	Assignment	Position	Assignment
40914	12^0_1	39050	12^0_1
41260	0^0_0	39135	13^0_1
41616	12^1_0	39420	0^0_0
41972	12^2_0	39740	13^1_0
		39818	12^1_0
		39890	11^1_0
		40138	$12^1_0 13^1_0$
		40198	12^2_0
		40288	$11^1_0 12^1_0$

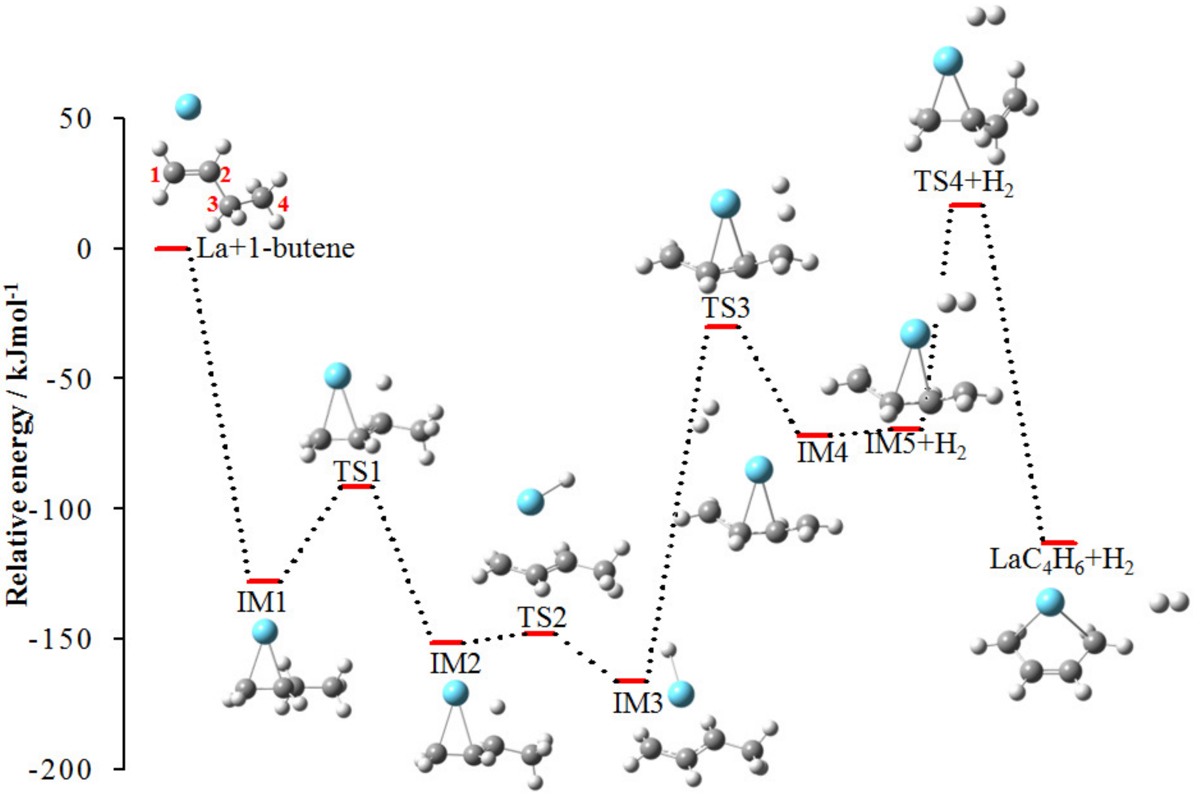

Figure 7.4 Reaction pathway for the formation of the isomer B of LaC_4H_6 from the reaction between La and 1-butene calculated at the DFT/B3LYP level. TS: Transition States, IM: Intermediates.

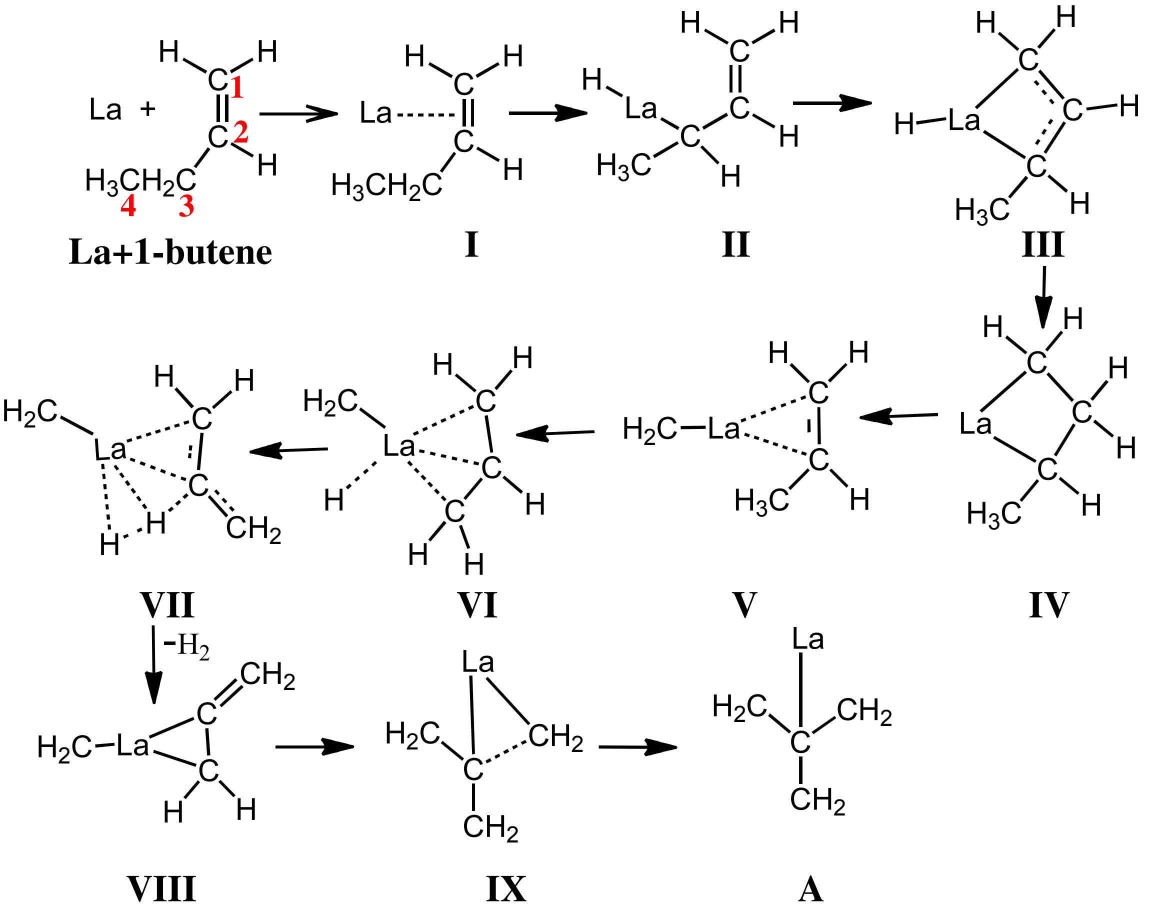

Figure 7.5 Reaction mechanism for the formation of isomer A of LaC_4H_6 from the reaction between La and 1-butene.

7.4 Conclusions

In conclusion, this study shows that the La metal-mediated C-H bond activation of 1-butene leads to the formation of lanthanum trimethylenemethane (isomer A) and 1-lanthana-3-cyclopentene (isomer B) of LaC_4H_6. These isomers are formed via the concerted elimination of the hydrogen atoms of 1-butene. Isomer A has a C_{3v} structure in the $^2A_2$ ground electronic state, whereas isomer B has a C_s structure in the $^2A'$ ground electronic state. Isomers A and B are not only observed in this reaction, but also in the La + propene reaction. On the other hand, only isomer B can be identified in the La + 1,3-butadiene reaction. In conclusion, the presence of a bond between sp^2 carbon and sp^3 carbon is essential to produce isomer A (lanthanum-trimethylenemethane). Since 1,3-butadiene doesn't have such a bond, La + 1,3-butadiene reaction generates only isomer B. To better understand the formation of LaC_4H_6 isomer A in La + 1-butene reaction, theoretical calculations of detailed reaction pathway is in progress.

REFERENCES

(1) Bergman, R. G. *Nature* **2007**, *446*, 391.
(2) Shilov, A. E.; Shul'pin, G. B. *Chem. Rev.* **1997**, *97*, 2879.
(3) Jones, W. D.; Feher, F. J. *Acc. Chem. Res.* **1989**, *22*, 91.
(4) Labinger, J. A.; Bercaw, J. E. *Nature* **2002**, *417*, 507.
(5) Hinrichs, R. Z.; Schroden, J. J.; Davis, H. F. *J. Phys. Chem. A* **2008**, *112*, 3010.
(6) Li, T. H.; Wang, C. M.; Yu, S. W.; Liu, X. Y.; Fu, H.; Xie, X. G. *J. Mol. Struct. (Theochem.)* **2009**, *907*, 119.
(7) Gibson, J. K. *J. Phys. Chem.* **1996**, *100*, 15688.
(8) Marcalo, J.; de Matos, A. P. *J. Organo. Chem.* **2002**, *647*, 216.
(9) Cloke, F. G. N. *Chem. Soc. Rev.* **1993**, *22*, 17.
(10) Cornehl, H. H.; Heinemann, C.; Schroder, D.; Schwarz, H. *Organometallics* **1995**, *14*, 992.
(11) Heinemann, C.; Schroder, D.; Schwarz, H. *Chem. Ber.* **1994**, *127*, 1807.
(12) Marcalo, J.; Santos, M.; de Matos, A. P.; Gibson, J. K.; Haire, R. G. *J. Phys. Chem. A* **2008**, *112*, 12647.
(13) Crabtree, R. H. *Chem. Rev.* **1995**, *95*, 987.
(14) Jun, C.-H. *Chem. Soc. Rev.* **2004**, *33*, 610.
(15) Yang, M.-L.; Zhu, Y.-A.; Fan, C.; Sui, Z.-J.; Chen, D.; Zhou, X.-G. *PCCP* **2011**, *13*, 3257.
(16) Hall, C.; Perutz, R. N. *Chem. Rev.* **1996**, *96*, 3125.
(17) Wencel-Delord, J.; Droge, T.; Liu, F.; Glorius, F. *Chem. Soc. Rev.* **2011**, *40*, 4740.
(18) Omae, I. *Appl. Organomet. Chem.* **2008**, *22*, 149.
(19) Abel, E. W.; Stone, F. G. A.; Wilkinson, G. *Comprehensive Organometallic Chemistry II : a review of the literature 1982-1994*; Pergamon: New York, 1995; Vol. 4.
(20) Wilkinson, G.; Stone, F. G. A.; Abel, E. W. *Comprehensive Organometallic Chemistry : the synthesis, reactions, and structures of organometallic compounds* Peramon Press: Newyork, 1982.
(21) Crabtree, R. H. *Chem. Rev.* **2010**, *110*, 575.
(22) Lee, I. M.; Gauthier, W. J.; Ball, J. M.; Iyengar, B.; Collins, S. *Organometallics* **1992**, *11*, 2115.
(23) Grubbs, R. H.; Coates, G. W. *Acc. Chem. Res.* **1996**, *29*, 85.
(24) Burger, B. J.; Thompson, M. E.; Cotter, W. D.; Bercaw, J. E. *J. Am. Chem. Soc.* **1990**, *112*, 1566.
(25) Carroll, J. J.; Haug, K. L.; Weisshaar, J. C.; Blomberg, M. R. A.; Siegbahn, P. E. M.; Svensson, M. *J. Phys. Chem.* **1995**, *99*, 13955.
(26) Holthausen, M. C.; Fiedler, A.; Schwarz, H.; Koch, W. *J. Phys. Chem.* **1996**, *100*, 6236.
(27) Schroder, D.; Schwarz, H. *Angew. Chem. Int. Ed. Engl.* **1995**, *34*, 1973.
(28) Hinrichs, R. Z.; Schroden, J. J.; Davis, H. F. *J. Phys. Chem.* **2003**, *107*, 9284.
(29) Hinrichs, R. Z.; Schroden, J. J.; Davis, H. F. *J. Am. Chem. Soc.* **2003**, *2003*, 861.
(30) Crabtree, R. H. *The Organometallic Chemistry of theTtransition Metals*; John Wiley & Sons: Newyork, 1994; Vol. 2nd ed.

(31) Gladysz, J. A. *Chem. Rev. (special issue)* **2011**, *111(3)*, 1167.

(32) Marder, T. B.; Dyer, P. W.; Fairlamb, I. J. S.; Gibson, S.; Scott, P. *Dalton Trans. (themed issue)* **2010**, *39*, 10321.

(33) Eller, K.; Schwarz, H. *Chem. Rev.* **1991**, *91*, 1121.

(34) Bohme, D. K.; Schwarz, H. *Angew. Chem. Int. Ed.* **2005**, *44*, 2336.

(35) Armentrout, P. B. *Int. J. Mass spectrom.* **2003**, *227*, 289.

(36) Freiser, B. S. *Acc. Chem. Res.* **1994**, *27*, 353.

(37) Simoes, J. A. M.; Beauchamp, J. L. *Chem. Rev.* **1990**, *90*, 629.

(38) Metz, R. B. *Int. Rev. Phys. Chem.* **2004**, *23*, 79.

(39) Schroden, J. J.; Davis, H. F. In *Modern Trend in Chemical Dynamics Part II: Experiment and Theory (Advanced Series in Physical Chemistry: Vol 14)*; Yang, X., Lium, K., Eds.; World Scientific: Singapore, 2004.

(40) Mitchell, S. A. In *Gas Phase Metal Reactions, ACS Symposium Series*; Fontijn, A., Ed.; Elsevier: Amsterdam, 1992.

(41) Carroll, J. J.; Haug, K. L.; Weisshaar, J. C. *J. Am. Chem. Soc.* **1993**, *115*, 6962.

(42) Stauffer, H. U.; Hinrichs, R. Z.; Willis, P. A.; Davis, H. F. *J. Chem. Phys.* **1999**, *111*, 4101.

(43) H.U.Stauffer; R.Z.Hinrichs; J.J.Stauffer; J.J.Schroden; H.F.Davis *J. Phys. Chem. A* **2000**, *104*, 1107

(44) Wen, Y.; Porembski, M.; Ferrett, T. A.; Weisshaar, J. C. *J. Phys. Chem. A* **1998**, *102*, 8362.

(45) Ritter, D.; Carroll, J. J.; Weisshaar, J. C. *J. Phys. Chem.* **1992**, *96*, 10636.

(46) Porembski, M.; Weisshaar, J. C. *J. Phys. Chem. A* **2001**, *105*, 6655.

(47) Lech, L. M.; Freiser, B. S. *Organometallics* **1988**, *7*, 1948.

(48) Sunderlin, L. S.; Armentrout, P. B. *J. Am. Chem. Soc.* **1989**, *111*, 3845.

(49) Flory, M. A.; Apponi, A. J.; Zack, L. N.; Ziurys, L. M. *J. Am. Chem. Soc.* **2010**, *132*, 17186.

(50) Proctor, D. L.; Davis, H. F. *Proc. Natl. Acad. Sci. USA* **2008**, *105*, 12673.

(51) Cho, H.-G.; Andrews, L. *J. Phys. Chem. A* **2007**, *111*, 5201.

(52) Andrews, L.; Cho, H.-G. *Organometallics* **2006**, *25*, 4040.

(53) Ball, D. W.; Pong, R. G. S.; Kafafi, Z. H. *J. Phys. Chem.* **1994**, *98*, 10720.

(54) Wiest, O.; Wu, Y. *Computational Organometallic Chemistry*; Springer: New York, 2012.

(55) Cundari, T. R. *Computational Organometallic Chemistry*; Marcel Dekker: New York, 2001.

(56) Wittborn, A. M. C.; Costas, M.; Blomberg, M. R. A.; Siegbahn, P. E. M. *J. Chem. Phys.* **1997**, *107*, 4318.

(57) Hu, X.; Li, H.; Wu, T. *J. Phys. Chem. A* **2011**, *115*, 904.

(58) Siegbahn, P. E. M.; Blomberg, M. R. A. *J. Am. Chem. Soc.* **1992**, *114*, 10548.

(59) Kagan, H. B. *Chem. Rev.* **2002**, *102*, 1805.

(60) Einstein, A. *Ann. Phys.* **1905**, *17*, 549.

(61) Koopmans, T. *Physica* **1933**, *1*, 104.

(62) Yang, D. S. *Coord. Chem. Rev.* **2001**, *214*, 187.

(63) Turner, D. W. *Phil. Trans. Roy. Soc. Lond.* **1970**, *268*, 7.

(64) Dethlefs, K. M.; Schag, E. W. *Angew Chem. Int.* **1998**, *37*, 1346.

(65) Rothschopf, G. K.; Perkins, J. S.; Li, S.; Yang, D. S. **2000**, *104*, 8178.

(66) Merkt, F.; Schmutz, H. *J. Chem. Phys.* **1998**, *108*, 10033.

(67) Taylor, D. P.; Goode, J. G.; Leclaire, J. E.; Johnson, P. M. *J. Chem. Phys.* **1995**, *103*, 6293.

(68) Held, A.; Schlag, E. W. *Acc. Chem. Res.* **1998**, *31*, 467.

(69) Merkt, F. *Annu. Rev. Phys. Chem.* **1997**, *48*, 675.

(70) Cockett, M. C. R. *Chem. Soc. Rev.* **2005**, *34*, 935.

(71) Hepburn, J. W. *Chem. Soc. Rev.* **1996**, *25*, 281.

(72) Sohnlein, B. R.; Yang, D.-S. *J. Chem. Phys.* **2006**, *124*, 134305/1.

(73) Marks, T. J. *Bonding energetics in organometallic compounds* American Chemical Society: Washington, 1990.

(74) Zhu, L.; Jpgnson, P. *J. Chem. Phys.* **1991**, *94*, 5769.

(75) Ford, M. S.; Mackenzie, S. R. *J. Chem. Phys.* **2005**, *123*, 084308.

(76) Jouvet, C.; Lardeux, C. D.; Barra, S. M.; Solgadi, D. *Chem. Phys. Lett.* **1992**, *198*, 419.

(77) Kostko, O.; Kim, S. K.; Leone, S. R.; Ahmed, M. **2009**, *113*, 14206.

(78) Kostko, O.; Kim, S. K.; Leone, S. R.; Ahmed, M. *J. Phys. Chem. A* **2009**, *113*, 14206.

(79) McQuarrie, D. A. *Quantum Chemistry*; University Science Books: Sausalito, 1983.

(80) Born, M.; Oppenheimer, J. R. *Ann. Phys.* **1927**, *79*, 361.

(81) Christopher, J. C. *Essentials of Computational Chemistry*; 2nd Edition ed.; John Wiley & Sons Ltd: England, 2004.

(82) Lee, C. T.; Yang, W. T.; Parr, R. G. *Phys. Rev. B* **1988**, *37*, 785.

(83) Miehlich, B.; Savin, A.; Stoll, H.; Preuss, H. *Chem. Phys. Lett.* **1989**, *157*, 200.

(84) Becke, A. D. *J. Chem. Phys.* **1993**, *98*, 5648.

(85) Shenggang, L. PhD Dissertation, University of Kentucky, 2004.

(86) Franck, J. *Trans. Faraday Soc.* **1925**, *21*, 536.

(87) Condon, E. *Phys. Rev.* **1926**, *28*, 1182.

(88) Condon, E. *Phys. Rev.* **1928**, *32*, 858.

(89) Shenggang, L.; Clouthier, D. **Unpublished results, 2006**.

(90) Doktorov, E. V.; Malkin, I. A.; Man'ko, V. I. *J. Mol. Spectrosc.* **1977**, *64*, 302.

(91) Wiley, W. C.; McLaren, I. H. *Rev. Sci. Instrum.* **1955**, *26*, 1150.

(92) Frish, M. J.; Trucks, G. W.; Schlegel, H. B.; GAUSSIAN 03,Revision C.02 ed.; Gaussian, Inc.: Wallingford, CT, 2004.

(93) Krishnan, R.; Binkley, J. S.; Seeger, R.; Pople, J. A. *J. Chem. Phys.* **1980**, *72*, 650.

(94) McLean, A. D.; Chandler, G. S. *J. Chem. Phys.* **1980**, *72*, 5639.

(95) Dolg, M.; Stoll, H.; Savin, A.; Preuss, H. *Theoretica Chimica Acta* **1989**, *75*, 173.

(96) Pople, J. A.; Headgordon, M.; Raghavachari, K. *J. Chem. Phys.* **1987**, *87*, 5968.

(97) Dunning, T. H. *J. Chem. Phys.* **1989**, *90*, 1007.

(98) Woon, D. E.; Dunning, T. H. *J. Chem. Phys.* **1994**, *100*, 2975.

(99) Duschinsky, F. *Acta physicochimica U.R.S.S* **1937**, *7*, 551.

(100) Tysoe, W. T.; Nyberg, G. L.; Lambert, R. M. *J. Chem. Soc., Chem. Commun.* **1983**, 623.

(101) Kesmodel, L. L.; Waddill, G. D.; Gates, J. A. *Surf. Sci.* **1984**, *138*, 464.

(102) Abdelrehim, I. M.; Pelhos, K.; Madey, T. E.; Eng, J.; Chen, J. G. G. *J. Phys. Chem. B* **1998**, *102*, 9697.
(103) Logan, M. A.; Rucker, T. G.; Gentle, T. M.; Muetterties, E. L.; Somorjai, G. A. *J. Phys. Chem.* **1986**, *90*, 2709.
(104) Judai, K.; Abbet, S.; Worz, A. S.; Ferrari, A. M.; Giordano, L.; Pacchioni, G.; Heiz, U. *J. Mol. Catal. A-Chemical* **2003**, *199*, 103.
(105) Stacchiola, D.; Molero, H.; Tysoe, W. T. *Catal. Today* **2001**, *65*, 3.
(106) Caldwell, T. E.; Abdelrehim, I. M.; Land, D. P. *Langmuir* **1998**, *14*, 1407.
(107) Abdelrehim, I. M.; Caldwell, T. E.; Land, D. P. *J. Phys. Chem.* **1996**, *100*, 10265.
(108) Ramirezcuesta, A.; Zgrablich, G.; Tysoe, W. T. *Surf. Sci.* **1995**, *340*, 109.
(109) Pacchioni, G.; Lambert, R. M. *Surf. Sci.* **1994**, *304*, 208.
(110) Sesselmann, W.; Woratschek, B.; Ertl, G.; Kuppers, J.; Haberland, H. *Surf. Sci.* **1983**, *130*, 245.
(111) Patterson, C. H.; Mundenar, J. M.; Timbrell, P. Y.; Gellman, A. J.; Lambert, R. M. *Surf. Sci.* **1989**, *208*, 93.
(112) Hoffmann, H.; Zaera, F.; Ormerod, R. M.; Lambert, R. M.; Wang, L. P.; Tysoe, W. T. *Surf. Sci.* **1990**, *232*, 259.
(113) Sharma, P.; Attah, I.; Momoh, P.; El-Shall, M. S. *Int. J. Mass spectrom.* **2011**, *300*, 81.
(114) Martinez, M.; Michelin, M. D.; Rivalta, I.; Russo, N.; Sicilia, E. *Inorg. Chem.* **2005**, *44*, 9807.
(115) Wesendrup, R.; Schwarz, H. *Organometallics* **1997**, *16*, 461.
(116) Chretien, S.; Salahub, D. R. *J. Chem. Phys.* **2003**, *119*, 12279.
(117) Chretien, S.; Salahub, D. R. *J. Chem. Phys.* **2003**, *119*, 12291.
(118) Marchon, B. *Surf. Sci.* **1985**, *162*, 382.
(119) Ma, Y.-P.; Xue, W.; Wang, Z.-C.; Ge, M.-F.; He, S.-G. *J. Phys. Chem. A* **2008**, *112*, 3731.
(120) Ormerod, R. M.; Lambert, R. M. *Catal. Lett.* **1990**, *6*, 121.
(121) Stang, P. J.; Diederich, F. *Modern Acetylene Chemistry*; VCH: New York, 1995.
(122) Ormerod, R. M.; Lambert, R. M.; Hoffmann, H.; Zaera, F.; Yao, J. M.; Saldin, D. K.; Wang, L. P.; Bennett, D. W.; Tysoe, W. T. *Surf. Sci.* **1993**, *295*, 277.
(123) Abdelrehim, I. M.; Thornburg, N. A.; Sloan, J. T.; Caldwell, T. E.; Land, D. P. *J. Am. Chem. Soc.* **1995**, *117*, 9509.
(124) Tysoe, W. T.; Nyberg, G. L.; Lambert, R. M. *Surf. Sci.* **1983**, *135*, 128.
(125) Teng, Y.-L.; Xu, Q. *J. Phys. Chem. A* **2010**, *114*, 9069.
(126) Cho, H.-G.; Andrews, L. *J. Phys. Chem. A* **2010**, *114*, 10028.
(127) Cho, H.-G.; Andrews, L. *J. Phys. Chem. A* **2012**, *116*, 10917.
(128) Glendening, E. D. *J. Phys. Chem. A* **2004**, *108*, 10165.
(129) Moore, C. E. *Atomic Energy Levels*; National Bureau of Standards: Washington, DC, 1971.
(130) Duncan, M. A.; Dietz, T. G.; Smalley, R. E. *J. Chem. Phys.* **1981**, *75*, 2118.
(131) Yang, D. S. *J. Phys. Chem. Lett.* **2011**, *2*, 25.
(132) Li, S. Ph.D. Thesis, University of Kentucky, 2004.
(133) Doktorov, E. V.; Malkin, I. A.; Man'ko, V. I. *J. Mol. Spectrosc.* **1977**, *64*, 302.
(134) Kumari, S. Dissertation, University of Kentucky, 2014.

(135) Huang, Y. Q.; Hill, Y. D.; Sodupe, M.; Bauschlicher, C. W.; Freiser, B. S. *Inorg. Chem.* **1991**, *30*, 3822.
(136) Liu, Y.; Kumari, S.; Roudjane, M.; Li, S.; Yang, D.-S. *J. Chem. Phys.* **2012**, *136*.
(137) Radhakrishnan, K. V.; Yoshikawa, E.; Yamamoto, Y. *Tetrahedron Lett.* **1999**, *40*, 7533.
(138) Kan, S. Z.; Xu, Y. C.; Chen, Q.; Freiser, B. S. *J. Mass Spectrom.* **1997**, *32*, 1310.
(139) Wittneben, D.; Grutzmacher, H. F.; Butenschon, H.; Wey, H. G. *Organometallics* **1992**, *11*, 3111.
(140) Huang, Y. Q.; Freiser, B. S. *J. Am. Chem. Soc.* **1989**, *111*, 2387.
(141) Huang, Y. Q.; Freiser, B. S. *J. Am. Chem. Soc.* **1990**, *112*, 1682.
(142) Bennett, M. A.; Wenger, E. *Organometallics* **1995**, *14*, 1267.
(143) Bennett, M. A.; Wenger, E. *Organometallics* **1996**, *15*, 5536.
(144) Willis, P. A.; Stauffer, H. U.; Hinrichs, R. Z.; Davis, H. F. *J. Phys. Chem. A* **1999**, *103*, 3706.
(145) Weisshaar, J. C. *Acc. Chem. Res.* **1993**, *26*, 213.
(146) Greaves, S. J.; Rose, R. A.; Oliver, T. A. A.; Glowacki, D. R.; Ashfold, M. N. R.; Harvey, J. N.; Clark, I. P.; Greetham, G. M.; Parker, A. W.; Towrie, M.; Orr-Ewing, A. J. *Science* **2011**, *331*, 1423.
(147) Crim, F. F. *Faraday Discuss.* **2012**, *157*, 9.
(148) Elles, C. G.; Crim, F. F. *Annu. Rev. Phys. Chem.* **2006**, *57*, 273.
(149) Ferhati, A.; Sozzi, G.; Ohanessian, G. *Org. Mass Spectrom.* **1993**, *28*, 1453.
(150) Baranov, V.; Becker, H.; Bohme, D. K. *J. Phys. Chem. A* **1997**, *101*, 5137.
(151) Lide, D. R. *CRC Handbook of Chemistry and Physics*; 88ed. ed.; CRC: Boca Raton, FL, 2008.
(152) McCullough, L. G.; Schrock, R. R.; Dewan, J. C.; Murdzek, J. C. *J. Am. Chem. Soc.* **1985**, *107*, 5987.
(153) Gong, D.; Wang, B.; Bai, C.; Bi, J.; Wang, F.; Dong, W.; Zhang, X.; Jiang, L. *Polymer* **2009**, *50*, 6259.
(154) Porembski, M.; Weisshaar, J. C. *J. Phys. Chem. A* **2001**, *105*, 6655.
(155) Porembski, M.; Weisshaar, J. C. *J. Phys. Chem. A* **2001**, *105*, 4851.
(156) Parnis, J. M.; Lafleur, R. D.; Rayner, D. M. *J. Phys. Chem.* **1995**, *99*, 673.
(157) Porembski, M.; Weisshaar, J. C. *J. Phys. Chem. A* **2000**, *104*, 1524.
(158) Blomberg, M. R. A.; Siegbahn, P. E. M.; Svensson, M. *J. Phys. Chem.* **1992**, *96*, 9794.
(159) Castillo, S.; Poulain, E.; Novaro, O. *Int. J. Quantum Chem* **1989**, 509.
(160) Siegbahn, P. E. M. *J. Am. Chem. Soc.* **1993**, *115*, 5803.
(161) Siegbahn, P. E. M. *Theoretica Chimica Acta* **1994**, *87*, 277.
(162) Gleiter, R.; Hylakryspin, I.; Niu, S. Q.; Erker, G. *Organometallics* **1993**, *12*, 3828.
(163) Senba, K.; Matsui, R.; Honma, K. *J. Phys. Chem.* **1995**, *99*, 13992.
(164) Thompson, M. G. K.; Walker, S. W. C.; Parnis, J. M. *Inorg. Chem.* **2011**, *50*, 7317.
(165) Andrews, L.; Cho, H. G.; Wang, X. F. *Angew. Chem. Int. Ed.* **2005**, *44*, 113.
(166) Cho, H. G.; Wang, X. F.; Andrews, L. *J. Am. Chem. Soc.* **2005**, *127*, 465.
(167) Dahlmann, M.; Erker, G.; Bergander, K. *J. Am. Chem. Soc.* **2000**, *122*, 7986.
(168) Karl, J.; Dahlmann, M.; Erker, G.; Bergander, K. *J. Am. Chem. Soc.* **1998**, *120*, 5643.

(169) Hettich, R. L.; Freiser, B. S. *J. Am. Chem. Soc.* **1987**, *109*, 3543.
(170) Irikura, K. K.; Goddard, W. A. *J. Am. Chem. Soc.* **1994**, *116*, 8733.
(171) Brookhart, M.; Green, M. L. H. *J. Organomet. Chem.* **1983**, *250*, 395.
(172) Brookhart, M.; Green, M. L. H.; Parkin, G. *Proc. Natl. Acad. Sci. USA* **2007**, *104*, 6908.
(173) Crabtree, R. H. *Chem. Rev.* **1985**, *85*, 245.
(174) Wada, K.; Pamplin, C. B.; Legzdins, P.; Patrick, B. O.; Tsyba, I.; Bau, R. *J. Am. Chem. Soc.* **2003**, *125*, 7035.
(175) Janiak, C. *J. Organomet. Chem.* **1993**, *452*, 63.
(176) Prosenc, M. H.; Janiak, C.; Brintzinger, H. H. *Organometallics* **1992**, *11*, 4036.
(177) Omae, I. *J. Organomet. Chem.* **2011**, *696*, 1128.
(178) Roos, B. O.; Lindh, R.; Cho, H.-G.; Andrews, L. *J. Phys. Chem. A* **2007**, *111*, 6420.
(179) de Macedo, L. G. M.; Pyykko, P. *Chem. Phys. Lett.* **2008**, *462*, 138.
(180) Lein, M. *Coord. Chem. Rev.* **2009**, *253*, 625.
(181) Berkaine, N.; Reinhardt, P.; Alikhani, M. E. *Chem. Phys.* **2008**, *343*, 241.
(182) Thakur, T. S.; Desiraju, G. R. *Comp. Theor. Chem.* **2007**, *810*, 143.
(183) Xu, B.; Wang, Q.; Wang, X. *Comp. Theor. Chem.* **2011**, *976*, 36.
(184) Popelier, P. L. A.; Logothetis, G. *J. Organomet. Chem.* **1998**, *555*, 101.
(185) Roos, B. O.; Pyykko, P. *Chem. Eur. J.* **2010**, *16*, 270.
(186) Zhang, X.; Schwarz, H. *Chem. Eur. J.* **2010**, *16*, 5882.
(187) Goddard, R. J.; Hoffmann, R.; Jemmis, E. D. *J. Am. Chem. Soc.* **1980**, *102*, 7667.
(188) Makshina, E. V.; Janssens, W.; Sels, B. F.; Jacobs, P. A. *Catal. Today* **2012**, *198*, 338.
(189) Zemski, K. A.; Bell, R. C.; Castleman, A. W. *J. Phys. Chem. A* **2000**, *104*, 5732.
(190) Zemski, K. A.; Bell, R. C.; Castleman, A. W. *Int. J. Mass spectrom.* **1999**, *184*, 119.
(191) Bell, R. C.; Zemski, K. A.; Kerns, K. P.; Deng, H. T.; Castleman, A. W. *J. Phys. Chem. A* **1998**, *102*, 1733.
(192) Schroeter, K.; Schalley, C. A.; Wesendrup, R.; Schroder, D.; Schwarz, H. *Organometallics* **1997**, *16*, 986.
(193) Bakhtiar, R.; Drader, J. J.; Jacobson, D. B. *J. Am. Chem. Soc.* **1992**, *114*, 8304.
(194) Bakhtiar, R.; Drader, J. J.; Arneson, R. K.; Jacobson, D. B. *Rapid Commun. Mass Spectrom.* **1996**, *10*, 1405.
(195) Liu, H.; Jia, X.; Wang, F.; Dai, Q.; Wang, B.; Bi, J.; Zhang, C.; Zhao, L.; Bai, C.; Hu, Y.; Zhang, X. *Dalton Trans.* **2013**, *42*, 13723.
(196) Wang, B.; Gong, D.; Bi, J.; Dai, Q.; Zhang, C.; Hu, Y.; Zhang, X.; Jiang, L. *Appl. Organomet. Chem.* **2013**, *27*, 245.
(197) Liu, L.; Zhang, X.; Liu, H.; Zhang, X.; Sun, G.; Zhang, H. *Inorg. Chim. Acta* **2014**, *414*, 8.
(198) Chen, L.; Ai, P.; Gu, J.; Jie, S.; Li, B.-G. *J. Organomet. Chem.* **2012**, *716*, 55.
(199) Ai, P.; Chen, L.; Guo, Y.; Jie, S.; Li, B.-G. *J. Organomet. Chem.* **2012**, *705*, 51.
(200) Gong, D.; Wang, B.; Cai, H.; Zhang, X.; Jiang, L. *J. Organomet. Chem.* **2011**, *696*, 1584.
(201) Gong, D.; Jia, X.; Wang, B.; Wang, F.; Zhang, C.; Zhang, X.; Jiang, L.; Dong, W. *Inorg. Chim. Acta* **2011**, *373*, 47.

(202) Annunziata, L.; Pragliola, S.; Pappalardo, D.; Tedesco, C.; Pellecchia, C. *Macromolecules* **2011**, *44*, 1934.
(203) El Kolli, N.; Delannoy, L.; Louis, C. *J. Catal.* **2013**, *297*, 79.
(204) Yardimci, D.; Serna, P.; Gates, B. C. *Acs Catalysis* **2012**, *2*, 2100.
(205) Hughes, R. P.; Rose, P. R.; Rheingold, A. L. *Organometallics* **1993**, *12*, 3109.
(206) Diamond, G. M.; Green, M. L. H.; Walker, N. M.; Howard, J. A. K.; Mason, S. A. *Journal of the Chemical Society-Dalton Transactions* **1992**, 2641.
(207) Evans, W. J.; Engerer, S. C.; Neville, A. C. *J. Am. Chem. Soc.* **1978**, *100*, 331.
(208) Eng, J.; Fruhberger, B.; Chen, J. G.; Bent, B. E. *Catal. Lett.* **1998**, *54*, 133.
(209) Small, B. L.; Schmidt, R. *Chem. Eur. J.* **2004**, *10*, 1014.
(210) Hinrichs, R. Z.; Schroden, J. J.; Davis, H. F. *J. Phys. Chem. A* **2003**, *107*, 9284.
(211) Toledo, J. A.; Bosch, P.; Valenzuela, M. A.; Montoya, A.; Nava, N. *J. Mol. Catal. A-Chemical* **1997**, *125*, 53.
(212) Ranatunga, D. F. A.; Hill, Y. D.; Freiser, B. S. *Organometallics* **1996**, *15*, 1242.
(213) Kukulska-Zajac, E.; Kumar, N.; Salmi, T.; Murzin, D. Y.; Datka, J. *Catal. Today* **2005**, *100*, 407.
(214) Li, H. Y.; Pu, M.; Liu, K. H.; Zhang, B. F.; Chen, B. H. *Chem. Phys. Lett.* **2005**, *404*, 384.
(215) Huang, Y. Q.; Hill, Y. D.; Sodupe, M.; Bauschlicher, C. W.; Freiser, B. S. *J. Am. Chem. Soc.* **1992**, *114*, 9106.

VITAE

B. Sc., Statistics, University of Colombo, Sri Lanka 2006

Publications:

- **Hewage, D**; Roudjane, M; Silva, W. R; Kumari, S; Yang, D.-S. "*Lanthanum-mediated C-H bond activation of propyne and identification of La(C_3H_2) isomers*" *J. Phys. Chem.* **2014,** 119, 2857.
- Kumari , S; Sohnlein, B. R; **Hewage, D**; Roudjane, M; Sup Lee, J; Yang, D.S. *"Binding sites and electronic states of group 3 metal-aniline complexes probed by high resolution electron spectroscopy" J. Chem. Phys.* **2013,** 138, 224304.
- Kumari , S; Roudjane, M; **Hewage, D**; Liu, Y; Yang, D.S. "*High-resolution electron spectroscopy of lanthanide (Ce, Pr and Nd) complexes of cyclooctatetraene: the role of 4f electron" J. Chem. Phys.* **2013,** 138, 164307.
- **Hewage, D**; Silva, W. R; Kumari, S; Tao, H; Yang, D.-S. *"C-C Bond Activation and Coupling of propene induced by lanthanum atom*" In preparation.
- **Hewage, D**; Silva, R; Yang, D.-S. "*Lanthanum-mediated Cyclo-oligomerization of acetylene to benzyne and naphthalene*" In preparation.
- **Hewage, D**; Yang, D.-S. "*C-C and C-H bond activation, and coupling of 1,3-butadiene induced by Lanthanum atom*" In preparation.
- Silva, R; **Hewage. D**; Yang, D.-S. "*C-O and O-H bond activation of methanol by lanthanum atom*" In preparation.

Conference Presentations

- **Hewage, D**; Yang, D.-S. "C-C bond activation, coupling and cyclomerization of 1,3-butadiened by La metal" Multimedia presentation at 69th International Symposium on Molecular Spectroscopy in Urbana-Champaign, Illinois, 2014.
- **Hewage, D**; Silva, R; Kumari, S; Tao, H; Yang, D.-S. "C-C bond activation and coupling of propene induced by La metal" Multimedia presentation at 68th International Symposium on Molecular Spectroscopy in Columbus, Ohio, 2013.

- **Hewage, D**; Silva, R; Yang, D.-S. “Cyclopolymerization of acetylene to benzyne and naphthalene” Multimedia presentation at 67th International Symposium on Molecular Spectroscopy in Columbus, Ohio, 2012.
- **Silva, R**; Hewage. D; Yang, D.-S. "C-O and O-H bond activation by lanthanum atom" Multimedia presentation at 67th International Symposium on Molecular Spectroscopy in Columbus, Ohio, 2012.
- **Hewage, D**; Roudjane, M; Yang, D.-S. “Two La(C_3H_2) isomers formed by dehydrogenation of propyne” Multimedia presentation at 66th International Symposium on Molecular Spectroscopy in Columbus, Ohio, 2011.
- S. Kumari, R. Silva, **D. Hewage**, T. H. Li, and D. S. Yang, “Metal mediated C-H and C-C bond activation of propene” Multimedia presentation at 66th International Symposium on Molecular Spectroscopy in Columbus, Ohio, 2011.
- S. Kumari, M. Roudjane, R. Silva, **D. Hewage**, and D. S. Yang, “Metal (La and Ce) assisted bond activation of ethylene” Multimedia presentation at 66th International Symposium on Molecular Spectroscopy in Columbus, Ohio, 2011.